This is to certify that the

dissertation entitled

NMR Studies of Dopants in Fluorapatite

presented by

Liam B. Moran

has been accepted towards fulfillment
of the requirements for

_Ph.D._ degree in _Chemistry_

James L. Dye
Major professor

Date _May 17, 1996_

PLACE IN RETURN BOX to remove this checkout from your record.
TO AVOID FINES return on or before date due.

DATE DUE	DATE DUE	DATE DUE
_____	_____	_____
_____	_____	_____
_____	_____	_____
_____	_____	_____
_____	_____	_____
_____	_____	_____
_____	_____	_____

NMR STUDIES OF DOPANTS IN FLUORAPATITE

by

Liam B. Moran

A DISSERTATION

Submitted to Michigan State University in partial fulfillment of the
requirements for the degree of

DOCTOR OF PHILOSOPHY

Department of Chemistry

1996

ABSTRACT

NMR STUDIES OF DOPANTS IN FLUORAPATITE

By

Liam B. Moran.

Phosphors based on calcium fluorapatite $[(Ca_5F(PO_4)_3]$ doped with small amounts of Sb^{3+} as an activator are used in most fluorescent lamps. We have used quantitative ^{19}F and ^{31}P MAS-NMR to study a series of samples of calcium fluorapatite containing 0.0 to 3.0 wt. % Sb^{3+} in order to determine the site of antimony substitution. There were no peaks in ^{31}P MAS-NMR spectra of fluorapatite related to antimony. The ^{31}P MAS-NMR spectra of the model compounds $SbPO_4$, $Sr_{1.03}Ca_{8.97}F_2(PO_4)_6$, $Sr_5F(PO_4)_3$ and $Ba_5F(PO_4)_3$ were also obtained. The ^{19}F MAS-NMR spectra of the antimony doped samples exhibit two peaks associated with antimony at 65.6 and 68.6 ppm. The SPARTAN and SINK pulse sequences were used to measure spin diffusion between the antimony related fluorine spins and those of unperturbed apatitic fluorine nuclei. These results demonstrate that each Sb^{3+} ion is perturbing fluoride ions in at least two different chains. An additional peak at 73.1 ppm observed in some samples is assigned to a second type of antimony(III) substitution, with a single fluoride ion perturbed by each antimony ion. The results in total provide detailed support for a substitution model in which antimony(III) occupies a phosphate site in the apatite lattice, with an SbO_3^{3-} group replacing a PO_4^{3-} group. Two types of substitution at this site appear to occur, depending upon which oxygen atom is replaced by the antimony lone electron pair.

A method for obtaining multiple-quantum NMR spectra of a selected homogeneously broadened portion of an inhomogeneously broadened powder

pattern is demonstrated with ^{19}F results for polycrystalline calcium fluorapatite, $Ca_5F(PO_4)_3$, and doped fluoraptite systems. In addition to providing a means for studying the anisotropic growth of multiple-quantum coherences, chemical shift selective MQ NMR provides information about the correlation length of chemical shielding tensors (i.e. the distance over which the shielding tensors of given species maintain identical principal values and orientations). The growth of ^{19}F multiple quantum coherences in fluorapatite solid solution with 10% of the calcium ions replaced with strontium ions is significantly slower compared to that of the calcium fluorapatite at the same selected chemical shift. The slower growth rate is interpreted in terms of a decrease in the average correlation length of the shielding tensor in a one dimensional chain of fluoride ions in the solid solution, due to the ^{19}F chemical-shift perturbations caused by strontium ion substitutions. The growth of ^{19}F multiple-quantum coherences in fluorapatite doped with 2.1 wt. % antimony was the same as in stoichiometric fluorapatite. This result was used to rule out the possibility that antimony substitution in fluorapatite is accompanied by the removal of neighboring fluoride ions. The chemical shift selective MQ-NMR technique was also used to study multiple-quantum growth dynamics as a function of dipolar coupling strength in polycrystalline fluorapatite by recording the MQ -NMR spectra of different classes of crystal orientations.

To my parents

Acknowledgments

TABLE OF CONTENTS

IV. Chemical-Shift-Selective multiple Quantum NMR as a Probe of the

Correlation Length of Chemical Shielding Tensors

V. Chemical-Shift-selective Multiple Quantum NMR Applied to the Study of the

Effect of Dimensionality on Growth Dynamics

List Of Tables

List of Figures

I. INTRODUCTION

I-1. Overview

The research presented in this thesis features the application of both established and newly developed solid-state NMR techniques to some systems based on calcium fluorapatite, including a phosphor used in the commercial lighting industry. In this overview section (I-1) the different projects will be briefly described. Then the chemistry and structure of the apatite system, $M_5X(YO_4)_3$, will be discussed in section I-2; in this work, $M = Ca^{++}$, Sr^{++}, Ba^{++}, $X = F^-$, Cl^-, OH^- and $Y = P$, (Si, S)[1], As. Next, the portions of the nuclear spin Hamiltonian relevant to solid state NMR will be described (section (I-3.1)). The principal tool for computing the time evolution of a system of spins (hereinafter referred to as a "spin system") under the influence of a particular spin Hamiltonian, the density matrix, will be discussed in section I-3.2. Section I-3.3 will explain the concepts and experimental techniques of multiple-quantum NMR that are used in Sections IV and V. In section I-3.4 the experimental technique of Magic Angle Spinning (MAS) NMR will be reviewed, and details of the dynamics of spins under MAS conditions required to understand the newly developed MAS-based experiments in sections II and III will be discussed. Finally, the concepts, experimental techniques, and uses of spin diffusion experiments will be discussed in section I-3.5.

The common theme of the work in subsequent sections (II-V) is the study of dopants in calcium fluorapatite [$Ca_5F(PO_4)_3$]. In section II a halophosphate phosphor, antimony-doped fluorapatite, is examined using ^{31}P and ^{19}F MAS-NMR and spin diffusion techniques as an indirect probe of the antimony ion in the lattice. Apatite based phosphors are of great commercial importance and are produced on a kiloton per year scale for use in fluorescent lamps. In order to understand the processes by which these apatite phosphors absorb and emit light, and how their performance degrades over time, it is important to know the location of the activator

ion (antimony) in the apatite lattice. Based on the presence of several antimony-associated peaks in the ^{19}F MAS-NMR spectra and the lack of any such peaks in the ^{31}P MAS-NMR spectra , we concluded that the antimony resides in a phosphate site in the lattice. This conclusion is strengthened by the results of spin diffusion measurements made between the antimony-associated peaks in the ^{19}F NMR spectra using the SPARTAN technique. In section III the spin diffusion measurements between the antimony-related peaks in the ^{19}F MAS-NMR spectrum are extended with a technique called SINK that is especially well-adapted to observing spin diffusion from minor to major peaks in a spectrum. This new method, SINK, helps clarify some experimental observations of Section II and strengthen some of the conclusions drawn there.

Sections IV and V feature a new multiple-quantum NMR technique applied to the study of strontium-doped calcium fluorapatite and stoichiometric calcium fluorapatite. Multiple-quantum NMR refers to a class of experiments designed to create and detect multiple-quantum coherences among sets of coupled spins in solids. When a single pulse of rf energy is applied to a sample there is a coherent phase relationship between the magnetization vectors of each of the spins in the sample and the collective behavior of all the spins results in the emission of radiation. In such a sample, a single quantum coherence is said to have been created. If there are groups of n tightly-coupled spins in a sample (for instance n spins on the same molecule), up to n-quantum coherences can be created by the appropriate excitation pulse sequence. The multiple quantum experiments featured in sections IV and V are designed to examine multiple-quantum coherence growth in spins in certain specific orientations of crystallites in a powder pattern, by selecting specific frequencies in a chemical shielding powder pattern. We will refer to such experiments as chemical-shift-selective multiple-quantum NMR experiments.

In section IV chemical-shift-selective MQ NMR is used to probe the distance scale over which the chemical shielding tensors of spins in a lattice maintain the same orientation and/or magnitude. This new experiment is demonstrated on a sample of fluorapatite that has one of every ten calcium ions replaced by a strontium ion. The strontium ions in the lattice have the effect of changing the shielding tensors of neighboring ^{19}F spins, creating, in effect, clusters of unperturbed ^{19}F spins separated by strontium-perturbed spins. The length of these clusters of unperturbed ^{19}F spins is probed by observing the growth of multiple quantum coherence among sets of like spins. Since the strontium-perturbed spins cannot enter the coherence because of their large frequency offsets, the limited coherence growth reflects the finite size of the clusters of like spins.

In section IV the chemical-shift-selective MQ-NMR technique is used to study the difference between multiple-quantum growth dynamics of crystallites associated with different positions in the powder pattern. Chemical-shift-selective MQ-NMR results on different peaks in the powder pattern are presented that demonstrate that MQ coherence growth is faster in classes of crystallites with larger dipolar couplings between adjacent spins. Section IV also contains a description of an experiment that should be able to show the difference between the MQ growth dynamics in linear (1-D) and planar (2-D) arrangements of spins in fluorapatite. The fluorine nuclei in fluorapatite can be viewed as linear columns of uniformly spaced spins that extend the entire length of the crystal, neglecting the possible occurrence of vacancies or substitutions. On the other hand, each column of fluorine nuclei is surrounded by six other columns creating planes of spins perpendicular to the columns with each spin in the plane having six nearest neighbors. By performing chemical shift selective MQ experiments on peaks in the powder pattern associated with crystallite orientations that have relatively different strengths of dipolar

couplings among planar spins or linear spins, differences in linear and planar MQ growth dynamics might be observed.

I.2 Apatite Structure and Chemistry

Apatites are a class of minerals having the general formula $M_{10}X_2(YO_4)_6$, where M is an alkaline earth metal ion, X is a halogen or hydroxyl ion, and Y is an element near the metal-nonmetal transition line on the periodic table. Apatites are found in nature as calcium phosphates in mineralized tissue such as teeth and bones, as well as calcium fluorapatite in the Earth's crust as a major phosphate ore. Some important technological application of apatites include halophosphate phosphors in fluorescent lamps, a gain medium in lasers, and calcium hydroxyapatite chromatography materials. However, most apatite ore is converted to other phosphates such as $Ca(H_2PO_4)_2.H_2O$ and $Ca_2PO_4(OH).2H_2O$, which are in turn used for food processing or as fertilizers.[2] In this thesis the variations of apatites that will be examined include:

$M = Ca^{+2}, Sr^{+2}, Ba^{+2}$

$X = F^{-1}, Cl^{-1}, OH^{-1}$

$Y = P^{+5}, As^{+5}, (Si^{+4}, S^{+6})[1]$
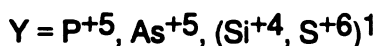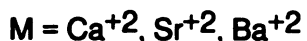
Apatite solid solutions can be created by synthesizing an apatite containing more than one of the cations and/or anions shown above. Four mixed apatite systems that will be examined in this work include: strontium and calcium in the M positions; silicon, sulfur, and phosphorus in the Y position; and arsenic and phosphorus in the Y position. Apatites can be synthesized in the laboratory either by the firing of mineral precursors in a quartz tube furnace or by aqueous precipitation. All of the samples in this study were synthesized by the firing method.

In this thesis most of the sections focus on dopants in calcium fluorapatite $[Ca_5F(PO_4)_3]$, so the details of its structure are important to the arguments that will

be presented. The apatite structure, obtained from x-ray crystallography,[3] features linear chains of uniformly-spaced fluoride ions parallel to the c axis and extending the length of the crystal (Figure I-1). There are two types of calcium ions in the structure, labeled Ca(1) and Ca(2), in the ratio of 4:6. Surrounding each fluoride ion is an equilateral triangle of crystallographically equivalent Ca(2) ions that lie in a plane perpendicular to the fluoride chain. Adjacent triangles of Ca(2) ions are rotated by 60° about the chain axis, creating a hexagonal screw axis in the structure. Adjacent to these Ca(2) sites are crystallographically equivalent phosphate tetrahedra. Finally, there are columns of Ca(1) ions running parallel to the c axis, each calcium column in the middle of an equilateral triangular prism formed by three fluoride columns.
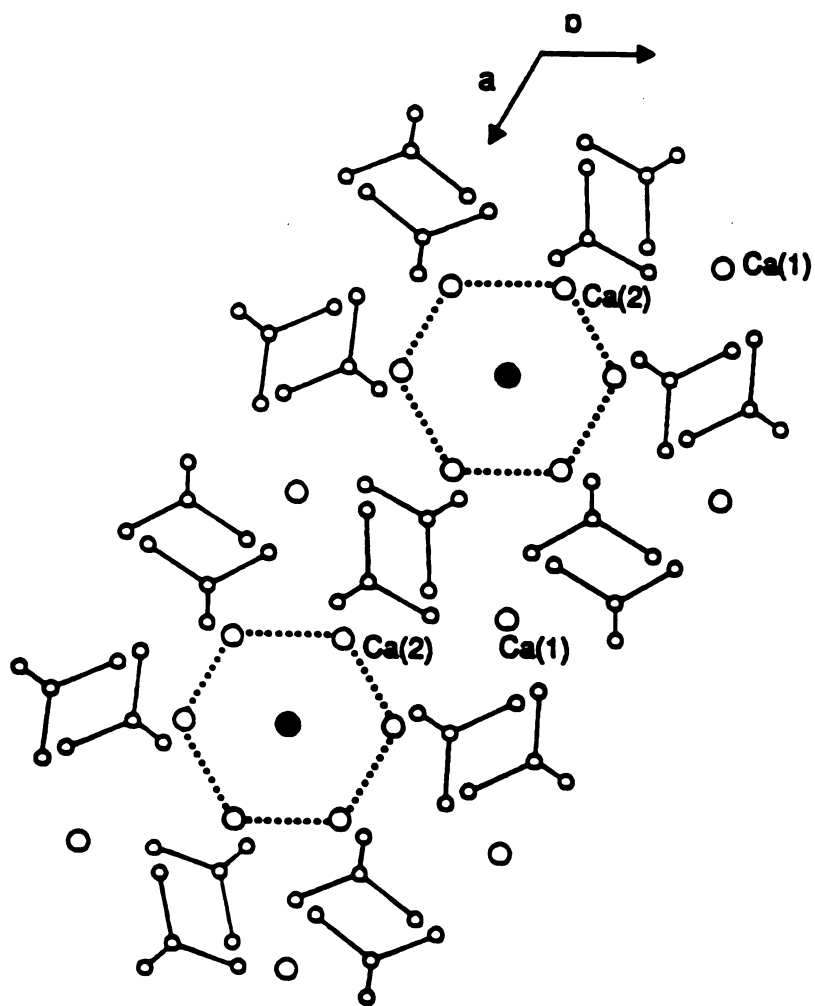
Figure I-1. Schematic drawing of the fluorapatite structure. Calcium ions (large open circles), fluoride ions (black dots), and phosphate groups (small open circles connected by lines). See text. Figure adapted from reference 4.

I-3 NMR Background

I-3.1 The Nuclear Spin Hamiltonian

The nuclear spin Hamiltonian has a well known form, involving some parameters that are generally measured rather than calculated quantum-mechanically using electronic wavefunctions (viz. the chemical shielding, scalar coupling, and quadrupole coupling). The Hamiltonian determines both the eigen frequencies of the NMR spectrum and, through time-dependent quantum mechanics, evolution of the spin system in time. The nuclear spin Hamiltonian is complete enough, and at the same time often simple enough, that it can actually be used to develop new NMR experiments before trying them in the laboratory. In this section the important terms in the nuclear spin Hamiltonian will be described and their effect on NMR lineshapes in solids will be illustrated through simulated spectra.

The nuclear spin Hamiltonian can be written as

$$\mathcal{H} = \mathcal{H}_{Zeeman} + \mathcal{H}_{RF} + \mathcal{H}_S + \mathcal{H}_D + \mathcal{H}_Q + \mathcal{H}_J + \mathcal{H}_{other} \qquad (I-1)$$

where $\mathcal{H}_{Zeeman}$ is the term for the Zeeman interaction of spins with the large applied static magnetic field, $\mathcal{H}_{RF}$ is the term for the Zeeman interaction of the spins with an applied linearly polarized magnetic field oscillating at rf frequencies, $\mathcal{H}_S$ is the term for the chemical shielding at the nucleus, $\mathcal{H}_D$ is the dipolar coupling term between pairs of spins, $\mathcal{H}_Q$ is the nuclear electric quadrupole coupling term (for $I > 1/2$), and $\mathcal{H}_J$ is the indirect coupling (scalar) term between pairs of spins. The term $\mathcal{H}_{other}$ represents other interactions such as spin-rotation coupling or coupling between nuclear spins and electron spins. These terms will not be addressed due to lack of relevance to this work. The first two terms in Eqn. I-1 are often referred to as the external Hamiltonian because they contain the applied fields that are under experimental control. The remaining terms in Eqn. I-1 are usually referred to as the internal portion of the Hamiltonian because they reflect the local environment of the

spins and depend on the sample. The only internal interactions that not are averaged out by rapid diffusion and tumbling in liquids are the (isotropic or scalar) chemical shift and (scalar) J coupling terms; however, all of these interactions can manifest themselves in solids as line broadenings.

I-3.1.1 Zeeman and Chemical Shielding Hamiltonian Interactions

It is convenient to treat the Zeeman and chemical shielding terms in Eqn. I-1 together since the shielding term is simply a correction to the applied magnetic field at the nuclei that depends on the local electronic environment of the spin. The combined Zeeman and shielding Hamiltonian has the form

$$H_{Zeeman} + H_{\sigma} = -\gamma \underline{I} \cdot (1-\underline{\sigma}) \cdot \underline{B}_0 \qquad \text{I-2})$$

where γ is the magnetogyric ratio of the nuclei, $\underline{I}$ is an angular momentum vector operator (I_x, I_y, I_z), $\underline{B}_0$ is the applied magnetic field. $\underline{\sigma}$ is a second-rank Cartesian tensor that describes the shift of the nuclei at various orientations of the molecule with respect to the applied field. The shielding tensor is generally not symmetric but the effects of the difference between elements on opposite sides of the diagonal (σ_{ij} and σ_{ji}) are insignificant at high fields and can be neglected. Since the shielding tensor can be approximated as being symmetric at high field, a reference system can be chosen such that the shielding tensor takes the diagonal form

$$\underline{\sigma} = \begin{bmatrix} \sigma_{xx} & 0 & 0 \\ 0 & \sigma_{yy} & 0 \\ 0 & 0 & \sigma_{zz} \end{bmatrix}. \qquad \text{I-3})$$

This reference frame is called the principal axis system. There are a few definitions and conventions for the values of the components of the shielding tensor. The isotropic chemical shift can be defined as $1/3\mathrm{Tr}\ \sigma = 1/3(\sigma_{xx} + \sigma_{yy} + \sigma_{zz}) = \sigma_{iso}$. The isotropic shift is the average shift the spin would experience in the liquid state if the molecular reference frame were subject to rapid isotropic tumbling motion. By convention the principal axes of the shielding tensor are chosen such that

$$\left|\sigma_{ZZ} - \sigma_{iso}\right| \geq \left|\sigma_{XX} - \sigma_{iso}\right| \geq \left|\sigma_{YY} - \sigma_{iso}\right|.$$

We can now define two useful quantities; the anisotropy of σ, δ, which is given by the formula

$$\delta = \sigma_{ZZ} - \sigma_{iso}$$

and the asymmetry parameter, η, given by the equation

$$\eta = \frac{\left|\sigma_{XX} - \sigma_{YY}\right|}{\delta}.$$

The asymmetry parameter can vary from 0 (for axially symmetric tensors) to 1.

We can attach a physical meaning to the values on the diagonal of the matrix in Eqn. I-3. The reference system in which Eqn. I-3 is diagonal is related to the laboratory frame such that when the z axis of the principal axis system is parallel to the applied field, the shift of the spin is given by σ_{zz} (furthest down field). When the x or y axes of the principal axis system are coincident with $\underline{B}_0$ the shift of the spin would be σ_{xx} or σ_{yy} respectively. Furthermore, the shielding tensor in the principal axis system can be related to the shielding tensor in the laboratory frame by the orthogonal transformation $\underline{R}$:

$$\underline{\sigma}(LAB) = \underline{R}\ \underline{\sigma}(PAS)\ \underline{R}$$

where R_{ij} is equal to the cosine of the angle between the i-axis of the lab frame and the j-axis of the principal axis system. When all orientations of the chemical shielding tensor with respect to $\underline{B}_0$ are present, such as is true in a polycrystalline sample, the resulting distribution of shifts is usually referred to as the chemical shielding powder pattern. As an illustration of these so-called "powder-patterns", Figure I-2a is a simulated spectrum of a powder sample with an axially symmetric chemical shielding tensor ($\eta = 0$) with the same chemical shielding anisotropy and isotropic chemical shift (w. r. t. hexamethylbenzene) as the ^{19}F spins in calcium fluorapatite. The downfield edge of this pattern has the shift $\sigma_{zz} = 120$ ppm and the

intense edge has a shift of σ_{yy} = 36ppm, which is also equal to σ_{xx} in this case. Figure I-2b is an illustrative chemical shielding powder pattern for a spin with three distinct principal shielding components located at the three singularities, as shown.
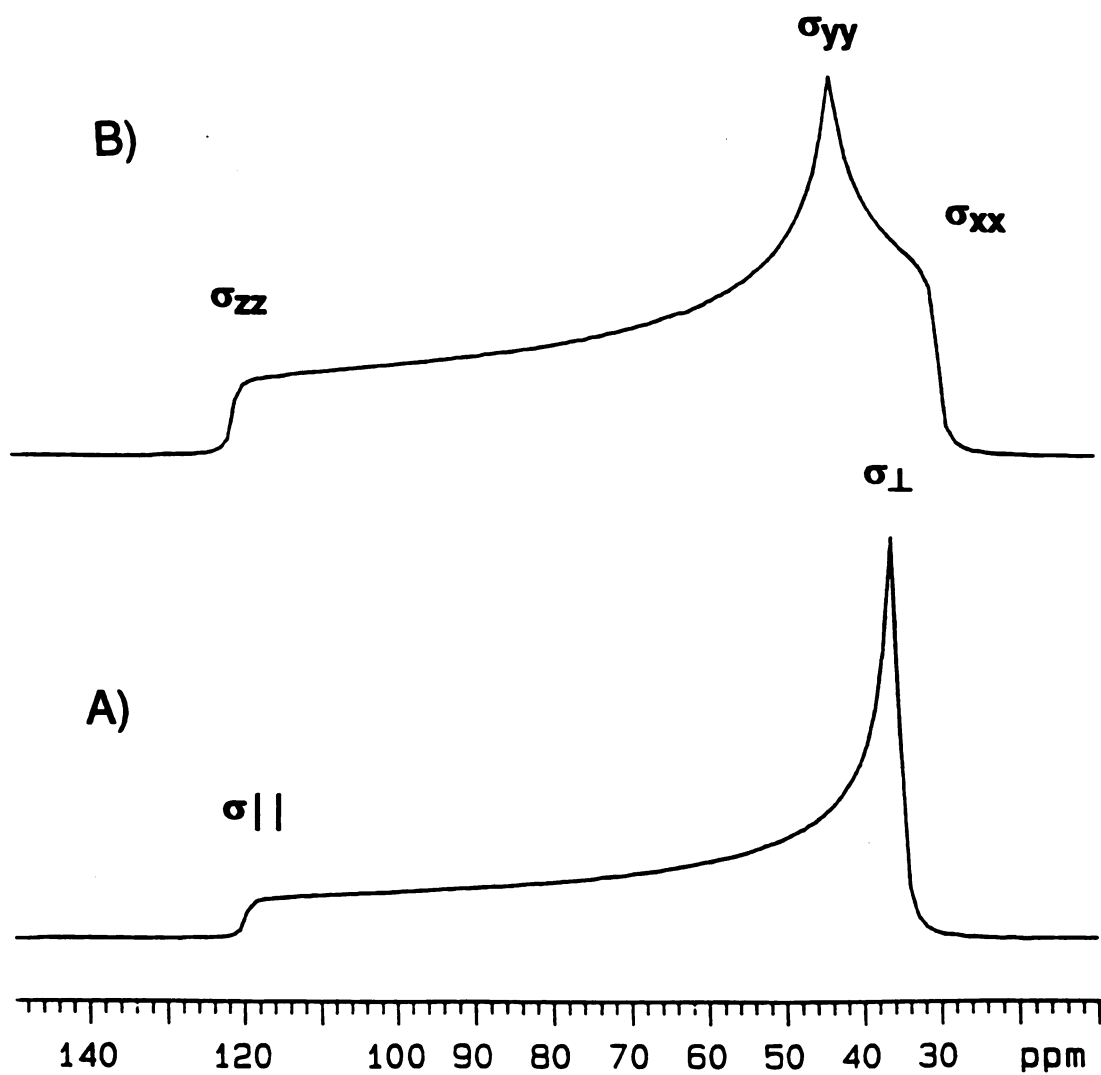
Figure I-2. Simulated chemical shielding powder patterns: (a) axially symmetric shielding tensor with CSA = 84 ppm and η = 0 ; (b) non-axially symmetric shielding tensor with CSA = 84 ppm and η = 0.24. An exponential apodization function corresponding to a 400 Hz line broadening was applied to the simulated FID before Fourier transformation.

I-3.1.2 Dipolar Coupling Hamiltonian

The dipole-dipole coupling term describes the energy of interaction between the magnetic dipoles of spins. The energy of interaction between two interacting magnetic moments is given by the expression

$$E = \frac{\mu_1 \cdot \mu_2}{r^3} - \frac{3(\mu_1 \cdot r)(\mu_2 \cdot r)}{r^5} \qquad \text{I-4)}$$

where r is the vector from the first nucleus to the second nucleus, and r is the length of r. The magnetic moment vectors, μ_1 and μ_2, are given by the equations $\mu_1 = \gamma \hbar I_1$ and $\mu_2 = \gamma \hbar I_2$ respectively. The quantum mechanical Hamiltonian for N interacting spins can be written as

$$H_D = \frac{1}{2} \sum_{j=1}^{N} \sum_{k=1}^{N} \left[\frac{\mu_j \cdot \mu_k}{r_{jk}^3} - \frac{3(\mu_j \cdot r_{jk})(\mu_k \cdot r_{jk})}{r_{jk}^5} \right] \qquad (j \neq k). \qquad \text{I-5)}$$

The magnitude of the small fields from other spins is typically on the order of several Gauss, which is approximately 10^{-5} times the size of the field of a commercial NMR magnet. Expressed in terms of Cartesian spin vectors and tensors the dipole coupling Hamiltonian takes the form

$$H_D = \sum_{j<}^{N} \sum_{k}^{N} \gamma_j \gamma_k I_j \cdot R \cdot I_k \qquad \text{I-6)}$$

where R is the dipolar coupling tensor given by

$$R = \begin{bmatrix} r^2 - 3x^2 & -3xy & -3xz \\ -3xy & r^2 - 3y^2 & -3yz \\ -3xz & -3yz & r^2 - 3z^2 \end{bmatrix}$$

where r is the length of a vector r pointing from one spin to another and x, y and z are the components of a unit vector parallel to r. When the Cartesian components in R are replaced by their equivalent expressions in polar coordinates:

x = r sin θ cos φ

y = r sin θ cos φ

z = r cos θ

equation I-6 takes the form

$$H_D = \sum_{j<}^{N} \sum_{k}^{N} \frac{h\gamma_j\gamma_k}{r_{jk}^3}[A+B+C+D+E+F]$$

$$A = (1-3\cos^2\theta)I_{jz}I_{kz}.$$ (I-6b)

$$B = \frac{1}{2}(1-3\cos^2\theta)(I_{jz}I_{kz} - I_j \cdot I_k)$$

The terms through C through F in Eqn. I-6b are given elsewhere [5] and are typically neglected since their effects on the eigenfrequencies are negligible for high field NMR. The term θ in Eqn. I-6b is the angle between the internuclear vector and the applied field B_0. The Hamiltonian shown in Eqn. I-6b written with the "A" and "B" terms takes the form:

$$H_D = \sum_{j<}^{N} \sum_{k}^{N} \frac{h\gamma_j\gamma_k}{r_{jk}^3}(1-3\cos^2\theta_{jk})\left[I_{zj}I_{zk} - \frac{1}{2}(I_{xj}I_{xk} + I_{yj}I_{yk})\right].$$ (I-7)

The "dipolar coupling" D_{jk} between a specific pair of nuclei is the quantity;

$$D_{jk} = \frac{h\gamma_j\gamma_k}{2\pi r_{jk}^3}(1-3\cos^2\theta_{jk}).$$

The value of the dipolar coupling is 1.20067×10^5 Hz for two protons separated by one angstrom with $\theta_{jk} = 90°$.

The effect of the dipole-dipole coupling interaction on an ^{19}F resonance for a pair of fluorine spins is shown in Figure I-3. The pair of spins is separated by a distance of 344 pm, the crystallographically determined distance between the fluorine spins in the chains of fluorine found in fluorapatite. The strength of the dipolar coupling between neighboring fluorine spins is relevant to the spin diffusion measurements and multiple-quantum NMR experiments in subsequent sections. Figure I-3a is a spectrum calculated for a pair of ^{19}F spins having $\theta_{jk} = 90°$. The splitting between the two peaks is equal to three halves of the coupling (D_{F-F}), which is equal to 3.9 (KHz). Figure I-3b is a powder spectrum of a pair of ^{19}F spins with a statistical distribution of orientations θ_{jk} present. This powder pattern distribution of spins is usually referred to as a Pake doublet. [6]
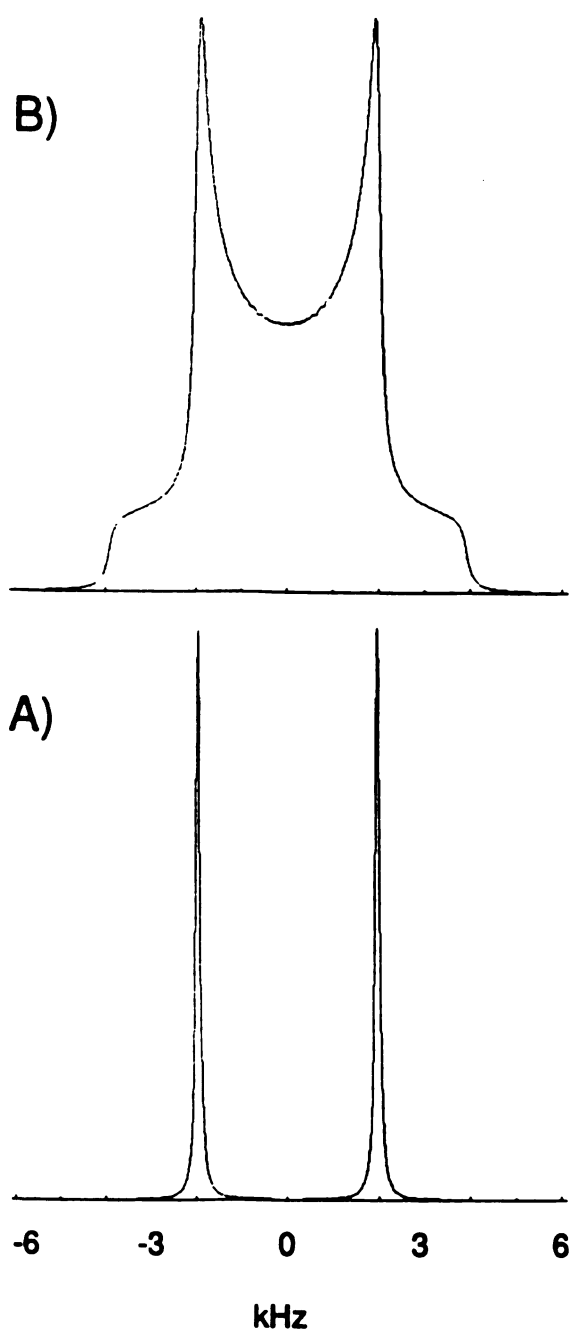
Figure I-3. Simulated spectra of a ^{19}F spin pair separated by 344 pm at 9.4 T: (a) internuclear vector oriented perpendicular to the applied field; (b) powder pattern spectrum.

I-3.1.3 Indirect Dipole Coupling

The indirect dipole coupling, or "J" coupling as it is called, refers to coupling to the magnetic dipole moment of a nearby spin transmitted through the Zeeman order of valence electrons between the nuclei as shown in the diagram below.

electron spins
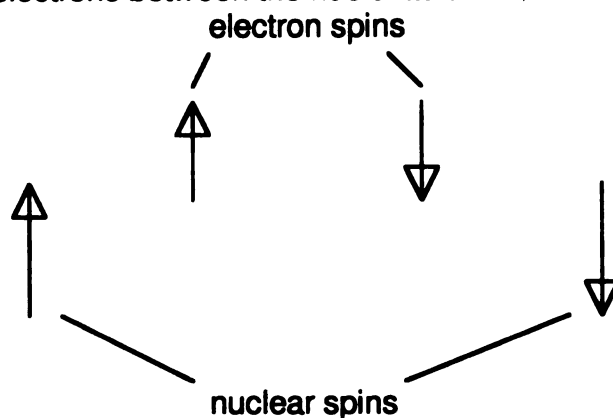
nuclear spins

The nuclear spins are pictured in the antiparallel orientation but can also have a parallel orientation. The indirect coupling Hamiltonian written in Cartesian form is

$$H_D = \sum_{j<}^{N} \sum_{k}^{N} \gamma_j \gamma_k I_j \cdot J \cdot I_k \qquad \text{I-8}$$

where J_{jk} is the indirect coupling tensor. Unlike the direct dipolar coupling tensor, the J tensor is generally not traceless, which results in splittings of peaks in the spectra of isotropic liquids.

If this Hamiltonian is recast eliminating nonessential terms for the high field limit we get the following form:

$$H_J = \sum_{j<}^{N} \sum_{k}^{N} J_{jk} I_j \cdot I_k + \sum_{j<}^{N} \sum_{k}^{N} J^{aniso}_{jk} [I_{zj} I_{zk} - \frac{1}{2} (I_{xj} I_{xk} + I_{yj} I_{yk})] \qquad \text{I-9}$$

where the two terms are the isotropic and anisotropic portions of the Hamiltonian respectively. The magnitude of J can range in size from less than one Hz all the way to many KHz. In Section II, an attempt is made to observe any "J" coupling between the fluorine spins as a possible source of spin diffusion. Unlike the direct dipolar coupling, the scalar coupling does not scale as $1/r^3_{ij}$ and does not depend explicitly upon r_{ij}. Therefore, if the magnitude of "J" coupling is substantial

compared to the direct dipolar coupling, determination of internuclear distances based on spin diffusion experiments would not be possible.

I-3.1.4 Quadrupole Hamiltonian

The quadrupolar term in the Hamiltonian describes the energy of interaction of a nonspherical nucleus with an electric field gradient at the nucleus. All nuclei with spin I > 1/2 (the majority of magnetic nuclei) are nonspherical, and are said to be "quadrupolar". The quadrupole term in the nuclear spin Hamiltonian can be written in Cartesian coordinates as follows:

$$H_Q = \frac{eQ}{2hI(2I-1)} \sum_{\alpha,\beta=1}^{3} V_{\alpha\beta} \left[\frac{3}{2} \left(I_\alpha I_\beta + I_\beta I_\alpha \right) - \delta_{\alpha\beta} I^2 \right] \qquad \text{I-10)}$$

where V is a second rank electric field gradient tensor, e is the charge on the electron, Q is the nuclear quadrupole moment, and I is the spin of the nucleus.

I-3.1.5 Radio Frequency Hamiltonian

In NMR, the radio frequency (rf) irradiation applied to the sample has an oscillating (linearly polarized) magnetic field vector perpendicular to the static field. The Hamiltonian for the Zeeman coupling of spins to this field can be described semi-classically by the following time dependent equation:

$$\begin{aligned} H_{rf} &= -2\gamma H_1 \cos(\omega t) I_x \\ &= -2\omega_1 \cos(\omega t) I_x \end{aligned} \qquad \text{I-11)}$$

where H_1 is the linearly polarized magnetic field vector rotating at a frequency ω and ω_1 is the precession frequency of the spins about the H_1 vector. Since it is easier to treat a time-independent Hamiltonian, Eqn I-11 is usually recast in a reference frame rotating about the z axis at the rf frequency ω. In this rotating frame the rf Hamiltonian simplifies to the following form;

$$H_{rf}(rot) = -\omega_1 I_x \qquad \text{I-12)}$$

 A physical consequence of Eqn. I-12 is that when the rf irradiation is applied, the magnetization vector of the spins on resonance precesses about the x axis of the rotating frame at the frequency ω_1. This behavior is not true of the spins that are not on resonance (not resonant at ω). Instead, these spins precess about the effective field given by the equation

$$\underline{H}_{\mathit{eff}} = (\underline{H}_0 - \omega/\gamma) + \underline{H}_1 \qquad \text{I-13)}$$

where the quantity $(\underline{H}_0 - \omega/\gamma)$ is the component of the effective field along the z axis. The physical consequence of Eqn. I-13 will be discussed in section II in reference to creating frequency selective excitation experiments.

I-3.2 The Density Matrix

As shown in examples given in the previous section, the nuclear Hamiltonian can be used to compute the eigenfrequencies and therefore the NMR spectra of spin systems. With a well-described Hamiltonian and complete set of wave functions, the time development of a measurable property of a spin system can be computed by using the Liouville equation. Such a computation can be streamlined by placing all of the coefficients of the wave functions of a spin system into an array called the density matrix (more generally, in a basis-independent form, a density operator). This density operator contains all the information necessary to describe any measurable property (observable) of the spin system. For a large ensemble of spin systems an ensemble average of products of coefficients is used. In this section (I-4) the equilibrium density matrix for spins in a large applied magnetic field will be given and a connection between diagonal elements of the density matrix and polarization (z magnetization) will be made. Furthermore, a connection between the off diagonal elements of the density matrix and other observables a spin system can have, such as transverse magnetization and

multiple quantum coherences will be made. Portions of the following description of the density matrix are adapted from reference 7 (chapter 5.4).

The procedure to compute an observable is to evaluate the inner product of some operator corresponding to the desired observable with the wave function. For instance, the expectation value of the x component of the spin angular momentum would be

$$\langle I_x \rangle = \langle \psi(t) | I_x | \psi(t) \rangle. \tag{I-14}$$

The time dependent wave functions are usually written as

$$\psi(t) = \sum_j c_j(t) \phi_j \tag{I-15}$$

where ϕ_j is an orthonormal set of basis functions with time dependent coefficients $c_j(t)$. Evaluating an expectation value as in Eqn. I-14 would be done by taking the following sum;

$$\langle I_x \rangle = \sum_{j,k} c_k^*(t) c_j(t) \langle \phi_k | I_x | \phi_j \rangle. \tag{I-16}$$

All of the information about the time dependence of the observable $\langle I_x \rangle$ is carried in the products of coefficients of the matrix elements $c_k^* c_j$, since the matrix elements $\langle \phi_k | I_x | \phi_j \rangle$ themselves do not change with time. The products $c_k c_j^*$ can be arranged into a matrix. It is convenient to think of the matrix $c_k c_j^*$ as being the representation of an operator P, the operator defined by its matrix elements:

$$\langle \phi_j | P | \phi_k \rangle = c_j c_k^* \tag{I-17}$$

The expectation value of I_x can be written as in eqn I-16 with coefficients of the matrix elements written as shown in Eqn. I-17:

$$\langle I_x \rangle = \sum_{k,j} \langle \phi_k | P | \phi_j \rangle \langle \phi_k | I_x | \phi_j \rangle. \tag{I-18}$$

The result of the operator P acting on a function ϕ_k may be written as

$$P \phi_j = \sum_k a_k \phi_k \tag{I-19}$$

since the ϕ_k's form a complete basis set. As usual we find the coefficients a_k by multiplying both sides from the left by ϕ_k^* and integrating:

$$a_k = \int \phi_k^* P\phi_j = \langle \phi_k | P | \phi_j \rangle \quad \text{so that} \qquad \text{I-20)}$$

$$P\phi_k = \sum_k \phi_k \langle \phi_k | P | \phi_j \rangle \qquad \text{I-21)}$$

Likewise we have

$$I_x\phi_k = \sum_k \phi_k \langle \phi_k | I_x | \phi_j \rangle \qquad \text{I-22)}$$

therefore

$$I_x\phi_k = \sum_k \phi_k \langle \phi_k | I_x | \phi_j \rangle \qquad \text{I-23)}$$

and

$$PI_x\phi_k = \sum_k P\phi_k \langle \phi_k | I_x | \phi_j \rangle$$
$$= \sum_{j,k'} P\phi_{k'} \langle \phi_{k'} | P | \phi_j \rangle \langle \phi_j | I_x | \phi_k \rangle \qquad \text{I-24)}$$

so that

$$\langle \phi_{k'} | PI_x | \phi_k \rangle = \sum_j \langle \phi_{k'} | P | \phi_j \rangle \langle \phi_j | I_x | \phi_k \rangle$$

By using Eqn. I-23 , we find that

$$\langle I_x \rangle = \sum_{j,k} \langle \phi_k | P | \phi_j \rangle \langle \phi_j | I_x | \phi_k \rangle$$
$$= \sum_{j,k} \langle \phi_j | PI_x | \phi_k \rangle \qquad \text{I-25)}$$
$$= Tr\{PI_x\}.$$

In words this simply states that the expectation value of an observable is the trace of the product of the density operator and the operator corresponding to the observable. Since $\langle \phi_k | P | \phi_j \rangle = \langle \phi_j | P | \phi_k \rangle^*$ the density operator is Hermitian.

Until now we have been describing an operator P which is defined (as in Eqn.I-17) by the wave functions of a single spin system and contains the information required to compute observables of that spin system. In many NMR problems (and all of those in this work) we are concerned with computing the average expectation value of an ensemble of spin systems. This is generally the

case since the sample in most high field NMR studies contains a large number of spins (ca. 10^{16} -10^{23}). However, some experiments [8] do detect the properties of single spins. In a large collection of spin systems, the coefficients $c_k c_j^*$ will vary from system to system since each spin system has a unique set of wave functions, but the matrix elements $\langle \phi_j | I_x | \phi_k \rangle$ will be the same. If we use a bar to denote the ensemble average, we have, then,

$$\overline{\langle I_x \rangle} = \sum_{j,k} \overline{c_k^*(t) c_j(t)} \langle \phi_k | I_x | \phi_j \rangle . \tag{I-26}$$

The quantities $\overline{c_k^*(t) c_j(t)}$ form a matrix, and it is this matrix that we call the "density matrix". We shall consider it to be a matrix of an operator ρ, defined by the equation

$$\langle \phi_k | \rho | \phi_j \rangle = \overline{c_k^* c_j} = \overline{\langle \phi_k | P | \phi_j \rangle} . \tag{I-27}$$

Similar to equation I-25, ρ can be used to compute an ensemble average expectation value in the following manner:

$$\overline{\langle I_x \rangle} = \sum_{j,k} \langle \phi_j | \rho | \phi_k \rangle \langle \phi_k | I_x | \phi_j \rangle = Tr \{ \rho I_x \} . \tag{I-28}$$

Having established how to compute an observable of the spin system, we will now examine how to calculate the evolution of the density matrix under the influence of a Hamiltonian. By the Liouville equation:

$$\frac{d\rho}{dt} = i[\rho, H] . \tag{I-29}$$

In the event that H is independent of time, we may obtain a formal solution of Eqn. I-29:

$$\rho(t) = e^{-iHt} \rho(0) e^{iHt} \tag{I-30}$$

If the Hamiltonian is time dependent, it can be approximated by a string of time-independent H_j operating for very short intervals:

$$H_j = \left(\frac{1}{\Delta t}\right) \int_{t_j}^{t_j + \Delta t} H(t)\,dt$$ \hfill I-31)

In order to begin computing the evolution of the spin system we must first know where it starts by describing the initial properties of the ensemble of spin systems (i. e. the equilibrium density matrix). Off diagonal elements $\rho_{jk} = \overline{c_j c_k^*}$ are the average products of two different complex numbers. At equilibrium there is no reason to expect a special phase relationship, and hence the off diagonal elements would each have a value of zero (by the random-phase hypothesis) .[7] Diagonal elements describing populations should at equilibrium satisfy a Boltzman distribution:

$$\rho(0) = \overline{c_j c_j^*} = \frac{e^{-iE_j/kT}}{Z}$$ \hfill I-32)

where Z is the partition function

$$Z = \sum_k {}^{-E_k}\!\!\Big/\!_{kT}$$ \hfill I-33)

For concreteness, the equilibrium density matrix for ^{19}F in a 14.1 Tesla field (500 MHz spectrometer) at 298 K evaluated in the m basis states { $|\alpha\rangle$, $|\beta\rangle$ }would be:

$$\rho(0) = \begin{bmatrix} 1.00000453 & 0.0 \\ 0.0 & 0.99999547 \end{bmatrix}.$$ \hfill I-34)

If we expand the exponential in eqn-32,

$$\rho(0) = \left(\frac{1}{Z}\right)(1 + \omega_0 I_z / kT)$$ \hfill I-35)

we notice the equilibrium density matrix can be decomposed into the unity matrix and a term proportional to I_z (higher power terms of I_z can be dropped since they are very small). Since the unity matrix does not change under unitary transformations, it is simply dropped to simplify calculations; the resulting matrix is referred to as the reduced density matrix.

To compute the z-magnetization from the equilibrium density matrix in Eqn. I-35 we simply multiply by I_z and take the trace;

$$\langle I_z \rangle = Tr\{\rho I_z\} = \rho_{\alpha\alpha} - \rho_{\beta\beta}.$$ I-36)

Thus, the difference of the diagonal elements is proportional to the polarization.

Having shown that the diagonal components of the density matrix are related to z-magnetization, we can now discuss which elements correspond to transverse (x and y) magnetization. The elements that are immediately off the diagonal correspond to transverse magnetization. For example the reduced density matrix for a two spin system evaluated in the m-basis states after a single 90° (x) non-selective pulse would take the form:

$$\rho(t) = \begin{bmatrix} 0.0 & * & 0.0 & 0.0 \\ 0.0 & 0.0 & 0.0 & 0.0 \\ 0.0 & 0.0 & 0.0 & * \\ 0.0 & 0.0 & 0.0 & 0.0 \end{bmatrix}$$ I-37)

with the asterisks denoting nonvanishing elements. Often the presence of such density matrix elements are referred to as single quantum coherences. They have the label single, because they connect states that vary by one unit of total angular momentum. The word coherence is used because the spin systems in the ensemble of spin systems have a coherent phase relationship. The question that logically follows is: what do the other elements of the density matrix correspond to? The first thing to observe is that they do not correspond to properties that are directly observable in the laboratory such as transverse magnetization (immediate off-diagonal elements). The other off diagonal elements are generally referred to as multiple quantum or zero-quantum coherences and must be detected indirectly by converting them into observable magnetization. The density matrix of a two spin system;

$$\rho(t) = \begin{bmatrix} 0.0 & 0.0 & 0.0 & * \\ 0.0 & 0.0 & 0.0 & 0.0 \\ 0.0 & 0.0 & 0.0 & 0.0 \\ * & 0.0 & 0.0 & 0.0 \end{bmatrix} \qquad \text{I-38)}$$

has two elements associated with double quantum coherences indicated here by asterisks. A physical interpretation of an ensemble of two-spin systems with non-vanishing double-quantum elements is that the individual spin systems (spin pairs) would be absorbing and emitting two quanta of angular momenta in a synchronous fashion. The existence of nonvanishing double quantum matrix elements as in Eqn. I-38 is referred to a double quantum coherence. More generally, the presence of an n quantum matrix element is referred to as an n-quantum coherence. We will further discuss the creation and detection of these "multiple quantum coherences" in the next section.

I-3.3 Multiple Quantum NMR

Multiple quantum NMR experiments are used to detect transitions other than "allowed" ($\Delta M = \pm 1$) transitions that correspond to the lines observed in NMR spectra. The simplest example of a multiple quantum transition, or coherence, would be the double-quantum coherence for a coupled spin pair. Figure I-4 is a diagram of the energy levels for a coupled pair of spins with the energy levels labeled 1, 2, 3, 4 as shown. The double quantum transition between the energy levels 1 and 3 is denoted with a dashed line. This transition is labeled a *double* quantum transition because it corresponds to an event whereby the system is absorbing two units of z angular momentum. As discussed in Section I-3 if a double quantum coherence has been created the density operator would contain a nonvanishing element between the states corresponding to energy levels 1 and 3. From this example the utility of MQ-NMR spectroscopy is readily apparent: the maximum MQ coherence is limited by the number of coupled spins in the spin system. For the spin pair described in Figure I-4 a two quantum coherence can be created. However, one can expect to be able to create both double and triple quantum coherence for three spin clusters (such as in a CH_3 group).

In this section (I-5) the double quantum selective NMR pulse sequence for creating and detect MQ coherences will be discussed. Then, a model for determining the size of clusters of spins involved in MQ coherences will be examined and explained in terms of the statistics of MQ transitions available to a spin system.
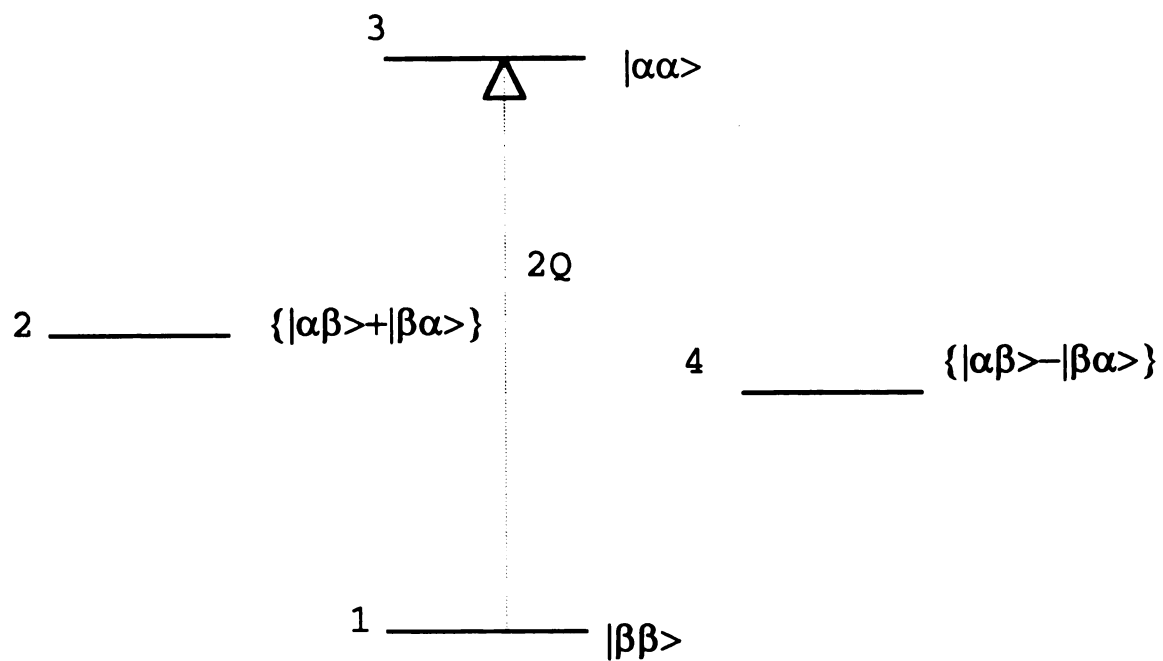
Figure I-4. Energy level diagram for a pair of dipolar coupled spins. The double-quantum transition between levels 1 and 3 is indicated with a dashed line.

I-3.3.1 Detecting MQ Coherences

The pulse sequence[9] use to obtain even-order selective multiple quantum in this work is pictured in Figure I-5. Although the pulse sequence used in this work is actually designed to collect even order coherences, it can obtain odd order coherences with a slight modification.[10] This pulse sequence has four different sections; the preparation period $\tau(U)$, the evolution period t_1, the mixing period $\tau(V)$, and the detection period t_2. The preparation period has the effect of creating multiple quantum coherence among neighboring sets of spins. The average Hamiltonian during the basic eight pulse cycle is given by the formula:

$$\overline{H}_D = \frac{1}{3}\left[H_{yy} - H_{xx}\right]$$

$$= \frac{1}{2}\sum_{j<k} D_{jk}\left(I_{j+}I_{k+} + I_{j-}I_{k-}\right)$$

I-39)

This Hamiltonian has the effect of transferring intensity from the diagonal elements of the density matrix to those related to even order quantum coherences. This transfer process is shown schematically in Figure I-6 for the reduced density matrix of a spin system of two spin 1/2 nuclei. (Note: both even and odd orders are shown to be populated in Figure I-6 for ease of visualization. This would actually only occur under the influence of a non-selective MQ Hamiltonian.) Figure I-6a is the equilibrium density matrix with the various m basis states explicitly given as row and column indices. The equilibrium density has intensity on the diagonal elements which is related to population of spins aligned with the field or z-magnetization (see Eqn. I-36). The statistical mechanical order is moved into the off-diagonal elements of the density matrix corresponding to zero, one, and double quantum coherences
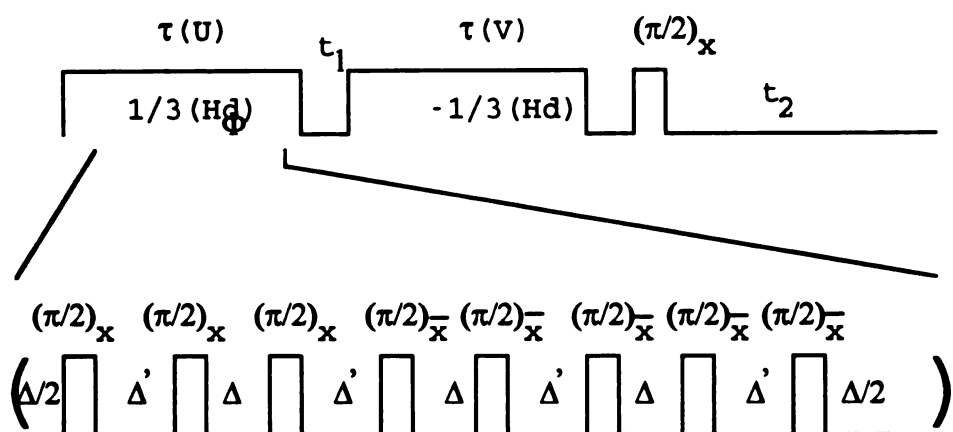
Figure I-5. Even order selective PI-MQ-NMR pulse sequence.
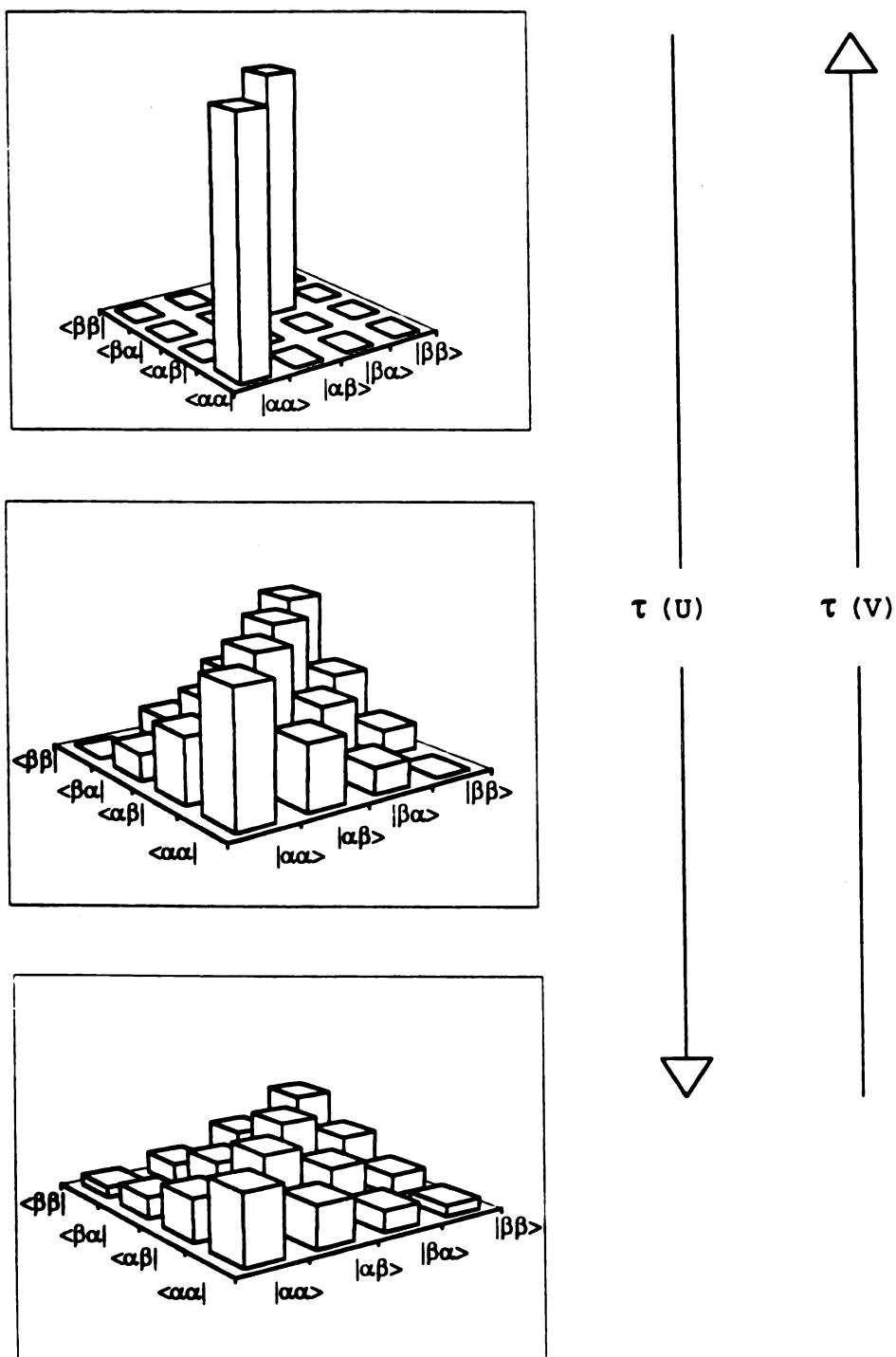
Figure I-6. Bar graph plot showing the flow of multiple-quantum coherence order in a schematic density matrix during the preparation and detection periods (U and V) of the PI-MQ-NMR shown in Figure I-5.

during the preparation period as shown in Figure I-6b and I-6c. The coherence order can be spread equally among the off diagonal elements by lengthening the preparation period. This is done by increasing m, the number of repetitions of the eight pulse cycle shown in Figure I-5.

After the preparation section of the PI-MQ sequence a short delay or evolution period t_1 is inserted to give the NMR spectrometer time to adjust the phase of the rf pulses. This delay is made as small as the NMR hardware will allow (typically 1 μs in this work) so as to avoid decay of coherence order. Next, the mixing period reverses the flow of order created during the preparation period to the diagonal elements as shown in Figure I-6. This time reversal is implemented by changing the x and $\bar{x}$ pulses in the preparation period to y and $\bar{y}$ in the mixing period. The way this pulse sequence actually gains information about the multiple quantum coherence orders that are created, is by incrementing ϕ, the phase of the rf irradiation used for the pulses in the preparation period, while holding the phase of the rf in the evolution period constant. The z-magnetization represented by the intensity of the diagonal elements of the density matrix immediately after the mixing period can be written[9] as:

$$S(\phi, \tau) = \sum_n \sum_{j,k} \left| \Phi_{j,k}(\tau) \right|^2 \exp(in\Delta\phi) \exp(-i\omega_{j,k}t) \qquad \text{I-40)}$$

where $\Phi_{i,j}(\tau)$ are elements of the reduced density matrix and $\omega_{jk} = \omega_j - \omega_j$ is defined as the MQ transition frequency between states j and k. We notice immediately that Eqn. I-40 is a Fourier series in ϕ, leading us to two conclusions. First, a Fourier transform of the data as a function of ϕ yields a "multiple-quantum" spectrum that will have a δ-function peak for each MQ coherence. Second, from the Nyquist sampling theorem, one must sample at twice the "frequency" of the highest order

peak to detect that frequency. This means that in order to obtain a maximum coherence n_{max}, ϕ must be incremented by intervals of $1/2(2\pi/n_{max}) = \pi/n_{max}$.

The final element in the PI-MQ-NMR sequence shown in Figure I-5 is a single nonselective 90° read pulse. The function of this pulse is to convert the ϕ-modulated z-magnetization left after the evolution period V into detectable transverse magnetization. Once transverse magnetization is created, a single complex data pair is typically taken. However, the entire FID can be recorded and transformed to yield information about the growth of MQ coherences in specific peaks in the usual NMR frequency domain f_2 (as will be shown in Section V).

As an illustration of what the data from a PI-MQ-NMR experiment look like, real points of a set of complex pairs as a function of ϕ are shown in Figure I-7a. The data points shown are often referred to as a multiple-quantum interferogram and in this case were collected with ϕ incremented in intervals of 15° allowing for the detection of up to 12-quantum coherences. The Fourier transform of the interferogram yields the MQ-spectrum shown in Figure I-7 b. Each peak in this "spectrum" corresponds to a different coherence order as labeled. As shown in Figure I-7b the coherence orders have greatly differing magnitudes. In the next section we will discuss how to determine the size of the clusters of spins giving rise to such distributions of coherence orders.
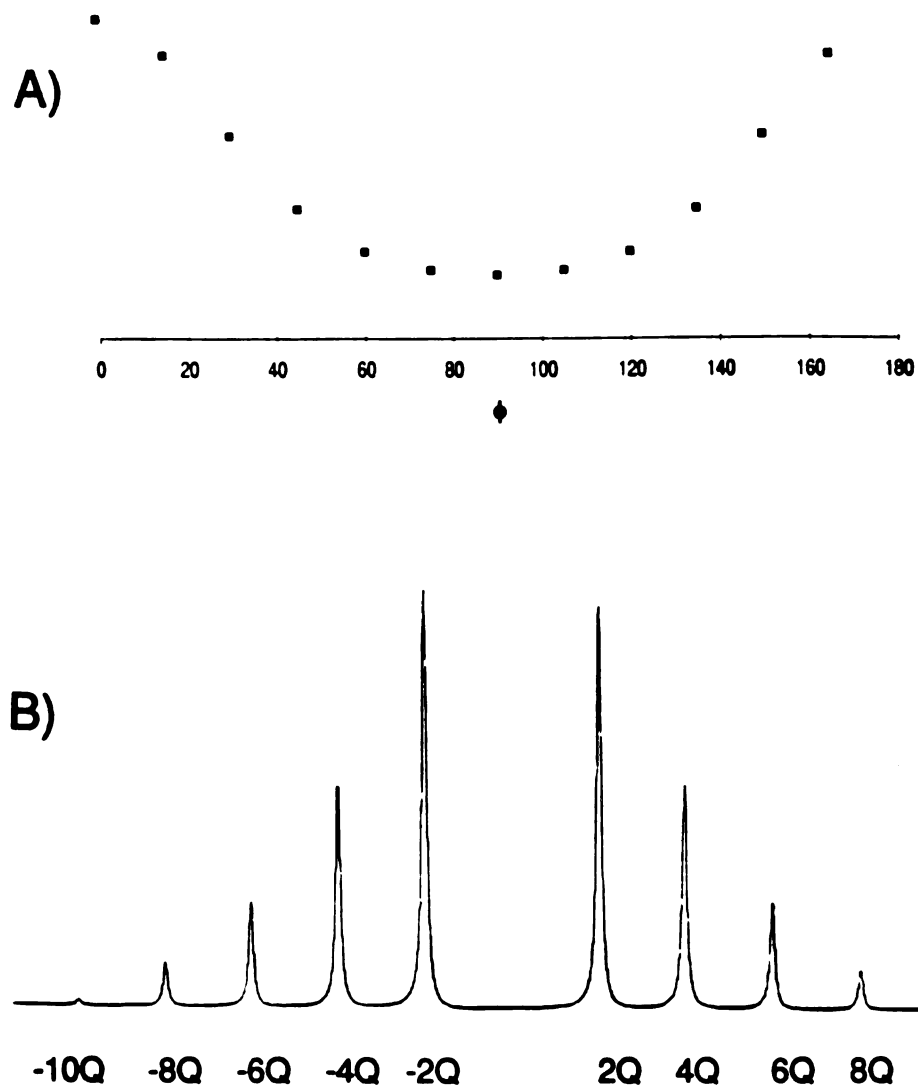
Figure I-7. Data from the PI-MQ-NMR sequence shown in Figure I-5 with ϕ incremented in intervals of 15° to obtain a maximum coherence order of 12; a) ϕ-domain interferogram; b) MQ spectrum .

I-3.3.2 Statistical Model for Coherence Order and the Effective Size Concept.

In the last section the actual pulse sequence for obtaining various coherence order magnitudes was discussed. The end result of this experiment is a multiple-quantum spectrum which consists of a series of peaks for each coherence, each with a distinct magnitude. In this section a model which relates the MQ peak intensity distribution to the size of the clusters of spins in the spin system will be given.[11] Furthermore, the concept of the effective size of the spin system will be developed. "Effective size" is a phrase that refers to the size of the clusters of spins that are participating in MQ coherences in large, essentially infinite lattices of spins. Finally, information that can be gained about geometrical arrangements of spins by examining the growth of the effective size as a function of the preparation time will be detailed. Understanding these MQ growth dynamics experiments is crucial to understanding the studies in Sections V and VI of this thesis.

The magnitude profile of the peaks in a MQ spectrum can be related to the size of the spin system N by considering the number of density matrix elements associated with each coherence.[11,12] This can be illustrated by the example of a three spin system taken from reference 12. A system of three dipole-coupled spin-1/2 nuclei (N=3) has $2^N = 8$ product states. These are explicitly listed as the row and column indices of the schematic density matrix for the system given by:

$$\rho = \begin{array}{c} \\ <\alpha\alpha\alpha| \\ <\alpha\alpha\beta| \\ <\alpha\beta\alpha| \\ <\beta\alpha\alpha| \\ <\beta\beta\alpha| \\ <\beta\alpha\beta| \\ <\alpha\beta\beta| \\ <\beta\beta\beta| \end{array}$$

	$|\alpha\alpha\alpha>$	$|\alpha\alpha\beta>$	$|\alpha\beta\alpha>$	$|\beta\alpha\alpha>$	$|\beta\beta\alpha>$	$|\beta\alpha\beta>$	$|\alpha\beta\beta>$	$|\beta\beta\beta>$
$<\alpha\alpha\alpha|$	0	1	1	1	2	2	2	3
$<\alpha\alpha\beta|$	1	0	0	0	1	1	1	2
$<\alpha\beta\alpha|$	1	0	0	0	1	1	1	2
$<\beta\alpha\alpha|$	1	0	0	0	1	1	1	2
$<\beta\beta\alpha|$	2	1	1	1	0	0	0	1
$<\beta\alpha\beta|$	2	1	1	1	0	0	0	1
$<\alpha\beta\beta|$	2	1	1	1	0	0	0	1
$<\beta\beta\beta|$	3	2	2	2	1	1	1	0

I-41)

where the number at each element is the multiple quantum coherence order associated with that element. The order of a coherence, n, is simply the difference of the z component of the angular momentum m_z between two correlated states. For instance, a transition from the $m_z = -3/2$ state, $\beta\beta\beta$, to the $m_z = +1/2$ state, $\alpha\alpha\beta$, is a +2-quantum transition. The reverse process is a -2-quantum transition. The number of density matrix elements Z_n corresponding to an n-quantum coherence is given by the following eqn:

$$Z_n = \binom{2N}{N - |n|} = \frac{2N!}{(2N - |n|)! |n|!}$$

I-42)

where N is the size of the spin system. In the case of the three spin system (N=3) the possible values of n are 0, ±1, ±2, ±3. The number of elements comprising each order are $Z_0 = 20$, $Z_1 = Z_{-1} = 15$, $Z_2 = Z_{-2} = 6$, $Z_1 = Z_{-1} = 1$. This is easily verified by counting the elements in Eqn I-41 associated with each coherence order.

As we saw in Equation I-40 the actual intensity of an MQ order I(n,t) is dependent on the preparation time τ. When τ is sufficiently long, the coherence

order is spread equally among (or nearly equally) among the elements (see Figure I-6) and the total intensity of the peaks in the MQ spectrum will reflect the number of elements corresponding to a given coherence order. For example, the MQ spectrum of the three spin-1/2 system would contain peaks for each order proportional to the number of the elements Z_n listed above. A schematic stick spectrum of the three spin system at long τ values would appear as follows:
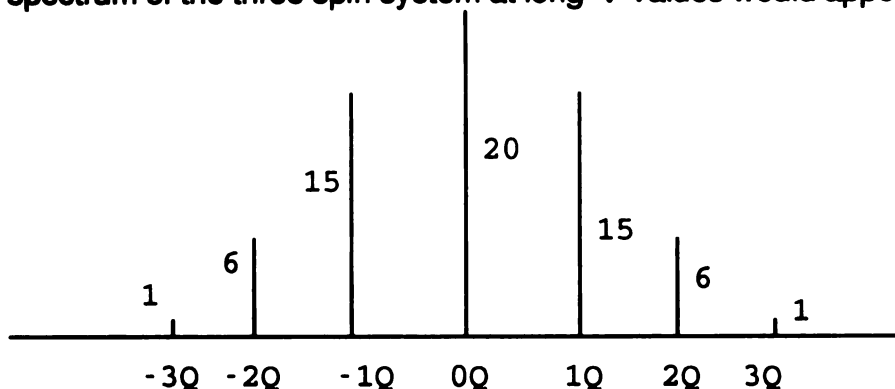
with the intensities of the peaks indicated next to the lines.

From the practical standpoint, this model enables one to "count" the number of spins grouped together in well isolated clusters in a sample using MQ NMR, by recording MQ spectra with increasing preparation times until the intensity profile of the MQ peaks ceases to change as a function of τ. Then the intensities of the MQ peaks are fit to Eqn. I-42 by varying N, thereby giving the size of the cluster of coupled spins in the sample. The Pines group has shown that this "counting" technique can be used to count as many as 21 spins in a cluster in a sample.[13]

If a spin system is not characterized by finite clusters of spins but rather by a large infinite lattice or network, the MQ order will continue to shift toward peaks of higher multiple quantum coherences with increasing τ as larger groups of spins enter coherences. This presents a problem for the statistical model: if the size of the coherent groups of spins is increasing, the statistics of the number of correlated states is changing at the same time. This necessarily obscures any information about the size of coherence clusters of spins. Despite this limitation the peaks in the

MQ spectrum of a sample with large numbers of coupled spins can be fit to Eqn. I-42 (or its Gaussian approximation). The size of the spins system, N, obtained from this fit is usually called the "effective size". The effective size parameter is roughly equivalent to the average size cluster of spins that are in a coherence. [11] It has been pointed out [14] that some deviation from Eqn. I-42 would be expected since spins on the periphery of the cluster have neighbors outside of the coherence.

Some useful information about large spin systems can be gained from measuring the effective size as a function of preparation time. The rate of growth of coherences (and therefore the effective size) as a function of preparation time scales with the dipole-dipole couplings between spins in the sample. Since dipolar couplings depend upon the inverse cube of the internuclear distance, the MQ growth dynamics can yield information about whether spins are agglomerated or dispersed in a sample. Furthermore, it has been shown recently[15] that the dimensionality of spin arrangements (i.e. linear, planar, solid) can be determined from the shape of the MQ growth curve. In this thesis (section V) MQ growth is examined in linear clusters of ^{19}F spins in a doped fluorapatite sample at different orientation with respect to the field. Obtaining orientation dependent MQ spectra is achieved by using a newly-developed MQ-NMR technique that selectively records MQ growth within a specific peak in a powder pattern. In section VI the frequency-selective MQ-NMR technique given in Section V is used to test some of the concepts concerning the dependence of coherence growth on dipolar coupling strength and dimensionality.

I-3.4 Magic Angle Sample Spinning (MAS) NMR

The primary experimental technique employed to overcome the broadening interactions in solids described in Section I-2 is Magic Angle Spinning (MAS) NMR. MAS-NMR involves rotating powdered samples in a cylinder about an axis that forms an angle of 54.7° with respect to the magnetic field H_0. This technique can eliminate the portions of second rank tensor interactions that transforms in real space as $P_2(\cos\theta) = (1-3\cos^2\theta)$, where θ is the angle between the principal axis of the tensor and the applied field. Interactions governed by this form include chemical shielding anisotropies (axially symmetric), the anisotropic portion of the indirect dipolar coupling, the direct dipolar coupling, and quadrupolar coupling with axially symmetric field gradient tensors.

An illustration of the effect of MAS is provided in Figure I-8. Figure I-8a is a simulated static CSA pattern of the ^{19}F spins in calcium fluorapatite in a 9.4 T field, and is approximately 32 kHz wide. This simulation was performed using the measured values of the principal components of the ^{19}F shielding tensor in fluorapatite and neglected the hetero- and homonuclear dipolar couplings. A simulation of a spectrum for the same spin system subjected to MAS is shown in Figure I-8b. This spectrum exhibits typical appearance, having a comb of peaks separated by the sample rotation frequency ω_r with an intensity profile that roughly mimics the intensity in the static spectrum. In a MAS spectrum there is always a peak at the isotropic chemical shift which is referred to as the centerband. The other peaks (called the sidebands) can be distinguished from the centerband since they change position in the spectrum when the spinning speed is changed. When the sample spinning speed is much greater than the breadth of the static spectrum, the sidebands become vanishingly small and only the centerband remains. The utility of MAS-NMR is easily appreciated when one considers a static spectrum
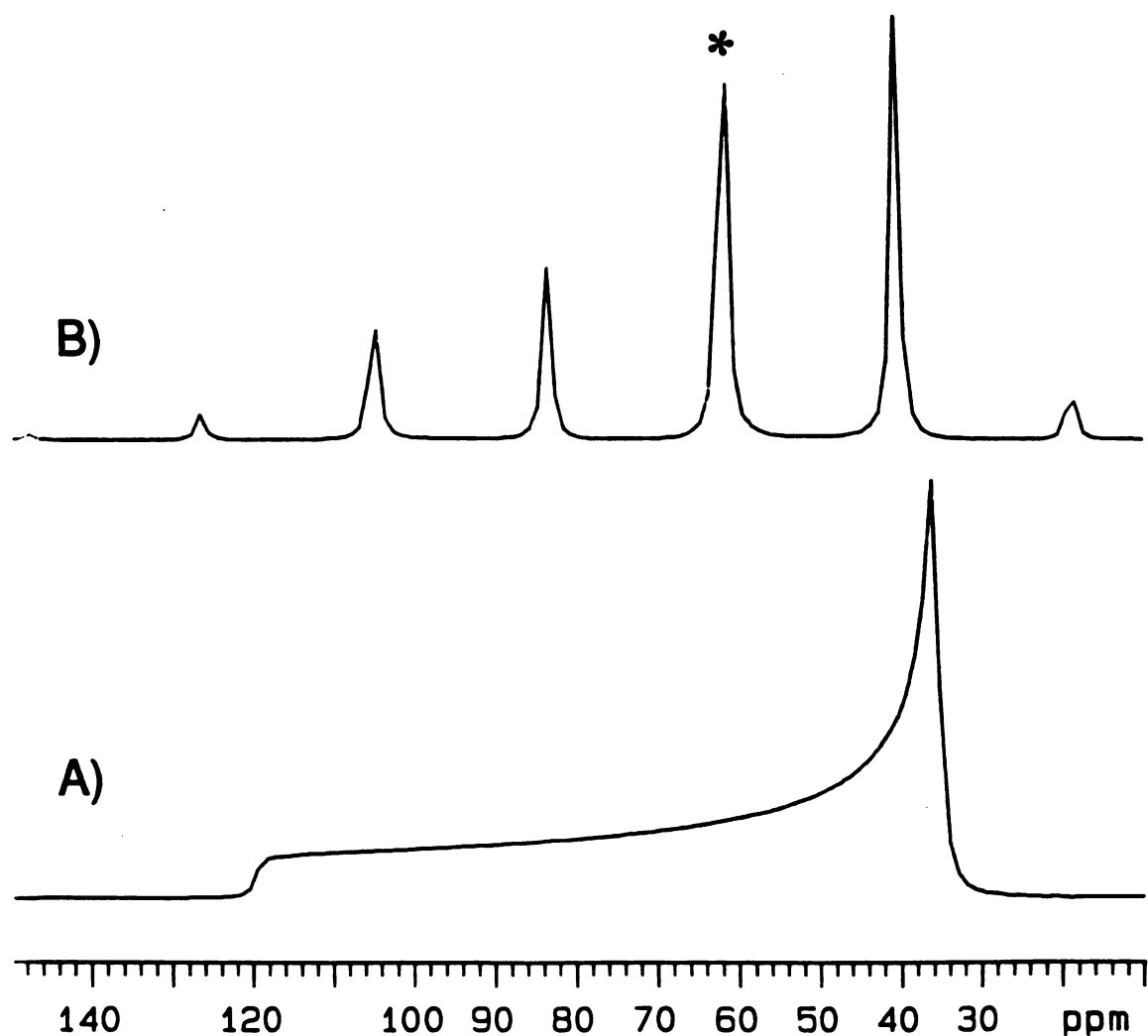
Figure I-8. Simulated chemical shielding powder pattern with an axially symmetric shielding tensor with chemical sheilding anisotropy CSA = 84 ppm, σ_{iso} = 64 ppm and an asymmetry parameter η = 0: (a) under static conditions and (b) under Magic Angle Spinning conditions with ν_r = 8.0 kHz. The centerband is marked with an asterisk. An exponential apodization function corresponding to a 400 Hz line broadening was applied to the simulated FID before Fourier transformation.

influenced by more than one chemical shielding tensor present. In such a spectrum it would in general be difficult to determine that there were two or more distinct tensors present if the difference between the isotropic chemical shifts was less than the CSA powder pattern linewidths. On the other hand, the MAS spectrum would resolve the peaks corresponding to the different isotropic shifts of the different shielding tensors. A striking example of how well MAS can resolve distinct resonances is given in Section II.

The ability of the MAS process to create well resolved peaks in the spectra of solids enables the use of selective excitation schemes to saturate or invert the magnetization of single peak. Selective excitation can be carried out by a number of different schemes typically used in solution state NMR such as a soft pulse, DANTE,[16] or SELDOM.[17] In this work (Sections II and III) DANTE[16] pulse trains are use to selectively invert or saturate peaks under MAS conditions. A DANTE pulse train is simply a series of small flip angle pulses separated by uniform time delays. The DANTE pulse train has the effect of exciting peaks on resonance with the rf. Under MAS conditions optimal selectivity is achieved by synchronizing the small flip angle pulses in the DANTE train with the rotor rotation period. In sections II and III pulse sequences which use rotor synchronized DANTE trains are discussed.

I-3.5 Spin Diffusion

This section will qualitatively explain the concept of spin diffusion and describe some experiments used to measure spin diffusion. Spin diffusion is a term used to describe the transfer of longitudinal (z) magnetization between different (spatially distinct) regions of the sample via the dipole-dipole coupling of nuclear spins. Spin diffusion has the effect of moving spin polarization from regions of high polarization to regions of low polarization. Spin polarization can be transferred in a

qualitatively similar manner by atomic or molecular diffusion; however, in solid materials where atoms are essentially locked in place, the transfer of polarization can only arise from spins diffusion processes.

The actual process that moves polarization through space is the spin flip-flop or zero-quantum transition. For homonuclear isolated spin pairs the frequency of flip-flop transitions between states (i. e. $|\alpha\beta\rangle \rightarrow |\beta\alpha\rangle$ or $|\beta\alpha\rangle \rightarrow |\alpha\beta\rangle$) can be approximated by the formula:[5]

$$\omega_1 = \frac{E_S - E_T}{h} = \frac{\gamma^2 h}{2r^3}\left(1 - 3\cos^2\theta\right). \qquad \text{I-43)}$$

This formula is only an approximation in the sense that these m-basis states are not the eigenbasis of the total Hamiltonian (Zeeman and dipolar).[5] The types of transtions expected for a pair of coupled spins are zero ($|\alpha\beta\rangle \rightarrow |\beta\alpha\rangle$) , single ($|\alpha\beta\rangle \rightarrow |\alpha\alpha\rangle$) and double $|\alpha\alpha\rangle \rightarrow |\beta\beta\rangle$ quantum transitions. However, in a large magnetic field the zero-quantum transitions shown above are almost exclusively the only type that occur; since they are the only type that conserve total Zeeman energy. It has been pointed out by Abragam[5] that the problem can be thought of as one of an rf field of amplitude $H_1 = \omega_1/\gamma$ inducing transition between two states $|\alpha\beta\rangle$ and $|\beta\alpha\rangle$.

Spectral spin diffusion refers to spin diffusion between spins with different resonant frequencies. In this case a flip-flop transition has the effect of transferring magnetization from one peak to another and can be directly monitored through the intensity of the resonances in the spectrum. Unlike the pair of like-spins mentioned above, the flip-flop associated with spectral spin diffusion does not take place spontaneously since it does not conserve total Zeeman energy. Spectral spin diffusion is enabled when there is a source of energy to compensate for the energy difference between $|\alpha\beta\rangle$ and $|\beta\alpha\rangle$. The sources of this additional energy will be

discussed in Section II, in reference to spectral spin diffusion in fluorapatite under MAS conditions.

A schematic representation of a spectral spin diffusion experiment is given in Figure I-9. The basic scheme to measure spectral spin diffusion involves saturating the magnetization of a desired resonance and observing cross relaxation (magnetization transfer) to other resonances in the spectrum. Various methods can be used to selectively saturate a line. After a mixing period, any z-magnetization is turned into transverse magnetization with a $\pi/2$ pulse for detection. Competing processes that affect the dynamics of z-magnetization of the resonances are longitudinal (T_1) relaxation and spin exchange (by atomic or molecular diffusion). Provided that the rate of magnetization recovery from longitudinal relaxation is on the order of (or slower than) the spin diffusion rate, and spin exchange is very slow compare to spin diffusion, spectral spin diffusion can be detected by a scheme pictured in Figure I-9.

The presence of rapid spin diffusion in a sample can manifest itself as equal (or nearly equal) longitudinal relaxation times T_1 of various resonances in the spectrum. Spins are relaxed by the fluctuations in local fields. When paramagnetic centers are present in a sample, the nuclei near the fluctuating magnetic dipole of an unpaired electron can be relaxed many orders of magnitude faster than they would be in a sample lacking paramagnetic spins. The consequence of this is shown schematically in Figure I-10. At first, the spins near the paramagnetic center repolarize quickly, but then polarization is carried from these highly polarized regions into the rest of the sample. If spin diffusion is rapid, the recovery rate of the magnetization of all spins in the sample will be close to that of those near the paramagnetic center. Furthermore, if there is a low level of paramagnetic centers in the material, the rate of repolarization of spins distant from the paramagnetic spins will be influenced by two processes: longitudinal relaxation and the transfer of

polarization from paramagnetic centers by spin diffusion. In this case the observed recovery of the magnetization is nonexponential. These spin diffusion effects will be considered in section II.

Figure I-9. Schematic of a spin diffusion experiment. Spectral spin diffusion between two reservoirs of spins with distinct chemical shifts (A and B) can be detected and monitored by saturating peak A by one of several methods (see text) and observing the transfer of z magnetization to peak B as a function of mix time. The z magnetization is typically obtained by placing the magnetization into the x-y plane with a non-selective read pulse.

spectral "picture"　　　　**spatial "picture"**

A　　B　　　　　　　　A　　B

T
I
M
E
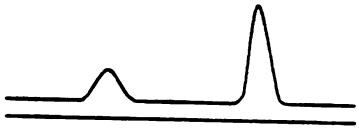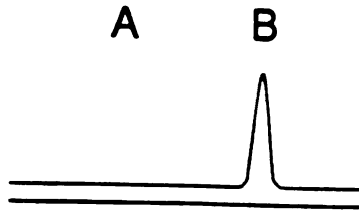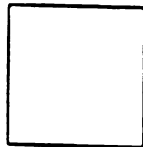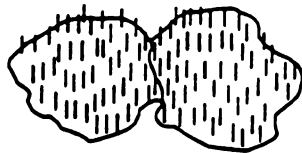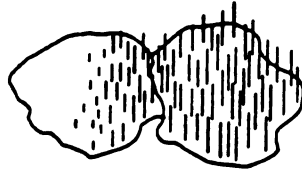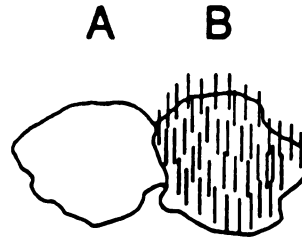
saturated　　　　　　polarized
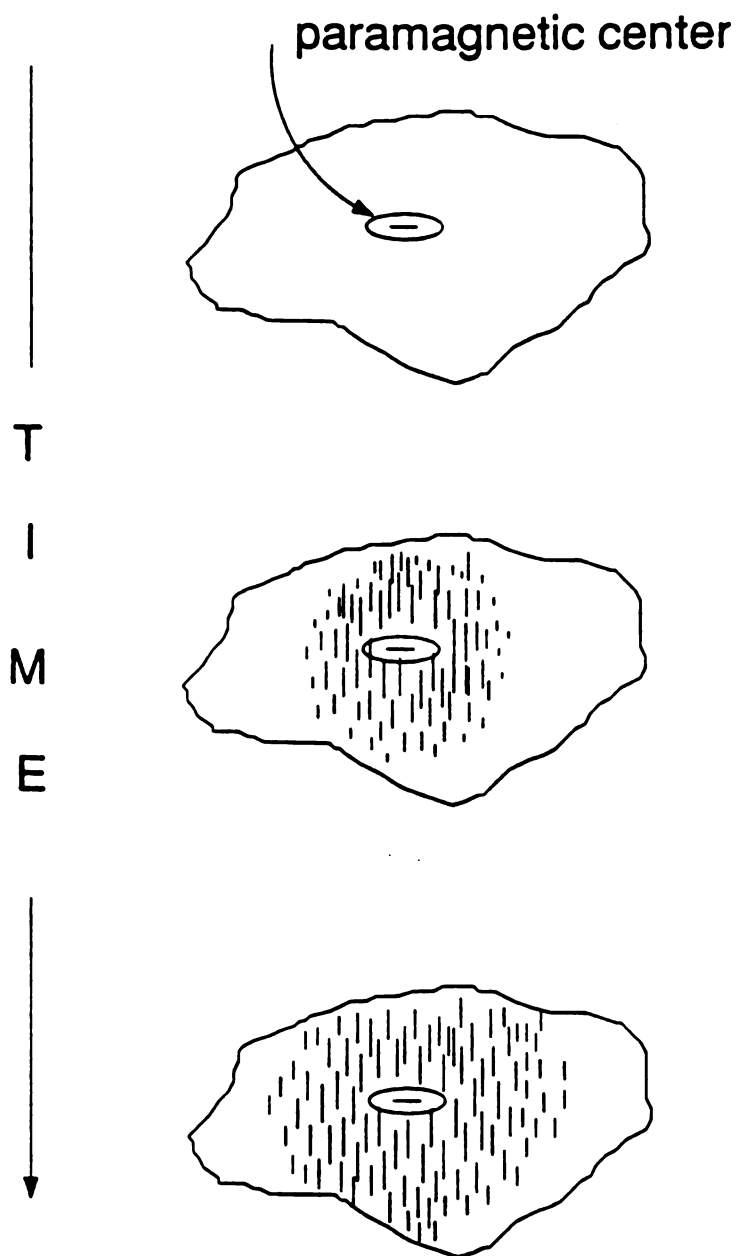
Figure I-10. Schematic diagram of polarization transfer from a paramagnetic center. The lengths of the vertical line segments indicate polarization as in Figure I-9. Spins in saturated systems near paramagnetic centers become polarized rapidly, and this polarization is transferred to the rest of the sample.

I-8 References

1. Silicon and sulfur replace two phosphorus ions as a charged coupled pair.

2. N. N. Greenwood and A. Earnshaw. Chemistry of the Elements. (Pergamon, Oxford, 1986).

3. S. Naray-Szabo. *Z. Krist.* **75**, 387 (1930)

4. W. E. Brown, M. Mathew, M. S. Tung, *Prog. Cryst. Growth Charact.* **4**, 59 (1981).

5. A. Abragam. *The Principles of Nuclear Magnetism*, (Oxford, London, 1961).

6. G. E. Pake. *J. Chem. Phys.* **16**, 327 (1948)

7. C. P. Slichter. *Principles of Magnetic Resonance*. 3 rd Edition. (Springer-Verlag, Heidelberg, 1990).

8. J. A. Sidles. *Phys. Rev. Lett.* **68**, 1124 (1992).

9. D. N. Shykind, J. Baum, S.-B. Liu, A. Pines and A. N. Garroway, J. Magn. Reson. 76 (1988) 149.

10. D. Suter, S. B. Liu, J. Baum and A. Pines. *Chemical Physics.* **114**, 103-109 (1987).

11. D. P. Weitekamp, in Advances in Magnetic Resonance, Vol. 11, ed. J. S. Waugh (Academic Press, New York, 1983) p. 111.

12. K. K. Gleason, *Conc. Magn. Reson.* **5**, 199 (1993) .

13. J. Baum, M. Munowitz, A. N. Garroway and A. Pines, *J. Chem. Phys.* **83**, 2015 (1985) .

14. S. Lacelle, in *Advances in Magnetic Resonance*, Vol. 16, ed. J. S. Waugh (Academic Press, New York, 1991) p. 173.

15. B. E. Scruggs and K. K. Gleason, *Chem. Phys.* **166**, 367 (1992) .

16. G. Bodenhausen, R. Freeman, and G. A. Morris. *J. Magn. Reson.* **23**, 171 (1976).

17. D. Boudot, D. Canet, J. Brondeau, and J. C. Boubel. *J. Magn. Reson.* **83**, 428 (1989).

Section II

^{19}F and ^{31}P MAS-NMR of Antimony(III)-doped Fluorapatite Phosphors: Dopant Sites and Spin Diffusion

1. Introduction

The apatite structure,[1] with its extensive and varied substitutional chemistry,[2] is the basis for a wide variety of inorganic solids important in biomineralization, geology, and materials science. From the materials science standpoint, one extremely important technological application of apatites is as halophosphate phosphors in fluorescent lamps. The most commonly used phosphor is based on calcium fluorapatite [$Ca_5F(PO_4)_3$]. In commercial phosphors, approximately 20% of the fluoride ions are replaced by chloride ions. Also, 0.5 - 1.0 wt. % Sb^{3+} is present as an activator to absorb UV irradiation produced by the Hg discharge present in the lamp. The antimony subsequently converts this excitation energy into visible light by either of two processes. Direct Stokes shifted emission from antimony can occur, or the excitation energy can be transferred to Mn^{2+}, present in 0.0 - 0.5 wt.% quantities, which also emits light in the visible region of the spectrum. A detailed understanding of UV absorption, energy transfer, visible emission, and defect structures that lead to photodegradation requires knowledge of the lattice substitution site of the activator ion. Whereas the substitutional sites and oxidation state for manganese have been well established, [3,4] this is not true for antimony. Moessbauer results on antimony-doped calcium fluorapatite phosphors[5] have shown that the antimony in the lattice has an oxidation state of

+3. However, identification of the substitution site in the lattice is controversial, with at least two different sites having been proposed.[5-9]

The fluorapatite structure features linear chains of crystallographically equivalent fluoride ions parallel to the c axis and extending the length of the crystal (Figure II-1).[1,2] There are two types of calcium ions in the structure, labelled Ca(1) and Ca(2), in the ratio of 4:6. Surrounding each fluoride ion is an equilateral triangle of crystallographically equivalent Ca(2) ions that lie in a plane perpendicular to the fluoride chain. Adjacent triangles are rotated by 60° about the chain axis, creating a hexagonal screw axis in the structure. Adjacent to these Ca(2) sites are crystallographically equivalent phosphate tetrahedra. Finally, there are columns of Ca(1) ions running parallel to the c axis, each calcium column in the middle of an equilateral triangular prism formed by three fluoride columns.

Previous studies have considered three different possible substitution sites for antimony in the fluorapatite lattice. The first site of antimony substitution that has been considered is the Ca (I) site;[5-7] however, no direct experimental evidence for this model has been found. A second model, based on Rietveld analysis of x-ray powder diffraction data, invokes the replacement of Ca^{2+} at the Ca(2) site with an Sb^{3+} ion;[8] however, charge compensation was not explicitly discussed. Studies based on analyses of stoichiometry as well as spectroscopic data also support the replacement of Ca^{2+} at the Ca(2) site by Sb^{3+}, accompanied by the replacement of the adjacent fluoride ion by O^{2-} to achieve charge compensation.[6,7,9] The third, most recent model, involves the substitution of phosphorus(V) in the phosphate tetrahedron by Sb^{3+}, with the loss of one oxygen atom of the tetrahedron providing charge compensation (the 5s electron lone pair of the antimony(III) atom is directed toward the missing oxygen atom site in this model). This phosphate substitution model is based on measurements from Moessbauer data as well as theoretical calculations of antimony nuclear electric quadrupole coupling constants.[5]
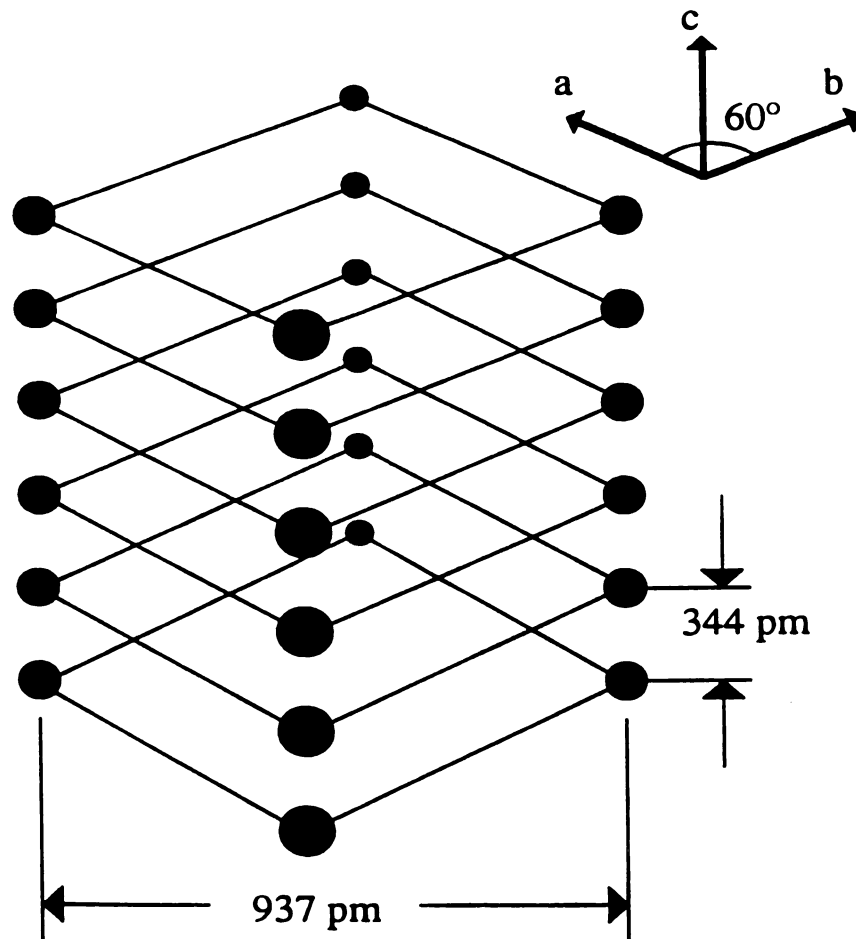
Figure II-1. Schematic diagram of the arrangement of four linear columns of fluoride ions (•) in the fluorapatite ($Ca_5F(PO_4)_3$) lattice.

The determination of which of these conflicting proposals is correct, and whether there is exclusively one dopant substitution site, requires a technique sensitive to local environments. High-resolution solid-state NMR, using the technique of magic-angle spinning (MAS),[10] is widely used to determine local structure, but has rarely been applied to the study of dopants. The major difficulty in studying dopant atoms at low concentrations in solids is limited sensitivity. Most spin 1/2 nuclei have relatively low magnetogyric ratios and/or low natural abundances, and quadrupolar nuclei (I>1/2) usually exhibit excessive NMR spectral line broadening. However, both ^{19}F, ^{31}P, and ^1H nuclei have natural abundances of 100 and large magnetogyric ratios, making them good prospects for studying dopants (the high-resolution ^{31}P and ^{19}F MAS-NMR spectra of undoped fluorapatite have already been reported[11-13]). The large chemical shift range of ^{19}F (several hundred ppm in metal fluorides[14]) makes it a particularly attractive probe nucleus. However, strong homonuclear dipolar couplings can make it difficult to obtain high resolution MAS-NMR spectra, particularly for ^{19}F and ^1H, unless more involved multiple-pulse techniques are used.[13,15] Fortunately, the availability of MAS rotor designs having high maximum spinning speeds, combined with the selection of samples having special structural arrangements, has made it possible to obtain high-resolution ^1H and ^{19}F MAS-NMR spectra in a variety of interesting systems. The special structural arrangements of homonuclear spins required include relatively isolated spin pairs,[16,17] dilute spins, and linear chains of spins.[18] The latter arrangement is characteristic of the fluorine atoms in fluorapatite, and high-resolution ^{19}F MAS-NMR spectra have been reported for calcium fluorapatite and fluorohydroxyapatites.[12]

The use of MAS-NMR to probe local structure has generally involved the measurement and interpretation of isotropic chemical shifts and possibly chemical shift anisotropies. Special techniques to measure heteronuclear dipolar couplings

have also proven useful.[19-21] Homonuclear dipolar couplings of abundant spins in MAS-NMR spectra manifest themselves in (at least) two ways: as "dipolar sidebands" in the spectra,[16,17] and as the source of "spin diffusion" contact among spins. Despite the great potential for obtaining local structural information from such spin diffusion measurements, since the dipolar coupling is inversely related to the cube of the internuclear distance, few applications have been reported.[22-25] In this study, we demonstrate that in an abundant homonuclear dipolar system spectral spin diffusion between peaks with different isotropic chemical shifts can be observed using a one-dimensional (1-D) MAS-NMR experiment referred to as selective population anti-z and rate of tranfer to adjacent nuclei (SPARTAN).[26] A rotor-synchronized DANTE pulse train is used to selectively invert the magnetization of a ^{19}F peak and its associated sidebands, and all peaks are nonselectively observed after a mixing period during which spin diffusion occurs. The change in intensity of a peak resulting from cross-relaxation to other peaks as a function of the mixing time provides a quantitative measure of spin diffusion and can aid in assignment of peaks.

In this study, we report quantitative ^{19}F and ^{31}P MAS-NMR results for calcium fluorapatite samples containing 0.0 to 3.0 total wt. Sb^{3+} as well as ^{31}P MAS-NMR results for the model compounds $SbPO_4$, $Sr_{1.03}Ca_{8.97}F_2(PO_4)_6$, $Sr_5F(PO_4)_3$ and $Ba_5F(PO_4)_3$. The ^{19}F and ^{31}P MAS-NMR results, including the ^{19}F MAS-NMR spin diffusion experiments, will be discussed in relation to three possible models for substitution of antimony into the fluorapatite lattice. We will show that only the phosphate substitution site (the third model) is consistent with the totality of experimental results.

2. Experimental

2.1. Sample preparation and characterization

The samples of antimony-doped fluorapatite that were prepared contained 0.00, 0.18, 1.3, 1.7, 2.1, and 3.0 wt.% antimony(III) (determined by permanganate titration). Samples containing 0.00, 1.7, and 3.0 wt.% antimony were prepared by combining $Ca_2P_2O_7$, CaO, CaF_2, and $CaSb_2O_6$ (GTE Chemical and Metals Division, Towanda PA) and firing in a covered Coors porcelain crucible at 1200°C. Both the 1.7 and 3.0 wt. % antimony samples were firings of identical raw material blends. The difference in the final antimony levels in these two samples arises from significant vapor transport taking place during firing as described in reference 8. Because of this vapor transport process, it is difficult to control the final antimony level in a given sample. The samples containing 1.3 and 2.1 wt. % antimony were prepared from identical raw material blends, but in a different manner than the samples containing 1.7 and 3.0 wt.% antimony. The reagents $CaHPO_4$, $CaCO_3$, and CaF_2 (GTE Chemical and Metals Division, Towanda PA) were first fired in stagnant air to create a fluorohydroxyapatite (with an indication of some carbonate substitution for phosphate from IR spectroscopy). $CaSb_2O_6$ and a small amount of $Ca_2P_2O_7$ were then fired with the precursor at 1200°C in a covered Coors porcelain boat. The 0.18 wt.% sample was prepared by firing a combination of $Ca_2P_2O_7$, CaO, CaF_2, and Sb_2O_3 at 1100°C in an open quartz boat with a flowing nitrogen atmosphere. Finally, the 0.8 wt % sample was a commercial halophosphate phosphor (GTE type 2440)

The specific surface areas of the samples containing 0.0 wt.% and 2.1 wt. antimony were measured with a Quantachrome Monosorb Brunauer-Emmett-Teller (BET) apparatus and were determined to be 0.626 ± 0.007 and 0.506 ± 0.004 m^2/g respectively.

The $SbPO_4$ sample was obtained from GTE Chemical and Metals Division, Towanda PA, and was annealed in air at 600° C for 1/2 hour to improve its crystallinity. Its identity was confirmed by using X-ray powder diffraction (two small peaks attributable to Sb_2O_4, cervantite, were also present).

The $Sr_{1.03}Ca_{8.97}F_2(PO_4)_6$ was prepared by combining the following starting materials in the molar ratio: 6.0 moles $CaHPO_4$, 2.982 moles $CaCO_3$, 0.994 moles SrF_2, and firing for 2 hours at $1150^\circ C$ under nitrogen in a Crystar crucible.

2.2 NMR equipment and procedures

The ^{31}P and ^{19}F MAS-NMR spectra were recorded on a 9.4T Varian Associates VXR-400 spectrometer at the Max T. Rogers NMR Facility at Michigan State University, operating at frequencies of 161.76 MHz, and 376.2 MHz respectively. The fluorine radiofrequency was amplified by an AMT model 3137/3900-2 amplifier. The phosphorus radiofrequency was amplified by an Amplifier Research model 1000LPM10 amplifier. A fast switching PIN diode was used to isolate the receiver during the pulse, and 1.0 μs after the end of the pulse. The ^{19}F spectra were collected by using an ultra-high speed ^{19}F MAS-NMR probe from Doty Scientific (Columbia, SC) with 5 mm o.d. Si_3N_4 rotors with Vespel caps. The probe was equipped with a fiber optic detector to measure both the speed and the position of the rotor for the rotor-synchronized spin diffusion experiments. The 5 mm rotors contained approximately 160 mg of sample, and spinning speeds υ_r were typically 8.25 ± 0.1 kHz. The $\pi/2$ pulses for ^{19}F were 4.0-4.2 μs. The magic angle of the ^{19}F MAS-NMR probe was set by minimizing the linewidth of the fluorapatite peak. Chemical shift referencing of the ^{19}F MAS-NMR spectra was accomplished by using fluorapatite prepared as in ref. 12 as a secondary chemical shift reference at 64.0 ppm (downfield) with respect to hexafluorobenzene at 0.0

ppm.[12] The ^{19}F MAS-NMR spectra were obtained with a 100kHz sweep width, using 32,000 data points. An exponential weighting corresponding to a line broadening of 37 Hz (0.1 ppm) was applied to the FID before Fourier transformation. Eight transients were collected for each Bloch decay ^{19}F MAS-NMR spectrum with relaxation delays of at least five times the spin lattice relaxation time T_1.

The ^{31}P MAS-NMR spectra were obtained by using a high speed multinuclear MAS-NMR probe from Doty Scientific (Columbia, SC) with 7 mm o.d. Si_3N_4 rotors with Vespel caps. The rotors contained approximately 500 mg of sample. The probe was equipped with a fiber optic detector to measure the spinning speed of the rotor. Spinning speeds v_r for the ^{31}P MAS-NMR experiments were 6.15 ± 0.1 kHz and the $\pi/2$ pulses were 6 μs. The magic angle was set by observing the ^{79}Br resonance in KBr. The chemical shifts of the ^{31}P MAS-NMR spectra were referenced to the peak of fluorapatite at 2.8 ppm downfield (with respect to 85 % H_3PO_4).[11] The ^{31}P MAS spectra were obtained with a 30kHz sweep width, using 48,000 data points. An exponential apodization was applied to the FID corresponding to a line broadening of 100 Hz.

The ^{31}P MAS-NMR spectra were obtained by collecting 80 transients using $\pi/4$ (3 μs) pulses and a delay time of 180 s between scans. Since ^{31}P MAS-NMR spin lattice relaxation times can be extremely long in rigid solids (hours), the spectrum of the 2.1 wt. % Sb^{3+} fluorapatite sample was also obtained with a very long relaxation delay of 3600 s and eight transients; no additional peaks due to a slowly-relaxing component could be detected.

Values of the ^{19}F spin lattice relaxation time T_1 were obtained with an inversion recovery pulse sequence with four transients for each value of the delay time, and a relaxation delay at least 5 times the T_1 of each sample. Thirteen delay time values were used for each T_1 experiment. The T_1 values of the centerbands

and sidebands (equal within experimental error for a given sideband family) were calculated by using peak heights and the VNMR 2.2 software. Values of the ^{19}F transverse relaxation times, T_2, were obtained by using a rotor synchronized Hahn spin echo experiment with four transients for each value of the delay. The value of T_2 was obtained by fitting the peak heights to an exponential using Varian VNMR 2.2 software. This sequence comprises a $(\pi/2)_x$ pulse, a delay, a $(\pi)_x$ pulse applied at the same rotor orientation ($\pm 0.5°$) as the $(\pi/2)_x$ pulse, and a further delay before acquisition. Synchronization was necessary to ensure that the second pulse comes at the maximum of a rotational echo.[18]

^{19}F MAS-NMR spectral spin diffusion was measured by selective inversion of a specific resonance and its associated sidebands, followed by a cross-relaxation delay and then a nonselective $\pi/2$ pulse to monitor the longitudinal magnetization (Figure II-2). Selective inversion of the centerband and sidebands was achieved by a DANTE pulse train[27] that consisted of fifteen 12 (1.6 μs) pulses applied once each rotor period at identical rotor orientations (to within $\pm 0.5°$). These pulse lengths (and the corresponding power levels) were chosen to give an optimal excitation profile for the peaks in the spectra. The nonselective $\pi/2$ observation pulse was 12 μs, and its phase was alternated to cancel out the effects of DANTE pulse trains that did not fully invert the magnetization of a specific resonance.[28] The cross-relaxation mixing period was varied from 1 ms to 12 sec, with 8 transients collected for each mixing time.

Deconvolution of overlapping ^{19}F MAS-NMR peaks was performed with the standard deconvolution tools in VNMR 2.2, the software package on the Varian VXR-400 spectrometer. This program operates by fitting the spectrum to a set of user selected Lorentzian peaks by varying the line widths, chemical shifts, and peak intensities.
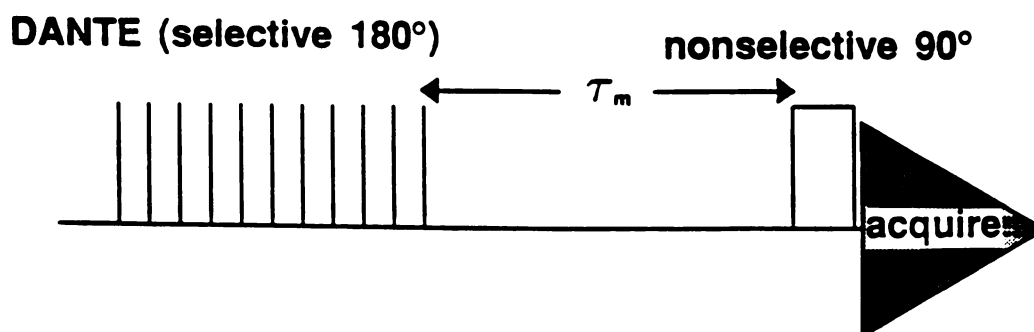
Figure II-2. SPARTAN pulse sequence for measuring spectral spin diffusion (see text).

3. Results

3.1 ^{31}P MAS-NMR

The ^{31}P MAS-NMR spectrum of fluorapatite is shown in Figure II-3a. It contains a peak at the isotropic chemical shift of 2.8 ppm with a half-height linewidth of 0.4 ppm and small sidebands arising from a small chemical shift anisotropy.[11] The spectrum of fluorapatite containing 2.1 wt. % antimony is shown in Figure 3b. There are no additional peaks observed in the spectrum of antimony doped fluorapatite with enough intensity to be attributable to the presence of antimony (i.e. if each antimony ion perturbed five phosphorus atoms, e.g. by occupying a calcium site, the corresponding perturbed ^{31}P peak would have 15.1% of the total spectral intensity). The small peaks shown in the expansion of Figure II-2b at approximately 9 ppm can be attributed to a very minor pyrophosphate impurity phase. The ^{31}P MAS-NMR spectrum of antimony phosphate ($SbPO_4$) is shown in Figure II-3c. A rather broad peak ($\Delta v1/2 = 4.0$ppm) with an isotropic chemical shift of -18.3ppm and weak sidebands is seen.

To test the effect of substituting different group II metal ions in the Ca sites, ^{31}P MAS-NMR spectra of $Sr_{1.03}Ca_{8.97}F_2(PO_4)_6$, $Sr_5F(PO_4)_3$, and $Ba_5F(PO_4)_3$ were obtained. The spectrum of $Sr_{1.03}Ca_{8.97}F_2(PO_4)_6$ contains a peak with an isotropic chemical shift of 3.3 ppm, with an upfield shoulder at 2.4 ppm. The spectrum of $Sr_5F(PO_4)_3$ contains a peak with an isotropic chemical shift of 3.3 ppm. The spectrum of $Ba_5F(PO_4)_3$ contains a major peak at 1.4 ppm and two weaker peaks, the first at 2.3 ppm with one twelfth the intensity of the main, and the second (a weak shoulder) at 0.5 ppm, both presumably arising from impurities.
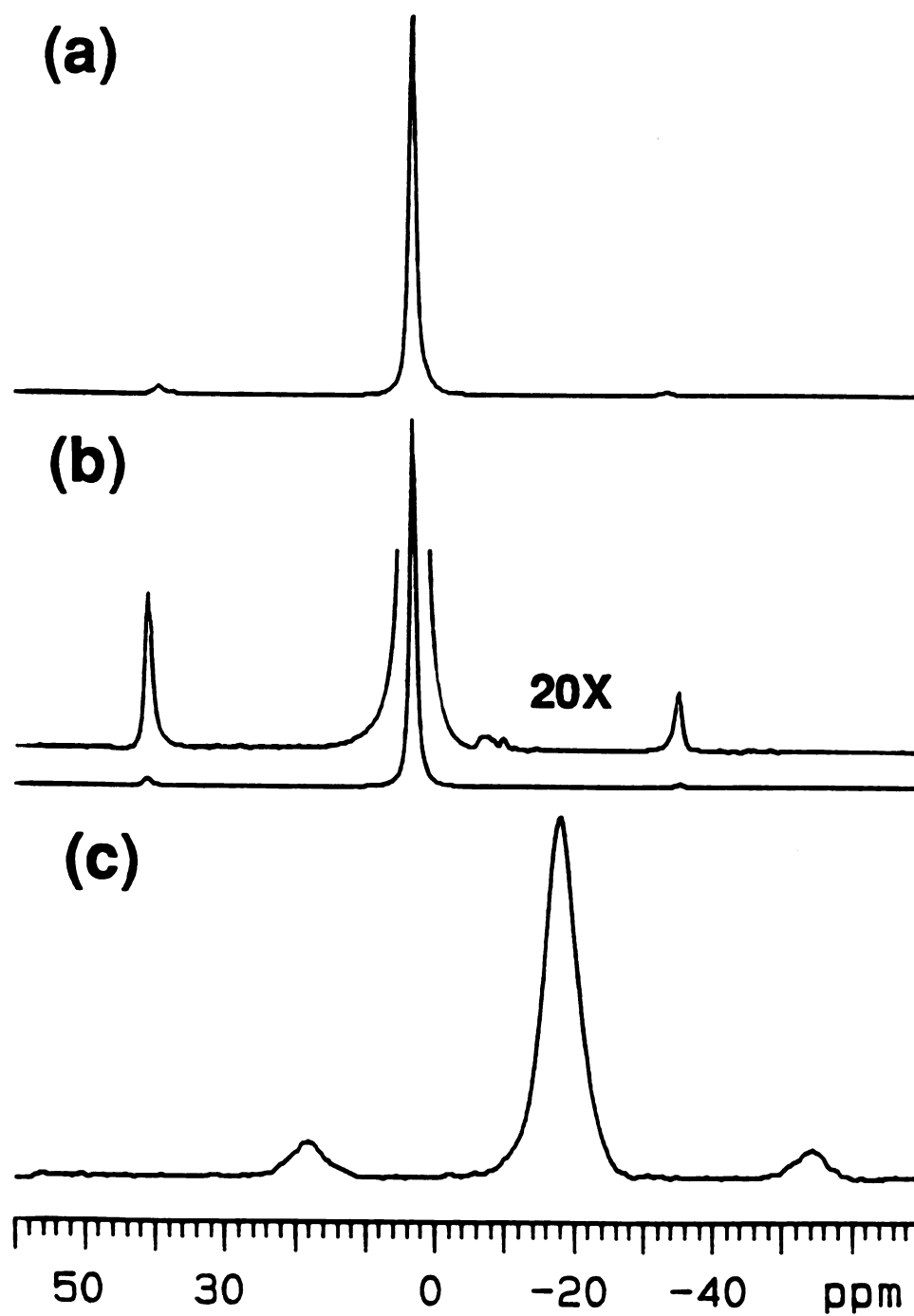
Figure II-3. ^{31}P MAS-NMR spectra with v_r= 6.15 ± 0.1 kHz; A. pure fluorapatite; B. fluorapatite containing 2.1 wt.% antimony(III) dopant, 20x vertical expansion above; C. SbPO$_4$.

3.2 ^{19}F MAS-NMR

The[19]F MAS-NMR spectrum of fluorapatite is shown in Figure II-4a. The isotropic chemical shift is 64.2 ppm and the $\Delta v_{1/2}$ value is 0.5 ppm. The sidebands of fluorapatite in the ^{19}F MAS-NMR spectrum arise principally from the axially symmetric chemical shift tensor (the anisotropy has been reported as 84 and 85 ppm[29,30]), although the [19]F-^{19}F dipolar couplings[31] and to a lesser extent [19]F-^{31}P dipolar couplings also contribute. The ^{19}F MAS-NMR spectrum of fluorapatite with 2.1 wt.% antimony is shown in Figure II-4b. This spectrum contains an intense resonance at 64.2 ppm and its associated sidebands, similar to those of fluorapatite, as well as three new peaks at 73.1 ppm, 68.6 ppm, and 65.6 ppm. The 65.6 ppm peak is a shoulder of the main peak at 64.2 ppm but is resolved by difference spectroscopy, as discussed below. Since peaks at (or near) 68.6 and 65.6 ppm are observed in the spectra of *all* of the samples containing antimony, we will refer to them throughout this paper as peaks A and B respectively. Due to its overlap with peak C, the chemical shift of peak B is less accurately determined than those of peaks A and C. The large main peak at (or near) 64.0 ppm will be referred to as peak C. The weak, broad peak at 73.1 ppm is present only in the ^{19}F MAS-NMR spectra of the samples containing 1.3, 1.7, and 2.1 wt.% antimony. All of the spectra of fluorapatite containing antimony have a very small upfield shoulder on peak C. Deconvolution indicates that the intensity of this shoulder is less than one-hundredth the intensity of peaks A and B, implying that this peak does not arise from the same source as peaks A and B. Since the shoulder is so weak, we will not discuss it further. The chemical shifts, linewidths, spin lattice relaxation times (T_1), and intensities (as a percentage of the total intensity) obtained from deconvolution of the peaks in each of the ^{19}F MAS-NMR spectra are given in Table II-1.
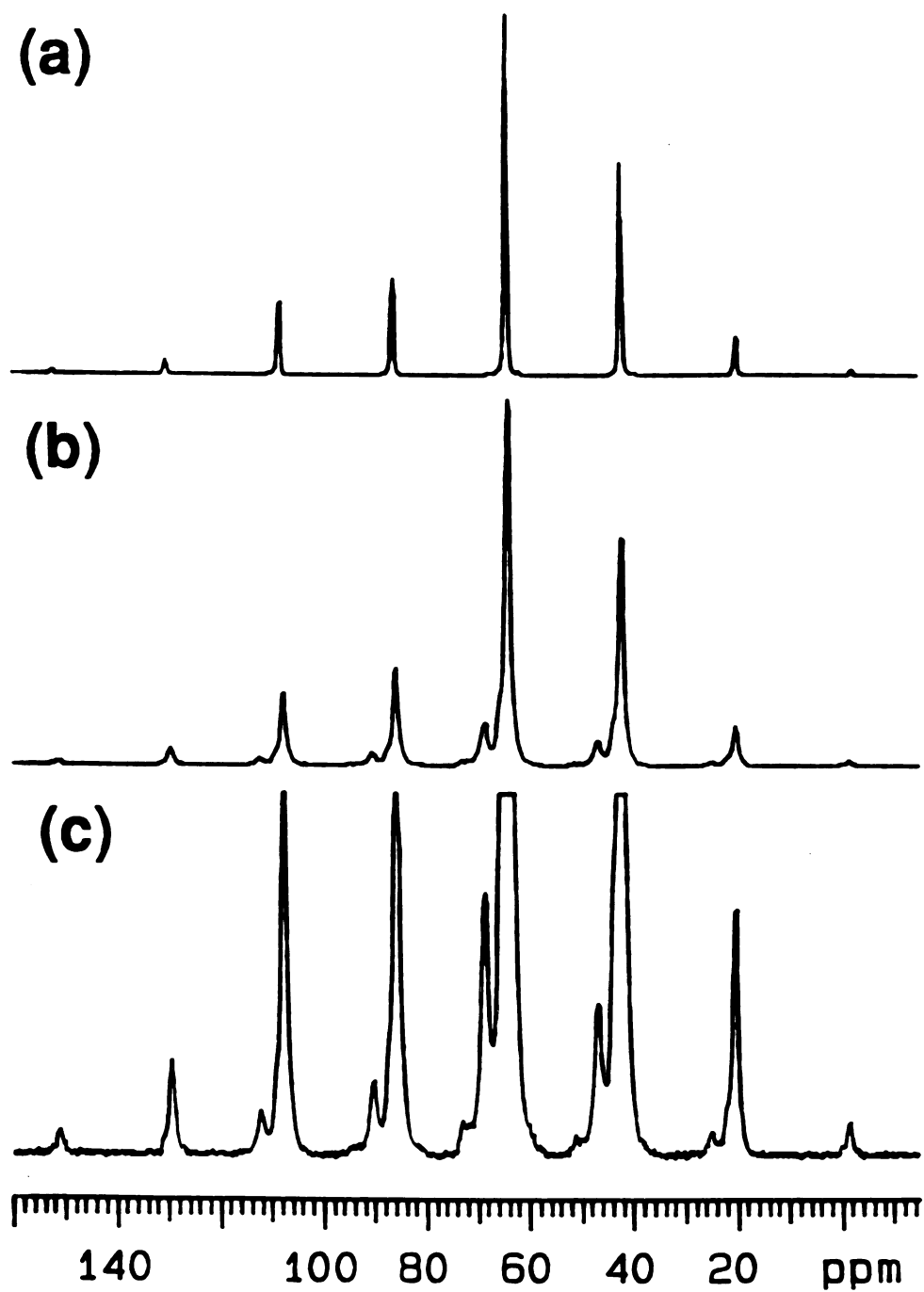
Figure II-4. ^{19}F MAS-NMR spectra with ν_r = 8.25 ± 0.1 kHz: A. fluorapatite; B. fluorapatite containing 2.1 wt.% antimony(III); C. vertical expansion of spectrum in B.

Table II-1. ^{19}F MAS-NMR data for antimony(III)-doped fluorapatite samples.

Wt. % Antimony (III)	HHLW peak C (Hz)	T₁ Peak A (s)	T₁ Peak C (s)	Peak at ca. 73 ppm (chem. shift, HHLW, area)[a]	Peak A (chem. shift, HHLW, area)[a]	Peak B (chem. shift, HHLW, area)[a]	Peak C (chem. shift, HHLW, area)[a]
0.0	189	—	84±2	—	—	—	64.2, 188, (100)
0.18	182	278±53	228±12	—	68.8, 180, 1.1	65.8, -, 0.08	64.2, 155, 98.7
0.8	246	132±11	123±4	—	68.2, 361, 6.6	65.3, 182, 2.0	63.6, 254, 91.4
1.3	296	378± 10	369± 8	72.6, 416, 0.5	68.2, 467, 8.8	68.2, 283, 4.3	63.5, 341, 86.3
1.7	296	193±7	175±8	72.6, 2285, 4.7	68.2, 380, 7.6	65.2, 239, 4.1	63.6, 282, 83.2
2.1	379	222± 12	183± 13	73.1, 1092, 3.2	68.6, 633, 13.6	65.6, 490, 10.1	64.0, 387, 73.1
3.0	239	247±33	218±13	—	68.8, 329, 5.0	65.8, 94, 0.9	64.2, 248, 94.2

a (ppm [w.r.t. hexafluorobenzene], Hz, percentage of total)

It has been demonstrated[32] that random molecular (or atomic motions) can interfere with coherent NMR line narrowing techniques such as MAS, resulting in broadening of lines if the MAS rotor period is comparable to the molecular correlation time. In order to demonstrate that random atomic motion is not broadening any of the peaks in the ^{19}F MAS-NMR spectrum to the point where they are undetectable, the spectrum of fluorapatite containing 1.7 wt. % antimony was obtained at 223 K. Since there is no difference between the spectrum obtained at 223 K and the one obtained at 295 K, random atomic motions do not appear to be interfering with the MAS process and producing broadened peaks.

In order to obtain more accurate chemical shift, linewidth, and intensity measurements of the shoulder corresponding to peak B in the spectra of doped fluorapatite, difference spectroscopy was used for all samples. Figure II-5 is a ^{19}F MAS-NMR difference spectrum obtained from the spectrum of fluorapatite containing 2.1 wt.% antimony and the spectrum of pure fluorapatite. Because the chemical shift of peak C in the doped sample is 0.2 ppm upfield of the chemical shift of fluorapatite, the difference spectrum was obtained by varying the frequency offset, linewidth (exponential apodization), and intensity (scaling factor) of the pure fluorapatite spectrum to provide the best null of the centerband of peak C. The amount of applied line broadening (apodization) required to make the linewidth of the centerband in the fluorapatite spectrum equal to the linewidth of peak C in each spectrum of fluorapatite containing antimony increased monotonically with the amount of antimony incorporated into the lattice. This suggests that the presence of antimony in the lattice slightly perturbs the apatitic fluoride ions which give rise to peak C, resulting in a symmetrical linebroadening (the specific surface areas of the 0.0 and 2.1 wt.% Sb samples are similar, arguing against crystal size effects being responsible). The additional linebroadening applied to the fluorapatite spectrum to achieve nulling of peak C in the difference spectrum does not result in a significant

reduction of the intensity of peak B in the difference spectrum since the applied broadening is small (between 0.1 and 0.8 ppm) compared to the chemical shift difference between peaks B and C (1.6 ppm). The difference spectrum clearly shows distinct peaks for A and B. The ratio of the intensity of peak A to peak B, determined by integration, equals 2:1 to within 16% uncertainty for all samples (except for the 0.18 wt. % sample). The deviation of this ratio from 2:1 becomes less with increased dopant levels, presumably because the correspondingly greater intensity of peaks A and B results in less uncertainty in their integrated areas.

The relative intensities of the sidebands of peak C in the ^{19}F MAS-NMR spectra of the samples of fluorapatite containing antimony are similar to those in the spectrum of fluorapatite, but the intensity of the third left sideband of peak C (in the sample containing 2.1 wt.% antimony) is only 70 % of that of the corresponding sideband in pure fluorapatite.

The vertically expanded centerband regions of the ^{19}F MAS-NMR spectra of each of the antimony doped fluorapatite samples as well as that of the undoped sample are shown in Figure II-6. The heights (off scale) of peak C for each of these spectra were set equal. The intensity of the peaks A and B associated with the presence of antimony in the sample do not monotonically increase with wt. % of *total* antimony, since not all of the antimony is present in the site responsible for these peaks (see below).
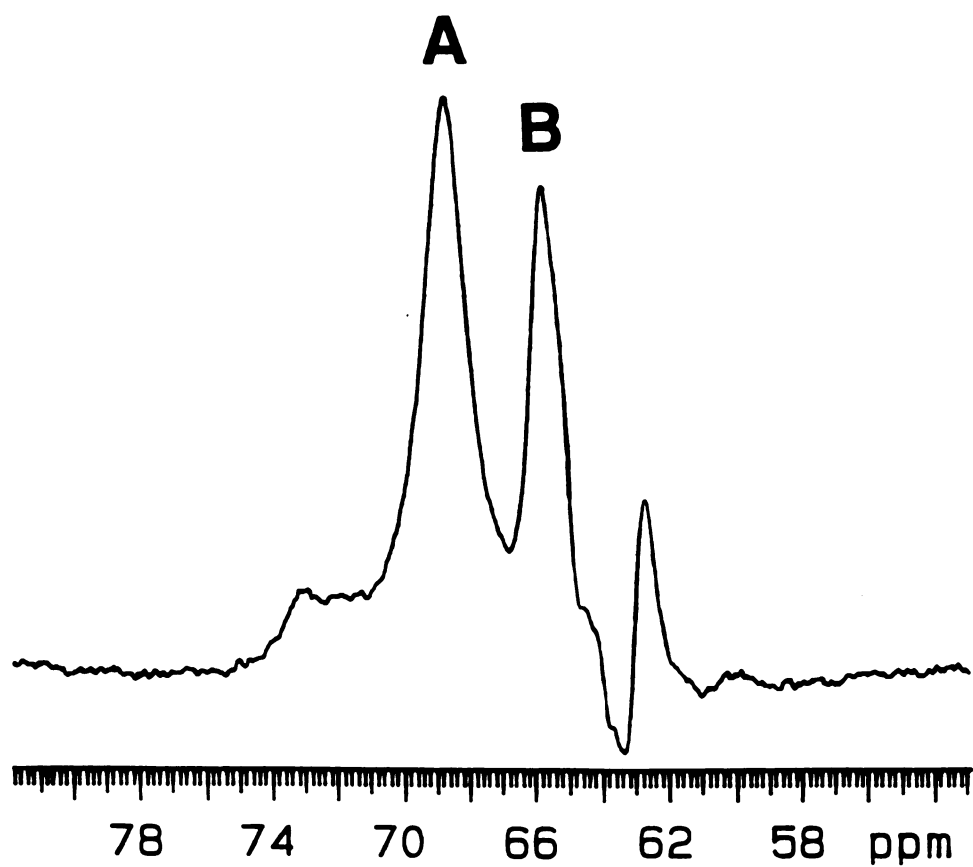
Figure II-5. ^{19}F MAS-NMR difference spectrum of fluorapatite containing 2.1 wt.%
antimony(III) and undoped fluorapatite (see text).

wt.% Sb(III)

3.0

2.1

1.7

1.3

0.8

0.18

0.0

76 72 68 64 60 56 ppm
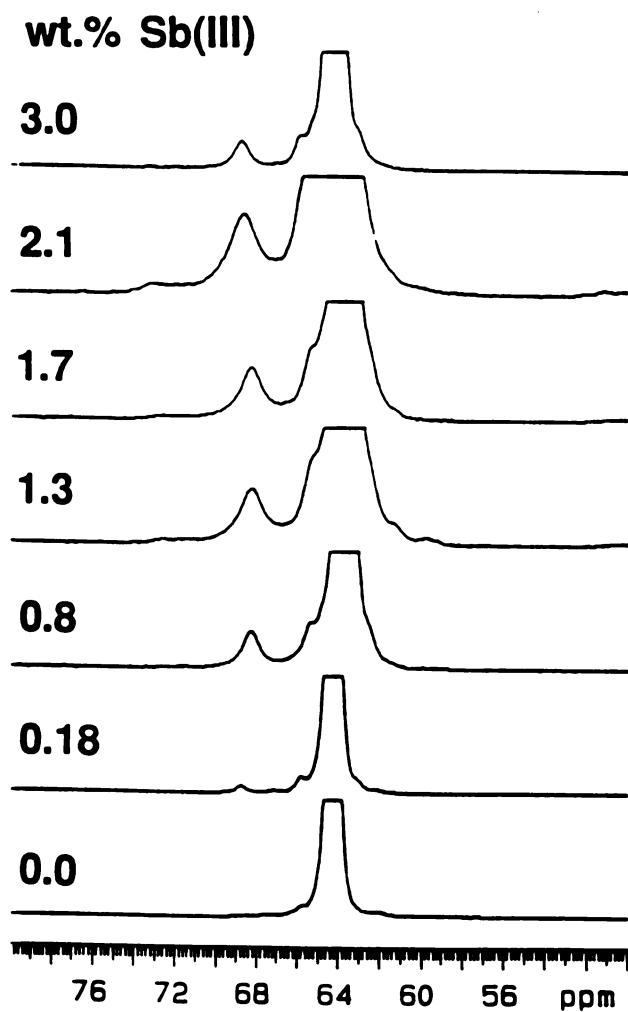
Figure II-6. ^{19}F MAS-NMR spectra (centerband region only) of antimony(III)-doped fluorapatite samples, v_r = 8.25 ± 0.1 kHz, wt.% antimony as indicated. The height of the main apatite peak (off scale) is equal for all spectra.

The T_1 values for peak C given in Table II-1 are the average of the (nearly identical) T_1 values for the centerband and the first right and first left sideband. The T_1 values for peak A are simply the T_1 values of the centerband. The T_1 values given in Table 1 for peaks A and C vary by no more than 9% for a given sample. The T_1 values of peak B for the various samples are not reported, since this peak severely overlaps peak C. Furthermore, the T_1 values of the 73.1 ppm peak are not reported since the intensity of this peak is too small. Nevertheless, the T_1 values of peak B and the 73.1 ppm peak are very close to that of peak C in a given sample, since their intensities follow the intensity of the main peak C for various delay times in the inversion recovery experiments. The spin lattice relaxation times of peaks A, B, C, and the peak at 73.1 ppm are equal to within experimental error for each sample; however, they vary irregularly from 129 s to 378 s, with no perceptible relationship to the antimony content.

The measured ^{19}F MAS-NMR transverse relaxation times (T_2) of peak C in the samples containing 2.1 and 1.7 wt. % Sb are 32 ms and 40 ms respectively. A T_2 value of 32 ms would contribute 10 Hz (0.027 ppm) to the linewidth of peak C for the sample containing 2.1 wt.% antimony, and 8 Hz (0.021 ppm) for the sample containing 1.7 wt. % antimony. The external magnetic field was shimmed by minimizing the proton line width of water in a spinning MAS rotor, yielding an estimated contribution to the half-height linewidth from field inhomogeneity of about 20 Hz (0.053 ppm). The observed half-height linewidths of the samples are considerably greater than the sum of the homogeneous broadening and the contribution from field inhomogeneity (ca. 0.1 ppm); they vary from 0.5 to 1.0 ppm (Table II-1). These half-height linewidths are significantly smaller than those previously reported for fluorapatite,[12,33] possibly because the fluorapatite in the earlier study was synthesized by an aqueous precipitation method.

Figure II-7 shows the ^{19}F MAS-NMR spectra of fluorapatite containing 1.7 wt. % antimony obtained with the SPARTAN pulse sequence. The frequency selectivity of the DANTE train was adjusted so that peak A would be inverted and the other peaks would remain unperturbed. The negative longitudinal magnetization of the inverted peak A comes to quasi-equilibrium with the relatively large bath of positive magnetization in the main apatite peak C in approximately 12 s (a time much less than the measured spin-lattice relaxation time of 193 s). While the height of the main peak decreases noticeably, the height of peak B remains constant. The total integral of the centerband region containing peaks A, B, and C should remain constant if spin diffusion is the only process affecting peaks A, B, and C. Measurements of the integral of this region show a 1.5 % increase from short to long mixing times, which is the amount expected from spin-lattice relaxation. To obtain the spin diffusion time constant from the spectra in Figure II-7, we have adapted the analysis in reference 34 for the present experiment. Although the data could be treated by simply fitting the magnetizations of peaks A and C to simple exponential curves, our analysis incorporates both data sets into one plot. The spin diffusion time constant is obtained by plotting $\ln(rf + f)/r$ vs. t_m (mixing time). The f in this relationship is given by the equation

$$f = \frac{M_a(\tau_m = \infty) - M_a(\tau_m = 0)}{M_a(\tau_m = \infty)},$$ II-1

where $M_A(\tau_m = \infty)$ and $M_A(\tau_m = 0)$ are the intensities of peak A obtained from an exponential fit. In this relationship r is given by the equation

$$r = \frac{M_A(\tau_m)}{M_C(\tau_m) - M_C(\tau_m = 0)},$$ II-2

where $M_A(\tau_m)$ is the integrated intensity of peak A, $M_C(\tau_m)$ is the integrated intensity of peak C, and $M_C(\tau_m = \infty)$ is the intensity of peak C at infinite mixing time
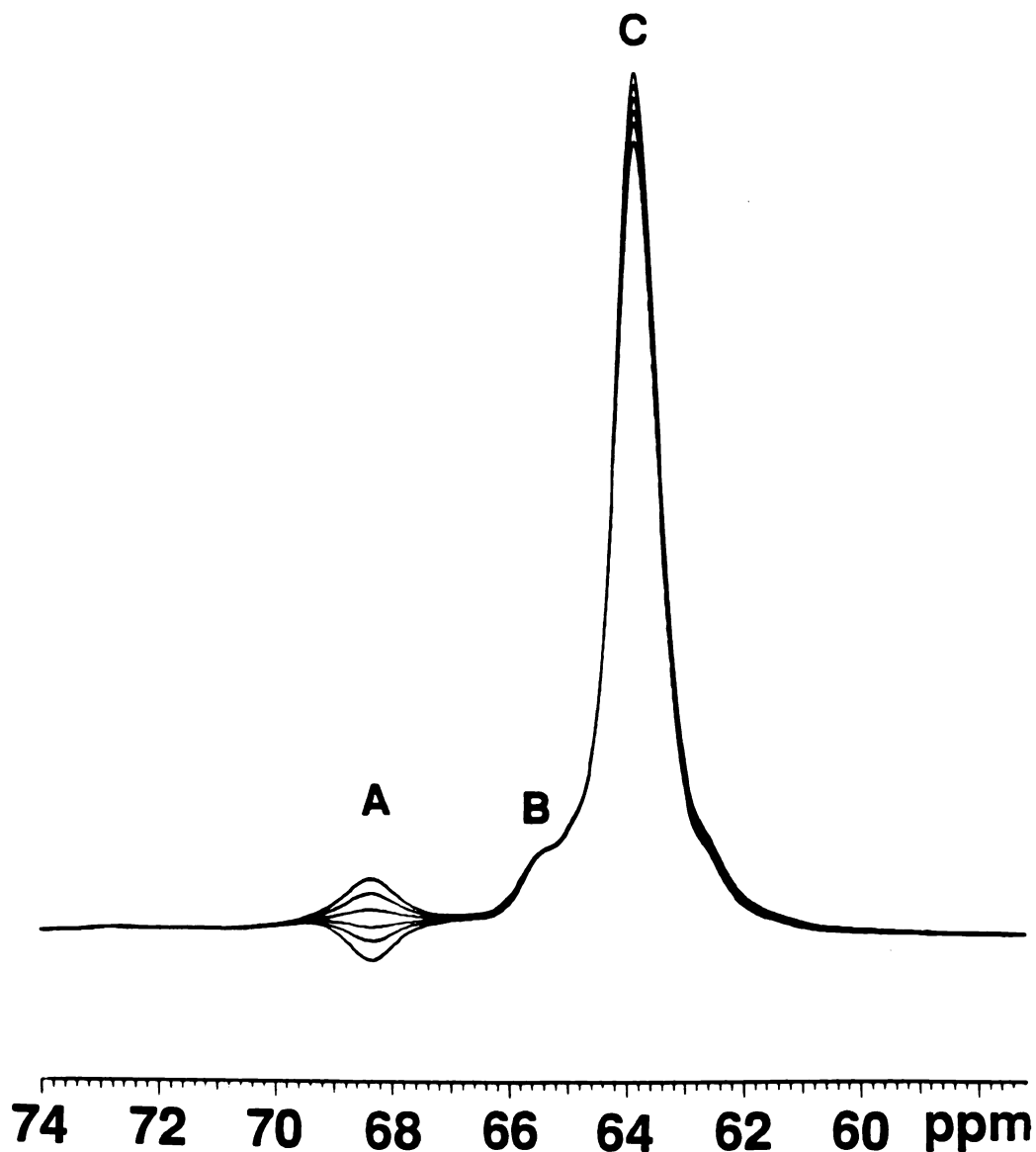
Figure II-7. ^{19}F MAS-NMR spectra (centerband region only) obtained using the SPARTAN pulse sequence (Fig. II-2 and text) of fluorapatite containing 1.7 wt. % antimony(III). Spectra for cross-relaxation mixing periods of 0.1, 0.5, 1, 2, 4, and 12 seconds are superimposed. Peak A (at 68.6 ppm) is inverted at short mixing periods, and peak C (at 64.0 ppm) steadily decreases in intensity for longer mixing periods.

obtained from an exponential fit. Contributions to $M_C(\tau_m)$ and $M_A(\tau_m)$ from the much slower longitudinal relaxation process can be safely neglected. The plot, shown in Figure II-8, should be linear for a process governed by a single spin diffusion rate, with the slope of the line equal to the reciprocal of the spin diffusion time constant, $1/\tau_{SD}$. The slopes of the plots were determined by fitting the data to a line, weighting points inversely proportional to their variances squared. The values of τ_{SD} for the data sets shown in Figure II-8 are 0.68 ± 0.04 s for $v_r = 5.09$ kHz, 1.79 ± 0.11 s for $v_r = 6.98$ kHz, and 2.22 ± 0.10 s for $v_r = 9.23$ kHz. The error values given are one standard deviation of τ_{SD} as determined by weighted regression. To show convincingly that there is no spin diffusion between peaks A and B, the SPARTAN pulse sequence was also used on the fluorapatite sample containing 0.8 wt.% antimony, since peak B was most well resolved for this sample. As in the 1.7 wt.% sample, the height of the main peak C decreases noticeably as peak A becomes positive and peak B remains constant within experimental error. The spin diffusion time constant for this sample was $1.95 \% \pm 0.31$ s for $v_r = 9.26$ kHz.

To test the effect of temperature on the spin diffusion rate, the SPARTAN experiment was performed on the sample containing 1.7 wt. % antimony at a temperature of 223 K and $v_r = 8.10$ kHz. The measured rate of spin diffusion between peaks A and C at the lower temperature was essentially unchanged ($\tau_{SD} = 1.89 \pm 0.12$ s).

Attempts to monitor spin diffusion by inverting peak B and observing cross relaxation to the other peaks were unsuccessful since no combination of pulse lengths or power levels was found that could selectively invert peak B without significantly exciting peak C.
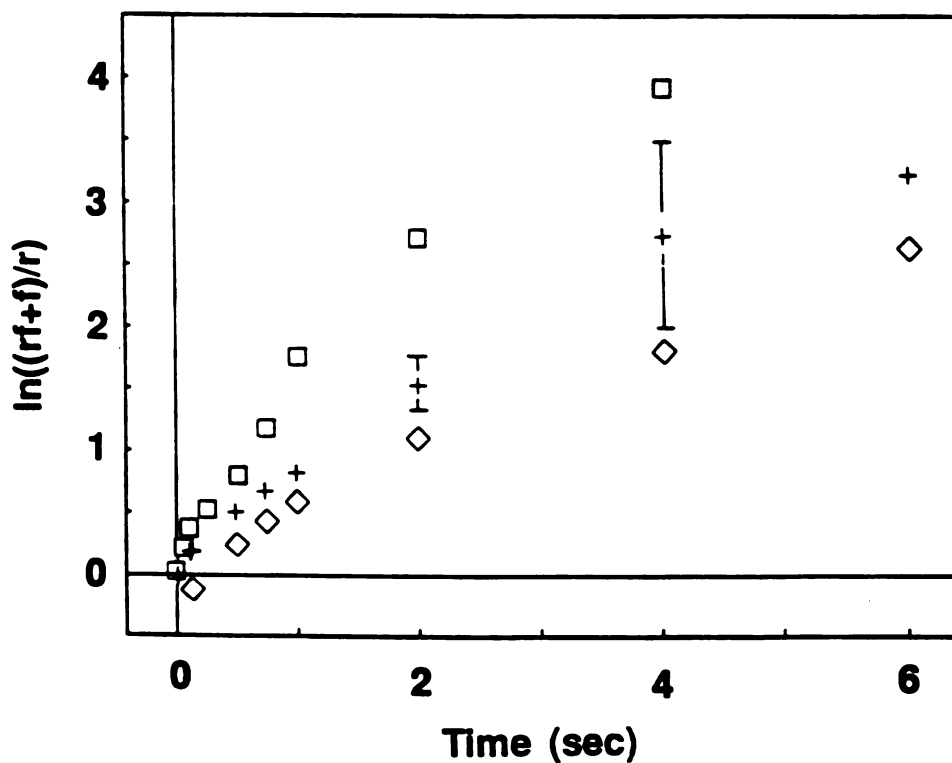
Figure II-8. Measurement of spin diffusion rates between peaks A and C in the ^{19}F

MAS-NMR spectra of fluorapatite containing 1.7 wt. % antimony at three different

spinning speeds using the SPARTAN pulse sequence:

ln ((rf + f)/r) vs. τ_m (see text). ν_r= 9.23 kHz ($\Diamond$), 6.98 kHz (+), and 5.09 kHz (o) .

Representative error bars are included on two of the data points.

4. Discussion

The discussion portion of this paper is divided into three sections. The first section discusses the basic principles of spectral spin diffusion, and shows how the experimental results involving spin diffusion enable one to assign the ^{19}F MAS-NMR peaks to specific antimony-perturbed fluoride ions in the apatite lattice. The second section first demonstrates that potential effects upon the MAS-NMR spectra arising from the presence of quadrupolar antimony nuclei do not appear, due to rapid relaxation of the quadrupolar nuclei. It then discusses the quantitative aspects of the ^{19}F MAS-NMR spectra, and the agreement between the NMR results and IR results regarding the amount of antimony actually incorporated into the apatite lattice. In the third and final section the phosphate site is shown to be the only location for antimony in the fluorapatite lattice that is consistent with all of the experimental MAS-NMR results. Molecular modelling of the apatite lattice leads to a plausible assignment of the ^{19}F MAS-NMR spectra.

4.1. Spin Diffusion

Spin diffusion is a term used to describe the transfer of longitudinal(z) magnetization within a homonuclear spin system between different regions of sample via the dipole-dipole coupling of nuclear spins.[35,36] The process is often assumed to exhibit general Fickian diffusion behavior, although we need make no such assumptions here, especially since our system is basically one-dimensional. Spin-diffusion allows paramagnetic centers or mobile domains to act as relaxation sinks for spins throughout the sample, and can manifest itself as a nonexponential spin-lattice relaxation process.[35,36] Spectral spin diffusion refers to the situation where the spins have different resonance frequencies,[37] and is usually observed in single crystals or under MAS conditions. The transfer of polarization is accomplished by the simultaneous exchange of Zeeman magnetization between

two adjacent spins, a process usually referred to as a spin flip-flop. One manifestation of spectral spin diffusion is an equalization of the longitudinal relaxation times of spectrally resolved spins.[38] In a limited number of cases, spectral spin diffusion in solids has been observed directly by selectively inverting the magnetization of one peak and monitoring cross-relaxation to other peaks. [24,25,28,39-41]

Spectral spin diffusion can occur provided inter-spin flip-flops conserve the total Zeeman energy. Sources of energy that can balance any mismatch in the Zeeman energies include large extraneous dipolar spin reservoirs, such as abundant protons[24, 28, 40-43], external radio-frequency fields,[44] and coupling between the spin system and the rotation of the sample.[28, 38, 42, 45, 46] None of the spectra reported here were obtained under such conditions.

Kubo and McDowell[28] have pointed out that the scalar coupling can facilitate spin diffusion under MAS conditions. Through space scalar couplings between ^{19}F nuclei have been reported to be as large as 217 Hz.[47,48] Since the intensity of peak A in the Hahn spin echo experiments was observed to decay monotonically with a time constant (T_2) of 34 ms, any scalar coupling to a neighboring C fluorine nucleus must be less than approximately 15 Hz. Since the magnitude of the scalar coupling (15 Hz) is substantially less than the dipolar coupling, spin diffusion must proceed predominantly through the dipolar interaction.

It is conceivable that atomic motions with spectral density at the frequency difference between peaks A and C could provide energy to compensate for the Zeeman mismatch between these peaks, and thus facilitate spin diffusion. The fact that the spin diffusion rate is essentially unchanged at lower temperatures indicates that if such a mechanism is responsible for the observed spin diffusion, the motion must have an activation barrier less than kT.

Kubo and McDowell[28] have pointed out that only if two identical chemical shielding tensors of neighboring spins have the same orientation will there generally be efficient spin diffusion. This situation certainly applies to the unperturbed fluorine nuclei in the fluorapatite lattice, whose axially symmetric shift tensors have their principal axes along the c-axis of the crystal. However, spin diffusion in MAS-NMR spectra can occur, albeit less efficiently, even if the chemical shielding tensors have a different orientation, or are unequal. For spin diffusion to occur under such conditions, without other sources to provide for Zeeman mismatch, level-crossing must take place.[28] A similar enhancement of spin-diffusion by level-crossing during sample rotation for quadrupolar powder patterns of deuterium nuclei has been reported by Eckman.[49] Since the frequency of each of the resonances varies during the rotor cycle, [50,51] level-crossing can occur when the two frequencies coincide.

The effects of spectral spin diffusion provide information as to whether peaks A, B, and the peak at 73.1 ppm in the ^{19}F MAS-NMR spectra of antimony-containing fluorapatite arise from fluorine atoms in the apatite lattice, or in secondary, non-apatitic phases. Since the ^{19}F T_1 values vary greatly (and irregularly) among the antimony containing fluorapatite samples (130 to 380 sec), the primary source of longitudinal relaxation is probably paramagnetic impurities introduced during synthesis, and not intrinsic lattice motions. When paramagnetic species are present, the magnetization recovery is expected to be,[35] and is observed to be, nonexponential. However, the T_1 values reported in Table 1 were obtained by fitting the relaxation data to a single exponential, which appeared to provide a good fit (no significant breaks in the logarithmic plot of the relaxation data were observable).

The fact that the T_1 values of peaks A, B, C, and the 73.1 ppm peak are identical within experimental error suggests that the spins corresponding to these

peaks are in spin diffusion contact with each other over the long time scale of T_1 (but see below). This implies that the corresponding spins are in the same crystallites, and not in different (secondary) phases. The rate of spin diffusion depends upon, among other factors, the square of the dipolar coupling constant between pairs of spins.[38] Fluorapatite contains parallel linear chains of fluoride ions with intra-chain fluorine atoms 344 pm apart, and with an inter-chain closest fluorine-fluorine distance of 937 pm. The corresponding calculated maximum homonuclear dipolar couplings (internuclear vector parallel to the magnetic field) are 5234 Hz and 262 Hz respectively. The largest fluorine-phosphorus dipolar coupling is ca. 2200 Hz, and the largest phosphorus-phosphorus dipolar coupling is ca. 640 Hz. The spin diffusion we observe in the present system is for a spinning speed (up to 9.23 kHz) significantly exceeding the largest dipolar coupling in the spin system. As far as we are aware, this is the first such case reported. Spin diffusion has been reported to be quenched by MAS spinning speeds that exceed the dipolar couplings,[42] but the quantitative degree of reduction in rate or quenching in this case has apparently not been studied experimentally.

Spectral spin diffusion among peaks in the ^{19}F MAS-NMR spectrum is most likely enabled by an instantaneous match of the frequencies of the spins of peaks due to differences in the chemical shielding tensors of the spins (see above). The isotropic chemical shifts of peaks A and C differ by 4.6 ppm, which is only a small fraction of the total chemical shift anisotropy of 84 or 85 ppm[29,30]. Thus, it is plausible that the frequencies could match during the rotor cycle. Although it was not possible to accurately determine the components of the chemical shielding tensors of peaks A, B, and C, the slight differences in sideband intensities of peaks A and C suggest a difference in the chemical shift anisotropy of each peak.[52] The increase in the spin diffusion rates between peaks A and C at lower spinning speeds is expected since the zero-quantum linewidth would be greater at lower

spinning speeds,[28] thus increasing the time during which the zero-quantum linewidths of peaks A and C overlap during a given rotor period.

The spectral spin diffusion results obtained using the SPARTAN sequence allow assignments of peaks A, B, and C. Figure II-9 shows a geometrical arrangement of the fluorine nuclei of peaks A and B in the fluorapatite lattice that explains both the observed spin diffusion between peak A and peak C and the considerably reduced spin diffusion between peak A and peak B. The model also takes into account the 2/1 intensity ratio of peaks A and B discussed in section 4.2. In this arrangement, the fluorine nuclei of peaks A and C are neighboring, with no intervening peak B nuclei, thus permitting facile spin diffusion. Since peaks A and B arise from fluorine nuclei in different chains, direct spin diffusion between these peaks would be negligible; instead, spin diffusion would proceed indirectly and more slowly through the nuclei of peak C. We should note that a model in which the two fluorine nuclei of peak A are on different chains would also be consistent with the spin-diffusion results; however, structurally this model is less plausible (see section 4.3.1).

4.2. Quantitative aspects of ^{19}F MAS-NMR results and extent of antimony incorporation

In order to obtain quantitative information about the amount of antimony in the fluorapatite lattice through its effect on the ^{19}F MAS-NMR spectrum, it is important to consider the effect that the quadrupolar antimony nucleus could have on the spectrum of the spin-1/2 fluorine nucleus. Antimony has two quadrupolar isotopes: ^{121}Sb with I = 5/2 and a natural abundance of 57.25%, and ^{123}Sb with I = 7/2 and a natural abundance of 42.75%. Effects of half-integral quadrupolar nuclei on the spectrum of a spin-1/2 nucleus under MAS conditions have been observed experimentally and calculated theoretically. [53-55] Generally, magic angle sample spinning fails to eliminate the effect of dipolar coupling on the spectrum of a spin-

1/2 nucleus dipolar coupled to a quadrupolar nucleus, because the axis of quantization of the quadrupolar spin is not parallel to H_0. The MAS-NMR spectrum of a spin-1/2 nucleus dipolar coupled to a quadrupolar nucleus is usually a complicated powder pattern with singularities, whose total breadth is roughly on the order of the dipolar coupling between the spin-1/2 and quadrupolar nuclei. The details of the pattern are governed by the sign and magnitude of the nuclear quadrupole coupling constant, the nuclear spin, and the angles between the principal axes of the dipole and quadrupolar interaction tensors.[53] The nuclear quadrupole coupling constant of the [121]Sb nucleus in fluorapatite has been measured to be approximately 700 MHz.[5]

For antimony nuclei in any of the proposed substitution sites, significant dipolar couplings to both fluorine and phosphorus nuclei would be expected to produce observable quadrupolar effects in the ^{19}F and ^{31}P MAS-NMR spectra. The calculated dipolar couplings between an [121]Sb ([123]Sb) antimony nucleus occupying the Ca(2), Ca(1) site, or phosphate site and the nearest fluorine nucleus in the fluorapatite lattice are 2.45 kHz (1.33 kHz), 161 Hz (87 Hz), and 630 Hz (340 Hz) respectively. If antimony nuclei were producing quadrupolar effects upon the ^{19}F MAS-NMR spectra, peaks A and B would be much broader than peak C; however, only peak A is slightly broader, and we ascribe this to the presence of two slightly different isotropic chemical shifts (see section 4.3.3). Furthermore, if peaks A or B were influenced by dipolar coupling to antimony they would not be simple Lorenztian peaks but rather complicated powder patterns.[53] The peak at 73.1 ppm and peaks A and B in the 19F MAS-NMR spectra of antimony doped fluorapatite are not part of such a powder pattern, because the intensity of the 73.1 ppm peak varies independently of the intensity of peaks A and B for the various samples.

Paralleling the ^{19}F MAS-NMR results, the ^{31}P MAS-NMR spectra of antimony doped fluorapatite samples fail to exhibit any quadrupolar effects. The
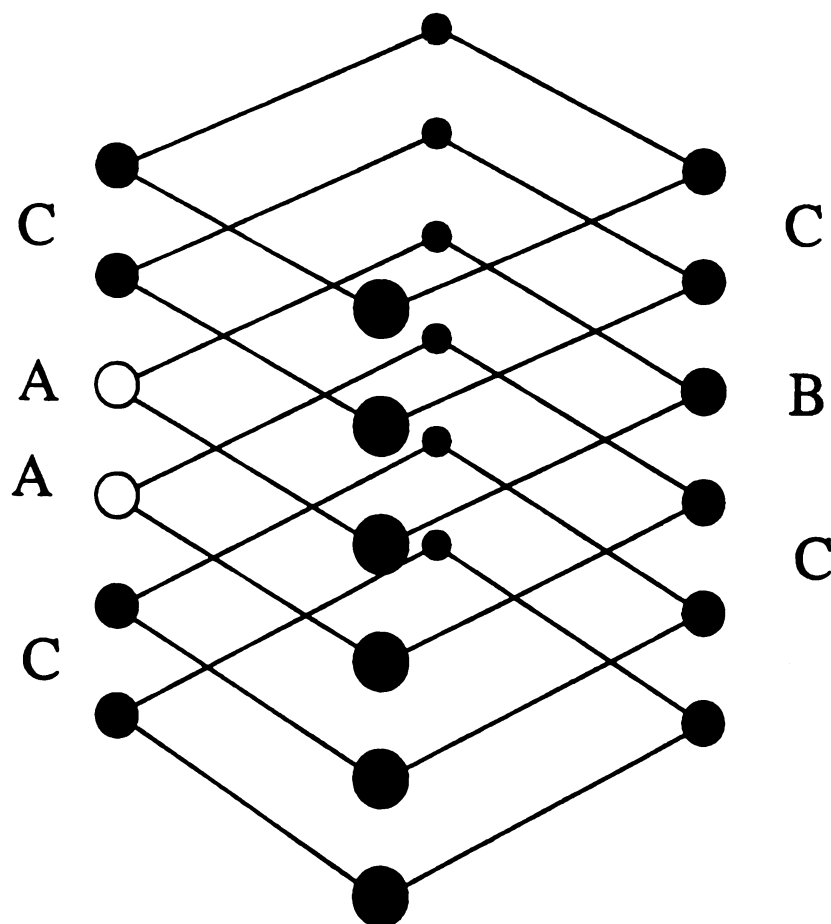
Figure II-9. Schematic diagram as in Fig. II-1, showing the arrangements of fluoride ions giving rise to peaks A and B in the ^{19}F MAS-NMR spectra. The antimony atom (not shown) is between the fluoride ions labelled A and B (see also Fig. II-12).

peak at the isotropic chemical shift of fluorapatite is not broadened at the base nor is its half-height linewidth significantly greater than that of undoped fluorapatite. The most probable explanation for the lack of an effect by the quadrupolar antimony nuclei on the ^{19}F and the ^{31}P MAS-NMR spectra is "self-decoupling" due to rapid spin-lattice relaxation ($T_1 \leq 1 \times 10^{-4}$ s) of the antimony nuclei.[53]

In the ^{31}P MAS-NMR spectrum of $SbPO_4$ the isotropic peak has a $\Delta v_{1/2}$ of 4 ppm, about ten times greater than that of fluorapatite. The increased linewidth in this case may arise from the above quadrupolar effect upon the phosphorus nuclei dipolar coupled to antimony nuclei; presumably in this case the antimony spin-lattice relaxation time is insufficiently short for complete "self-decoupling" to occur.

Having demonstrated the absence of quadrupolar effects upon the MAS-NMR spectra of antimony-doped fluorapatite, we will now discuss the relative quantitation of the ^{19}F MAS-NMR peaks in relation to the amount of antimony present. Figure II-10 is a plot, from the deconvolution data given in Table II-1, of the intensity of peak A in the ^{19}F MAS-NMR spectra vs. the total wt. % antimony in the samples. The lack of a meaningful correlation indicates that some antimony must go into a secondary phase or a site in the fluorapatite lattice other than the one giving rise to peak A. In the samples containing 1.3, 1.7, and 2.1 wt. % antimony the antimony not associated with peak A is most likely in a site in the fluorapatite lattice that gives rise to the peak at 73.1 ppm, as will be discussed in section 4.3.3. Since the ^{19}F and ^{19}P MAS-NMR spectra of the sample containing 3.0 wt. % antimony do not contain peaks with enough intensity to account for the antimony that is not associated with peak A, the "missing" antimony must be in a phase that does not contain fluorine or phosphorus. X-ray powder diffraction data (of the identical 3.0 wt. % antimony sample used in this study) suggest that this phase is calcium metaantimonate.

The solid line in Figure II-10 is the theoretical relationship expected if two fluorine nuclei are affected by each antimony atom in the lattice and all of the antimony is incorporated into the lattice. Since two of the samples (0.18 wt. % and 0.8 wt. %) have peak A intensities on or near this line, there are most likely two "A" fluorine atoms affected per incorporated antimony atom. It is unlikely that peak A arises from three or more fluorine atoms per incorporated antimony atom for several reasons. The amount of incorporated antimony as determined by IR (see next paragraph) for numerous samples containing less than 0.8 wt. % antimony is proportional to the total antimony content,[56] suggesting that all of the antimony present at these relatively low concentrations is incorporated into the apatite lattice. Furthermore, [fluorine A]/[Sb] molar ratios greater than 2/1 are difficult to reconcile with any of the models of antimony substitution discussed in section 4.3. Since the ratio of the area of peak A to peak B is 2:1 from the difference spectroscopy results, we can conclude that peak B arises from *one* fluorine nucleus perturbed by each antimony atom in the lattice.

The fluorescence of antimony doped fluorapatite has been shown to be directly proportional to a specific peak in the IR spectrum at 686 cm^{-1}.[8] The intensity of this IR band can therefore be used to determine the mole fraction of (fluorescence-active) antimony in the lattice of a given sample, using the 0.8 wt.% sample as a calibration standard (assuming that all antimony in this sample is incorporated into the lattice, as the above paragraph indicates). Figure II-11 is a plot from the deconvolution data given in Table II-1 of the intensity of peak A in the ^{19}F MAS-NMR spectra vs. the mole fraction of antimony in the lattice as determined by IR. The mole fraction antimony is calculated using the defect formula χ_{Sb} = [mol Sb]/[molCa$_5$F(PO$_4$)$_{3-x}$(SbO$_3$)$_x$]. The linearity of this plot not only confirms that peak A arises from antimony incorporated into the apatite lattice, but more importantly demonstrates that this peak is related to the specific antimony site

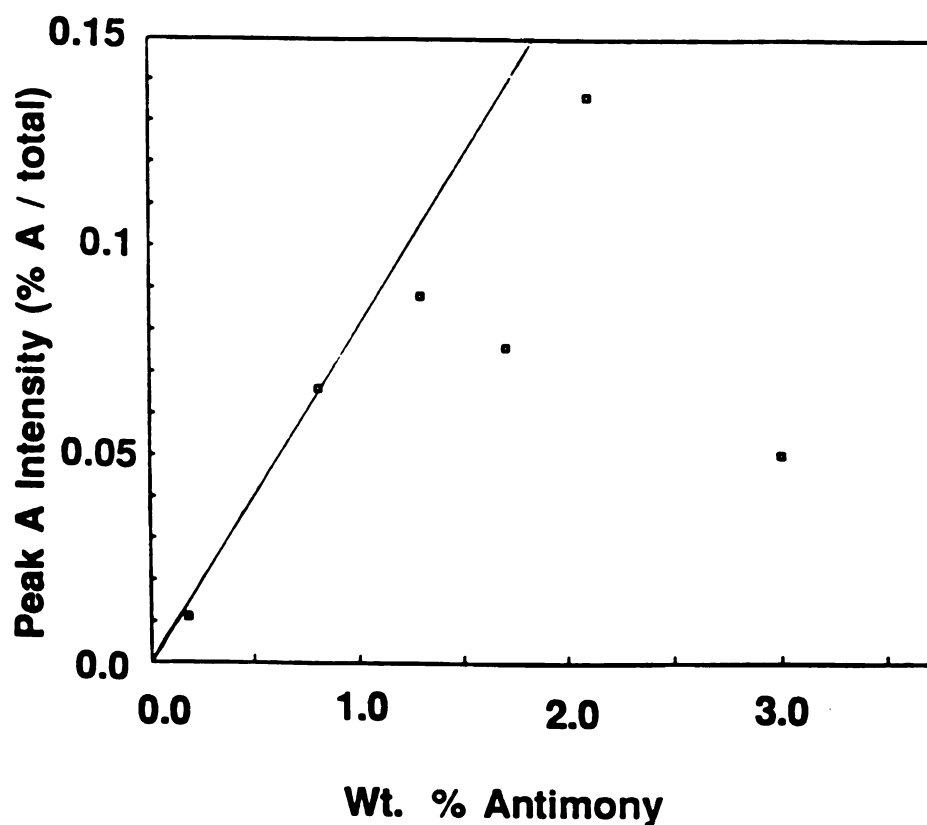Figure II-10. Plot of the[19]F MAS-NMR intensity of peak A obtained from deconvolution (see Table II-1) expressed as the fraction of the total intensity vs. the wt. % antimony(III). Data were obtained from spectra in Fig. II-6. Solid line is theoretical plot, with two assumptions: that peak A arises from two fluorine atoms per antimony atom, and that all of the antimony is incorporated into the apatite lattice.

responsible for fluorescence. The slope of the plot in Figure II-11 is 1.97 ± 0.18, or approximately two, since there are two fluorine nuclei affected by each antimony atom in the lattice.

4.3. Antimony substitution sites

In order to make specific assignments of peaks A and B in the ^{19}F MAS-NMR spectra of antimony doped fluorapatite, we must consider which of the possible antimony substitution sites can account for all of the experimental results. The antimony substitution site must be close enough to two apatitic fluorine nuclei to significantly perturb their ^{19}F chemical shifts, and must produce an equal or nearly-equal perturbation (since peak A is a single peak 4.6 ppm from the main apatite peak). It must also be close enough to a single fluorine nucleus to slightly perturb its ^{19}F chemical shift (since peak B is 1.6 ppm from the main apatite peak). As discussed in the spin diffusion section, the fluorine nuclei giving rise to peaks A and B must be in different fluorapatite chains. Finally, the substitution site of antimony must produce a negligible perturbation of the ^{31}P chemical shift.

Simulations of ^{31}P MAS-NMR spectra of the 2.1 wt. % sample show that if each antimony atom were to perturb three phosphorus nuclei (the smallest number of neighboring phosphorus atoms an antimony atom would have in any substitution site), a chemical shift perturbation of 0.4 ppm would be easily detectable as a shoulder on the main apatite peak. Although the effects upon the ^{31}P chemical shift of replacing calcium in the fluorapatite lattice by strontium or barium are rather small (2 ppm), unlike antimony, these ions have the same charge as calcium. Turner et al.[57] have shown an approximate empirical correlation of the ^{31}P chemical shift in metal phosphates with the quantity $Zr^{-1/2}$, where Z is the formal cation charge and r its ionic radius. Neglecting the structural differences between compounds, this correlation rationalizes the much larger effect upon the ^{31}P chemical shift of
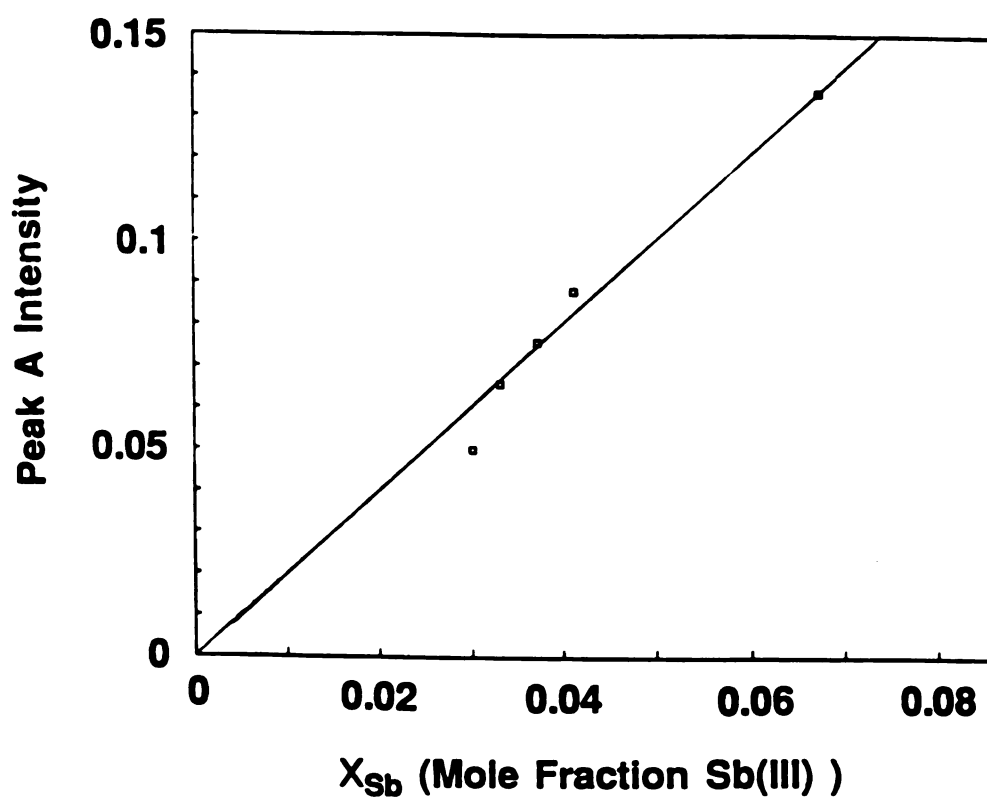
Figure II-11. Plot of ^{19}F MAS-NMR intensity of peak as in Fig. II-10 vs. the mole fraction of antimony incorporated into the apatite lattice as determined by IR (see text).

replacing Ca^{2+} (Z=2, r=99 pm) by Sb^{3+} (Z=3, r=76 pm) rather than Sr^{2+} (Z=2, r=112 pm) or Ba^{2+} (Z=2,r= 134 pm).[58]

The ^{31}P chemical shift of antimony phosphate, which has an antimony(III) atom sharing each oxygen atom of the phosphate tetrahedron,[59] is -18.3 ppm. If an antimony atom occupies a calcium site in the apatite lattice, it would be adjacent to a phosphate tetrahedron. The Sb-O-P linkage would then be expected to produce a detectable difference in the ^{31}P MAS-NMR spectrum, on the order of 5 ppm (1/4 of the difference between the ^{31}P chemical shift of FAP and that of $SbPO_4$).

In the following three sections we will discuss the three proposed sites for antimony substitution in light of the combined ^{19}F and ^{31}P MAS-NMR results.

4.3.1. Ca(1) site

Previous studies have provided evidence against the Ca(1) site as the antimony substitution site.[5,9] The lack of axial symmetry for the antimony nuclear quadrupole coupling constant obtained from Mossbauer spectroscopy has been used to argue against the Ca(1) site, which has threefold symmetry in the apatite lattice. However, although not explicitly discussed, the mechanism of charge compensation must be considered. If antimony occupied the Ca(1) site, charge balance would most likely be accomplished either by removing two Ca(1) ions (or alternatively one Ca(1) ion and one Ca(2) ion) and one fluoride ion, or by removing one Ca(1) ion and replacing a fluoride ion with an O^{2-} ion. In both cases, the antimony atom would reside in the center of a triangular prism formed from three columns of fluoride ions, but strict threefold symmetry would be absent. We should note that the Mossbauer results provide an additional argument against the Ca(1) site, since the theoretically calculated antimony nuclear quadrupole coupling constant for Sb^{3+} replacing Ca(1) with no other lattice distortion is much smaller than the measured value.

The ^{19}F MAS-NMR results do not explicitly rule out the Ca(1) site as a substitution site for antimony atoms. If either of these charge compensation schemes above were invoked, peak B in the ^{19}F MAS-NMR spectra would have to be assigned to a fluoride ion in the column of fluorides containing the vacancy (or oxygen ion), and peak A would be assigned to two identical fluoride ions in the other two chains of the triangular prism. This model offers no explanation for the greater linewidth of peak A compared to peak C (Table II-1). Finally, the presence of only one fluoride ion corresponding to peak B, rather than two essentially equivalent fluoride ions above and below the vacancy, is difficult to rationalize in the above model. Perhaps the most definitive experiment to rule out this model solely on the basis of ^{19}F MAS-NMR would be to demonstrate with a type of REDOR experiment[19] that peak A arises from two adjacent fluoride ions in the same chain.

The ^{31}P MAS-NMR NMR results provide the strongest evidence against the Ca(1) site. This conclusion is based on the lack of a distinct antimony-related resonance in the ^{31}P MAS-NMR spectra, despite the expectation that such a peak should be readily observable (see above).

4.3.2. Ca(2) site

The combined MAS-NMR results seem to rule out this possibility. As discussed in section 4.3.1, an antimony atom occupying a Ca(2) site would be expected to produce a detectable additional peak in the ^{31}P MAS-NMR spectra, which is not observed.

The ^{19}F MAS-NMR results provide additional evidence against the Ca(2) site. If an antimony atom were in the Ca(2) site, a fluoride ion adjacent to the antimony atom would be replaced by an O^{2-} ion for charge compensation. Assuming that the two fluoride ions adjacent to the O^{2-} ion were responsible for peak A, the spin diffusion results require that the fluoride nucleus giving rise to peak B must be in an adjacent fluoride chain (Figure II-9). However, this fluoride nucleus

would be distant (700 pm away) from the antimony atom and separated from it by five chemical bonds (Sb-O-P-O-Ca-F); the perturbation of the fluorine chemical shift observed for peak B is more difficult to rationalize in this case than for the phosphate model below.

4.3.3. Phosphate site

Both the ^{31}P and ^{19}F MAS-NMR results support the phosphate site as the location of antimony in the apatite lattice. If an antimonate tetrahedron (three oxygen atoms and a lone electron pair surrounding antimony) occupied the site of a phosphate tetrahedron, and the lone electron pair on the antimony atom occupied the site of an oxygen atom nearest the fluoride chain (Figure II-12), the environment of *two* Ca(2) ions normally bonded to this oxygen atom would be perturbed. The two fluoride ions adjacent to each of these perturbed Ca(2) ions can therefore be assigned to peak A. Since these two fluoride ions do not have an identical bonding geometry to the antimony ion, they would be expected to have slightly different chemical shifts. Such a small chemical shift difference may be responsible for the approximately 120 Hz (0.32 ppm) greater linewidth of peak A compared to peak C. The downfield shift of peak A may be qualitatively ascribed to an increased paramagnetic contribution in the Ramsey theory of chemical shifts,[60] due to a greater tendency of the Ca^{+2} ion missing an O^{2-} ligand to withdraw electrons from the fluoride ions. To satisfy the spin diffusion results (Figure II-9), peak B must be assigned to a fluoride ion in the closest linear chain of fluoride ions, with a three-bond bonding network of Sb-O-Ca-F linking the antimony ion to the fluoride ion (Figure II-12). The chemical shift difference between peak B and peak C (1.6 ppm) is expected to be less than that between peak A and peak C, since the perturbation is less. Although the fluoride ions adjacent to the peak A fluoride ions have the same bonding network to the antimony atom (Sb-O-Ca-F) as the fluoride ion assigned to peak B, we must assume that their chemical shift is undetectably
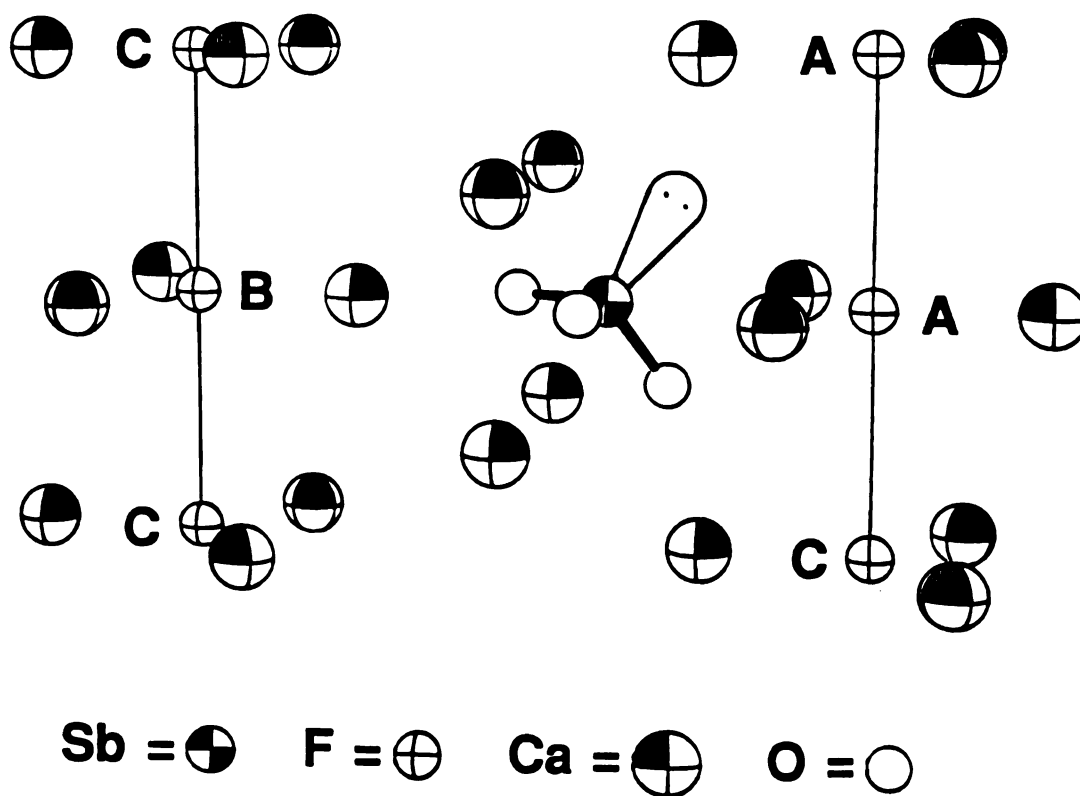
Figure II-12. ORTEP drawing of fluorapatite lattice, with antimony(III) and its lone pair placed exactly at the phosphate site. The assignment of fluoride ions to peaks A and B in the ^{19}F MAS-NMR spectra is indicated (see text).

different from that of the peak C fluoride ions.

The lack of an antimony related peak in the ^{31}P MAS-NMR spectra is also readily explicable if antimony occupies the phosphate site. The bonding network to the nearest phosphorus atom would be: Sb-O-Ca-O-P. The presence of four bonds between the antimony and phosphorus atoms, rather than two bonds as for the Ca(1) and Ca(2) site models, would plausibly result in the absence of a significant perturbation of the ^{31}P chemical shift.

Having shown that peaks A and B arise from fluorine nuclei near an antimony atom with a distinct orientation in the phosphate site, we will now attempt to assign the 73.1 ppm peak. As shown in section 4.1 the fluorine nuclei giving rise to the weak peak at 73.1 ppm must be in the fluorapatite lattice. The peak at 73.1 ppm does not arise from fluoride ions at the surface of the crystallites, since the specific surface area measurements indicate that only approximately one millionth of the fluoride ions are at or near the surface of the crystallites, whereas the intensity of the 73.1 ppm peak is as high as 4.6% of the total intensity. The 73.1 ppm peak in the ^{19}F MAS-NMR spectra of the fluorapatite samples containing 2.1, 1.7, and 1.3 wt. % antimony cannot be due to the antimony atom in the phosphate site that gives rise to peaks A and B, since its intensity does not correlate with that of these latter peaks. The 73.1 ppm peak is not due to an antimony atom that occupies one of the Ca sites, based on the ^{31}P NMR arguments in sections 4.3.1 and 4.3.2.

It is possible that the 73.1 ppm peak arises from an apatitic fluoride ion near an antimony atom in the phosphate site whose electron lone pair occupies the site of a missing oxygen atom directed away from the nearest adjacent fluoride chain (unlike the antimony associated with A and B). Supporting this assignment is the correlation observed (except for the 3.0 wt.% sample) of the intensity of the 73.1 ppm peak with the amount of antimony not associated with peaks A and B.

Specifically, when the ^{19}F MAS-NMR intensity of the 73.1 ppm peak (expressed as the fraction of the total intensity) is plotted versus the mole fraction of antimony atoms in the sample not associated with peaks A and B, the three points can be fit to a line with a slope of 1.01 and a correlation coefficient of 0.93, indicating that there is one antimony atom associated with each fluorine atom giving rise to the 73.1 ppm peak. The increased linewidth of this peak may be due to an observable quadrupolar effect from the antimony nuclei. One fact is not convincingly rationalized by the assignment of the 73.1 ppm peak to a single fluorine nucleus perturbed by an antimony atom in the phosphate substitution site with a different Sb lone pair orientation. The chemical shift difference between the 73.1 ppm peak and the main peak at 64.0ppm is twice as large as that between peak A and the main peak, even though the distance and bonding linkage from the antimony atom to the nearest fluorine nuclei are nearly the same for the proposed assignments.

5. Conclusion

We have shown by ^{31}P and ^{19}F MAS-NMR of antimony-doped fluorapatite samples that antimony(III) occupies the phosphate site in the apatite lattice rather than one of the cationic (calcium) sites. Our data strongly support the model of Mishra and coworkers,[5] in which the PO_4^{3-} group is replaced by a (slightly displaced) SbO_3^{3-} moiety, with the antimony 5s electron lone pair directed towards the missing oxygen atom site. The MAS-NMR results also show that these samples contain a maximum of 1.6 wt. Sb^{3+} in this well-defined lattice site, with most of the excess antimony going into a secondary site.

Since we are not aware of previous studies of antimony(III) dopant sites in ionic lattices, it is difficult to draw conclusions regarding the generality of the behavior we observe. At least in this one instance, we have shown that Sb^{3+}, rather than substituting for a divalent cation of larger ionic radius (99pm vs. 76pm),[58] instead essentially replaces a formal $P^{5+}-O^{2-}$ moiety. In this sense,

antimony(III) could be said to resemble a non-metal more than an alkaline earth ion. The oxygen coordination polyhedra may also be influential in determining the bonding mode, with the three oxygen atoms of a phosphate group providing the hemihedral coordination common in crystal structures of antimony(III) compounds.

High-field ^{19}F MAS-NMR is a useful technique for quantifying the amount of antimony actually incorporated into the fluorapatite lattice. It can readily detect antimony levels as low as 0.2 wt.% in a single scan. This study demonstrates several advantages to studying substitution by dopants through their effect on magnetically-active nuclei rather than by direct observation of the dopant nuclear resonance, even assuming the latter is observable. First, it is easier to distinguish actual incorporation of the dopant into the host lattice from possible formation of secondary phases. Also, a single dopant site may result in unequal perturbations of a number of atoms of the host, thus providing more detailed structural information. The influence of spin diffusion upon the ^{19}F MAS-NMR spin-lattice relaxation times was important in this study in establishing that the perturbed peaks arise from fluoride ions in the apatitic lattice. We have shown that the rate of spin diffusion between spectrally-resolved peaks can be quantitatively measured by using the selective-excitation SPARTAN pulse sequence in a one-dimensional NMR experiment. The spectral spin diffusion rates measured using the SPARTAN sequence have enabled us to assign the two peaks perturbed by antimony to fluoride ions on *different* linear chains. Difference spectra have shown that these two peaks are present in a 2/1 intensity ratio, consistent with expectations based on molecular models.

The observation of spectral spin diffusion for MAS spinning speeds greater than the maximum dipolar coupling in the spin network is an interesting experimental fact; we are aware of only one other comparable result that has been briefly alluded to.[61] If this behavior is fairly general (occuring either via level

crossing or atomic motion) spin diffusion measurements obtained using the SPARTAN sequence may prove very useful for assigning MAS-NMR peaks. It would also be worthwhile to investigate theoretically as well as experimentally the "quenching" of spin diffusion by MAS at high spinning speeds.[28,42]

6. References

1. S. Naray-Szabo. *Z. Krist.*75, 387 (1930).

2. D. McConnell. *Applied Mineralogy.* edited by A. V. D. Frechette, H. Kirsch, L. B. Sand, and F. Trojer. (Springer-Verlag, New York, 1973).

3. R. W. Warren. *Phys. Rev. B.* 2, 4383 (1970).

4. R. W. Warren and R. Mazelsky. *Phys. Rev. B.* 10, 19 (1974).

5. K. C. Mishra, R. J. Patton, E. A. Dale, and T. P. Das. *Phys. Rev. B.* 35,1512 (1987).

6. T. S. Davis, E. R. Kreidler, J. A. Parodi and T. F. Soules. *J. Lumin.* 4, 48 (1971).

7. R. W. Warren, F. M. Ryan, R. H. Hopkins, and J. Van Broekhoven. *J. Electrochem. Soc.* 122, 752 (1975).

8. B. G. DeBoer, A. Sakthivel, J. R. Cagle , and R. A. Young. Acta. Crystallog. in press.

9. J. G. Rabatin, G. R. Gillooly, and J. W. Hunter. *J. Electrochem. Soc.* 114, 956 (1967).

10. E. R. Andrew. *Progress in Nuclear Magnetic Resonance Spectroscopy,* edited by J. W. Emsley, J. Feeney, and L. H. Sutcliffe (Pergamon, New York, 1971).

11. W. P. Rothwell, J. S. Waugh, and J. P. Yesinowski. *J. Am. Chem. Soc.* 102, 2637 (1980).

12. J. P. Yesinowski and M. J. Mobley. *J. Am. Chem. Soc.* 105, 6191 (1983).

13. K. A. Smith and D. P. Burum. *J. Magn. Reson.* 84, 85 (1989).

14. M. Mehring, in *NMR Basic Principles and Progress* Volume 11 edited by P. Diehl, E. Fluck, and R. Kosfeld. (Springer-Verlag, Berlin, 1976).

15. B. C. Gerstein, C. Chow, R. G. Pembleton, and R. C. Wilson, *J. Phys. Chem.* **81**, 565 (1977).

16. J. P. Yesinowski and H. Eckert, *J. Am. Chem.Soc.***109**, 6274 (1987).

17. J. P. Yesinowski, H. Eckert, and G. R. Rossman. *J. Am. Chem. Soc.* **110**, 1376 (1988).

18. M. M. Maricq and J. S. Waugh. *J. Phys. Chem.* **70**, 3300 (1979).

19. T. Gullion and J. Schaefer. J. Magn. Reson. 81, 196 (1989).

20. M. Munowitz, W. P. Aue, and R. G. Griffin. *J. Chem. Phys.* **77**, 1686 (1982).

21. J. E. Roberts, et. al. *J. Am. Chem. Soc.* **109**, 4163 (1987).

22. C. E. Bronnimann, R. C. Zeigler, and G. E. Maciel. *J. Am. Chem. Soc.* **110**, 2023 (1988).

23. P. Caravatti, J. A. Deli, G. Bodenhausen, and R. R Ernst. *J. Am. Chem. Soc.* **104**, 5506 (1982).

24. A. Kubo and C. A. McDowell. *J. Chem. Phys.* **89**, 63 (1988).

25. V. Bork and J. Schaefer. *J. Magn. Reson.* **81**, 196 (1989).

26. L. B. Moran, J. K. Berkowitz, and J. P. Yesinowski. submitted to J. Am. Chem. Soc.

27. G. Bodenhausen, R. Freeman, and G. A. Morris. *J. Magn. Reson.* **23**, 171 (1976).

28. A. Kubo, and Charles A. McDowell. *J. Chem. Soc.,Faraday Trans.* **84**, 3713 (1988). J. L. Carolan. *Chem. Phys. Let.* **12**, 389 (1971).

29. A. M. Vakhrameev, S. P. Gabuda, and R. G. Knubovets. *J. Struct. Chem.* (USSR). **19**, 256 (1978).

30. W. Van der Lugt and W. J. Caspers. *Physica* **30**, 1658 (1964).

31. W. P. Rothwell and J. S. Waugh *J. Chem. Phys.***74**, 2721 (1981).

32. A. T. Kreinbrink, et. al. *J. Magn. Reson.* **88**, 267 (1990).

33. C. Connor, A. Naito, K. Takegoshi, and C. A. McDowell. *Chem. Phys. Lett.* **113**(2), 123 (1984).

34. N. Bloembergen. *Physica*, **15**, 386 (1949).

35. A. Abragam. *The Principles of Nuclear Magnetism*, (Oxford, London, 1961), Ch. V and IX.

36. D. Suter and R. R. Ernst. *Phys. Rev. B.* **25**, 6038 (1982).

37. E. R. Andrew, A. Bradbury, R. G. Eades, and T. Wynn. *Phys.Lett.* **4**, 99 (1963).

38. P. Caravatti, M. H. Levitt, and R. R. Ernst. *J. Magn. Reson.* **68**, 323 (1986).

39. D. L. Vanderhart. *J. Magn. Reson.* **72**, 13 (1987).

C. A. Fyfe, H. Gies, and Y. Feng. *J. Am. Chem. Soc.* **111**, 7702 (1989).

40. D. Suter and R. R. Ernst. *Phys Rev. B.* **32**, 5068 (1985).

41. P. M. Hendrichs, M. Linder, and J. M. Hewitt. *J. Chem. Phys.* **85**, 7077 (1986).

42. P. Robyr, B. H. Meier, and R. R. Ernst. *Chem. Phys. Lett.* **162**, 417 (1989).

43. M. G. Colombo, B. H. Meier, and R. R. Ernst. *Chem. Phys. Lett.* **146**, 189 (1988).

44. D. P. Raleigh, M. H. Levitt, and R. G. Griffin. *Chem. Phys. Lett.* **146**, 71 (1988).

45. J. Kowalewski. *Prog. in NMR Spec.* **11**, 1-74 (1976).

46. K. Hirao, H. Nakatsuji, and H. Kato. *J. Am. Chem. Soc.* **95**, 31 (1973).

47. R. Eckman. *J. Chem. Phys.* **79**, 524 (1983).

48. D. P. Raleigh, E. T. Olejniczak, and R. G. Griffin. *J. Chem. Phys.* **89**, 1333 (1988).

49. E. T. Olejniczak, S. Vega., and R. G. Griffin. *J. Chem. Phys.* **81**, 4804 (1984).

50. J. Herzfeld and A. E. Berger. *J. Chem. Phys.* **73**, 6021 (1980).

51. N. Zumbulyadis, P. M. Hendrichs, and R. H. Young. *J. Chem. Phys.* **74**, 1603 (1981).

52. J. Bohm, D. Fenzke, and H. Pfeifer. *J. Magn. Reson.* **55**, 197 (1983).

53. W. W. Fleming, et. al. *Macromolecules.* **13**, 460 (1980); E. M. Menger and W.S. Veeman. *J. Magn. Reson.* **46**, 257 (1982).

54.E. Dale. Private communication.

55. G. L. Turner, K. A. Smith, R. J. Kirkpatrick, and E. Oldfield.

56. J. Magn. Reson. **70**, 408 (1986).

57. Handbook of Chemistry and Physics. edited by R. C. Weast (CRC Press, Cleveland, 1976).

58. B. Kinberger. *Acta. Chem. Scand.* **24**, 320 (1970).

59. N. F. Ramsey. *Phys. Rev.***78**, 699 (1950).

60. N. J. Clayden. *J. Magn. Reson.* **68**, 360 (1983).

Section III

A Method for Detection of Spectral Spin Diffusion from Minor Peaks and Its Application to ^{19}F MAS-NMR of Antimony(III)-Doped Fluorapatite

1. Introduction

Spectral spin diffusion refers to the transfer of longitudinal (z-) magnetization within a homonuclear spin system between nuclear spins having different chemical shifts. Since the process requires a dipolar (or scalar) coupling, structural information is implicit in spin diffusion experiments.[1-10] Although the expectation has been that spin diffusion will be quenched at spinning speeds significantly exceeding the homonuclear dipolar couplings in a spin system,[1] we and others have recently demonstrated the existence of measurable spin diffusion under such conditions.[7-10] Our previous experiments have used the SPARTAN pulse sequence to measure spin diffusion in a one-dimensional ^{19}F MAS-NMR experiment.[7] We present here an improved technique for more accurately measuring spectral spin diffusion under MAS conditions that is particularly suitable when the two peaks involved have different intensities.

2. Results and Discussion

The new technique involves repeatedly saturating a peak and its associated sidebands with selective trains of pulses, and subsequently detecting the rate at which the saturation is transferred to other peaks in the spectrum. We refer to the sequence used (see Fig. III-1) as SINK (Saturation Inter-Nuclear Kinetics). It contains a series of DANTE trains[11] (small flip-angle pulses spaced at intervals of the rotor period, which have the effect of selectively exciting the on-resonance peak

and its associated sidebands), each of which is equivalent to a selective 90° (saturation) pulse. Alternatively, a shaped DANTE train could be used to improve selectivity.[12] Spectral spin diffusion (cross-relaxation) occurs during the mixing period following each DANTE train, and a non-selective 90° observe pulse is given after the last mixing period. The SINK experiment is conceptually related to saturation transfer experiments in solution-state NMR, which use low power continuous rf irradiation to selectively saturate a given peak, and monitor the loss of magnetization in other peaks due to chemical exchange.[13]

We have used the SINK pulse sequence to study calcium fluorapatite $(Ca_5F(PO_4)_3)$ doped with small levels of Sb^{+3} "activator", which is used as a phosphor material in fluorescent lamps. Since the nature of the Sb^{+3} ion substitution site is in dispute,[14-18] we have used ^{19}F (and ^{31}P) MAS-NMR as an indirect probe of the antimony substitution site.[7] Figure III-2a shows the structural arrangement of the identical fluoride ions (black solid circles) in the parent fluorapatite structure. The fluoride ions are separated by a distance of 344 pm, and form parallel linear chains along the (vertical) c-axis of the crystal.[19] The presence of Sb^{3+} in the lattice renders the nearby fluorine nuclei inequivalent, as suggested in Figure III-2b (the bases for these assignments are given in reference 7).

Figure III-3 shows superimposed ^{19}F MAS-NMR spectra of a fluorapatite sample doped with 1.7 wt. % Sb^{+3} (sample preparation and characterization and NMR conditions are given in reference 7; since the chemical shifts of the main apatite resonance (C) and the antimony related peaks in the spectra of antimony doped fluorapatites exhibit slight variations,[7] we have set the chemical shift of peak C in Figure 3 to 64.0 ppm). The spectra of Figure III-3 were obtained using the SINK pulse sequence with varying numbers of selective saturation DANTE pulse trains applied to peak A. The selectivity of the DANTE train was verified by performing the

selective 90° DANTE   nonselective 90°
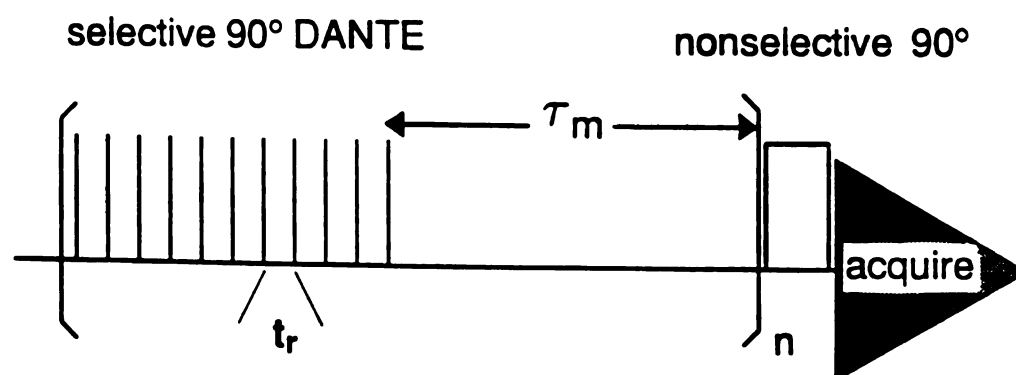
III-1. SINK (Saturation Inter-Nuclear Kinetics) pulse sequence for measuring spin diffusion in MAS-NMR. The rotor period (t_r) is indicated. Rotor-synchronization is carried out using an optical detector to gate the rf pulses. The mixing period for spin diffusion τ_m is fixed and the number of saturation pulse trains n is varied.

SINK experiment with the transmitter frequency on the upfield side of peak C with an offset from peak C equivalent to the frequency difference between peaks A and C. The mixing period (τ_m) should be more than five times T_2^* in order to allow all tranverse magnetization to decay; it was chosen to be 0.1 s for the current experiment. The intensity of the main peak (C) decreases with the number of saturation pulse trains (n) since the spins of peak C are in spin diffusion contact with the spins of peak A. The intensity of peak A in Figure III-3 decreases with increasing n until n = 20 since less magnetization is transferred to peak A in the final mixing period once the magnetization of peak C becomes depleted. After multiple saturation pulse trains that greatly reduce the intensity of peak C, two much weaker peaks that are less strongly affected become resolved. These are the previously-discussed[7] peak B at 65.6 ppm, and an even less-resolved shoulder on the upfield side of peak C at 62.9 ppm that we refer to as peak D. The results of the SINK experiment in Figure III-3 demonstrate even more clearly than the SPARTAN experiment that spin diffusion from A to C nuclei is faster than from A to B nuclei. This observation strengthens our previous conclusion[7] that A and B fluorine nuclei are in different chains (as shown in Fig. III-2b). Similarly, peak D may also arise from apatitic fluoride nuclei near an Sb^{3+} ion in a fluoride chain other than the one containing the A fluorine nuclei.

Spin diffusion time constants (τ_{SD} 's) were obtained by fitting the behavior of the magnetization to a simple model of two site magnetization transfer. The intensities of peak C were calculated numerically using the kinetic equations for a reversible process, where A and C represent the magnetization of the A and C peaks respectively, and k_{for} and k_{rev} are the rate constants for the process;

$$dA/dt = k_{rev}C - k_{for}A \qquad \qquad \text{III-1}$$
$$dC/dt = k_{for}A - k_{rev}C$$
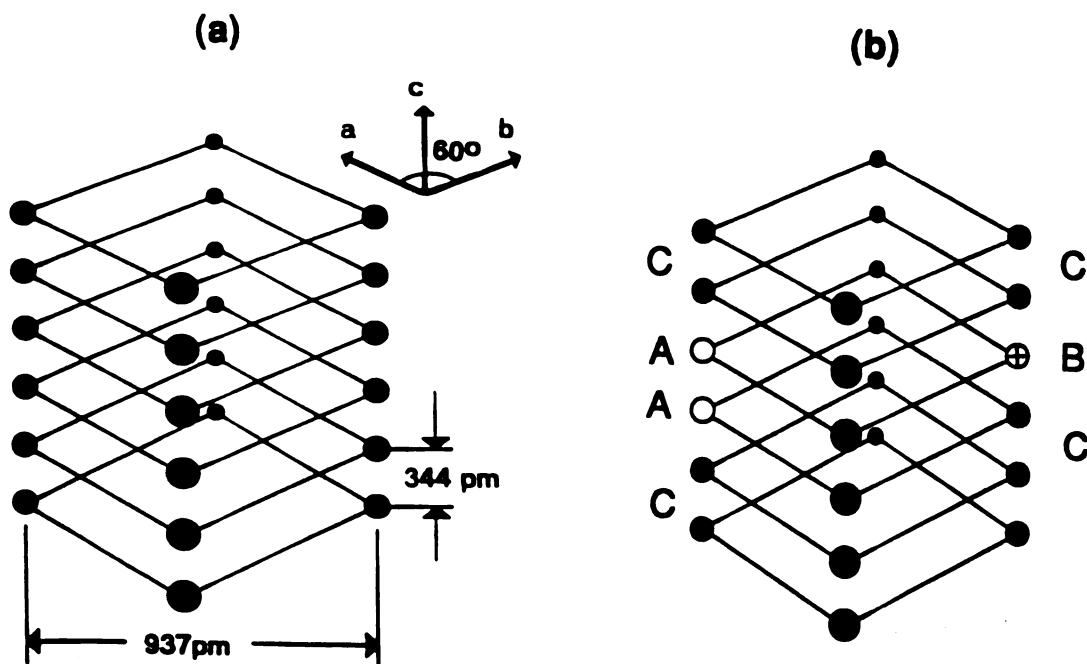
III-2. a) Schematic arrangement of fluoride ions (●) in calcium fluorapatite $(Ca_5F(PO_4)_3)$;[19] b) Assignments based on SPARTAN results[7] of peaks A, B and C in the ^{19}F MAS-NMR spectra of calcium fluorapatite doped with Sb^{3+}; the Sb^{3+} ion is located near the middle of the rhombus drawn involving fluoride ions A and B. The solid black circles represent fluoride ions that give rise to the main peak C in the ^{19}F MAS-NMR spectrum.
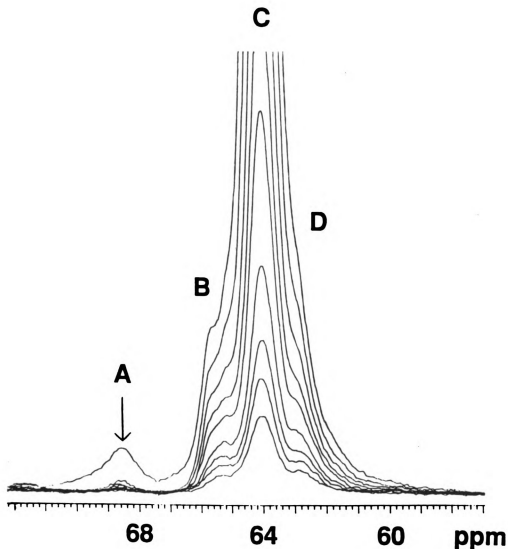
Figure III-3. ^{19}F MAS-NMR (376.29 MHz) superimposed spectra of a calcium fluorapatite sample containing 1.7 wt. % Sb^{+3} dopant obtained using the SINK pulse sequence (Figure III-1). The location of the transmitter rf (at peak A) is indicated on the spectrum with an arrow. The spectra shown were obtained with the number of saturation pulse trains (n) equal to (top to bottom) 1, 10, 20, 30, 40, 60, 80, 100, and 140, with τ_m set to 0.1 s. Seven 1.6 ms pulses (nominally 13° each) comprise the DANTE train, which has a total length of 0.75 ms; the spinning speed ν_r is 8.01 kHz.

The basic scheme for calculating the intensity of peaks C and A at various times t [C(t) and A(t)] involves recalculating the magnetization of the peaks after small increments of time Δt using the following piecewise solutions (including T_1 relaxation) of Eqn (III-1);

$$A(t + \Delta t) = A(t) + (1/\tau_{SD})C(t)\,\Delta t - (1/\tau_{SD})A(t)\,\Delta t + (1/T_{1A})[A_0 - A(t)]\Delta t$$

III-2a

$$C(t + \Delta t) = C(t) + (1/\tau_{SD})A(t)\,\Delta t - (1/\tau_{SD})C(t)\,\Delta t + (1/T_{1C})[C_0 - C(t)]\,\Delta t$$

III-2b

The rate constants k_{for} and k_{rev} have been replaced by $(1/\tau_{SD})$, since the flip-flop cross-relaxation mechanism requires that $k_{for} = k_{rev}$. The last terms in Eqns. III-2a and III-2b correct for longitudinal relaxation. The time increment Δt was chosen to be 0.01 s, a value short enough to accurately calculate the magnetization. The T_1 values (>100 s) used in Eqn. III-2 are reported in reference 7. Equilibrium magnetizations A_0 and C_0 were set equal to values obtained from a single non-selective 90° pulse after allowing for complete relaxation. The effect of the saturation pulse train is incorporated into the fitting procedure by lowering the value of A(t) to a fraction of its previous value each time the sum of the time increments equals a multiple of τ_m. The value of A(t) was not decreased to zero at these times since the DANTE train gives an effective 90° pulse only to the middle of peak A, leaving some positive side-lobes. The amount by which the DANTE train decreased the total A magnetization was determined by integrating peak A after a single DANTE train immediately followed by a non-selective read pulse. Cross-relaxation of the system during the selective DANTE trains has been neglected

since the train duration (0.75 ms) is small compared to the mixing period (τ_m = 100ms).

Since the present system features linear chains of C spins interspersed with A spins, longitudinal magnetization from most of the C spins must be transferred to A spins via other C spins. A thorough treatment of the cross-relaxation dynamics in this system would explicitly include cross-relaxation between C spins; however, we have treated the C spins as a "pool", based on the assumption that C spin polarization redistributes itself rapidly compared to the time scale of cross-relaxation between the A and C spins. This assumption is valid since the two samples studied have the same t_{SD} despite having different C spin chain lengths (caused by different levels of antimony doping).

Figure III-4 shows the peak C intensities calculated using Eqns. III-2 and the measured values plotted versus the total number of saturation pulse trains for the fluorapatite sample doped with 1.7 wt. % Sb^{+3}. The calculated C(t) values were obtained by varying τ_{SD} until the best visual fit was obtained. The spin diffusion time constants τ_{SD} (single exponential) measured from the SINK data for samples containing 1.7 % and 0.8 wt. % Sb^{+3} at a spinning speed v_r = 8.0 kHz are 2.4±0.1 and 2.2±0.1 s respectively, which are close to the values obtained using the SPARTAN pulse sequence.[7]

We note that the final (n > 60) data points could not be accurately fit to the calculated curve regardless of the τ_{SD} value used. The fact that the measured values of C magnetization are greater than the calculated values after many saturation pulse trains (n) suggests that some of the C spins are not in spin diffusion contact with the A spins. The fit of Figure III-4 is substantially improved over the entire range of n if only 95 % of the C spins are allowed to cross-relax with the A spins; the resultant τ_{SD} values remain essentially unchanged. One possible reason that 5 % of the C spins are not in spin diffusion contact with the A spins is
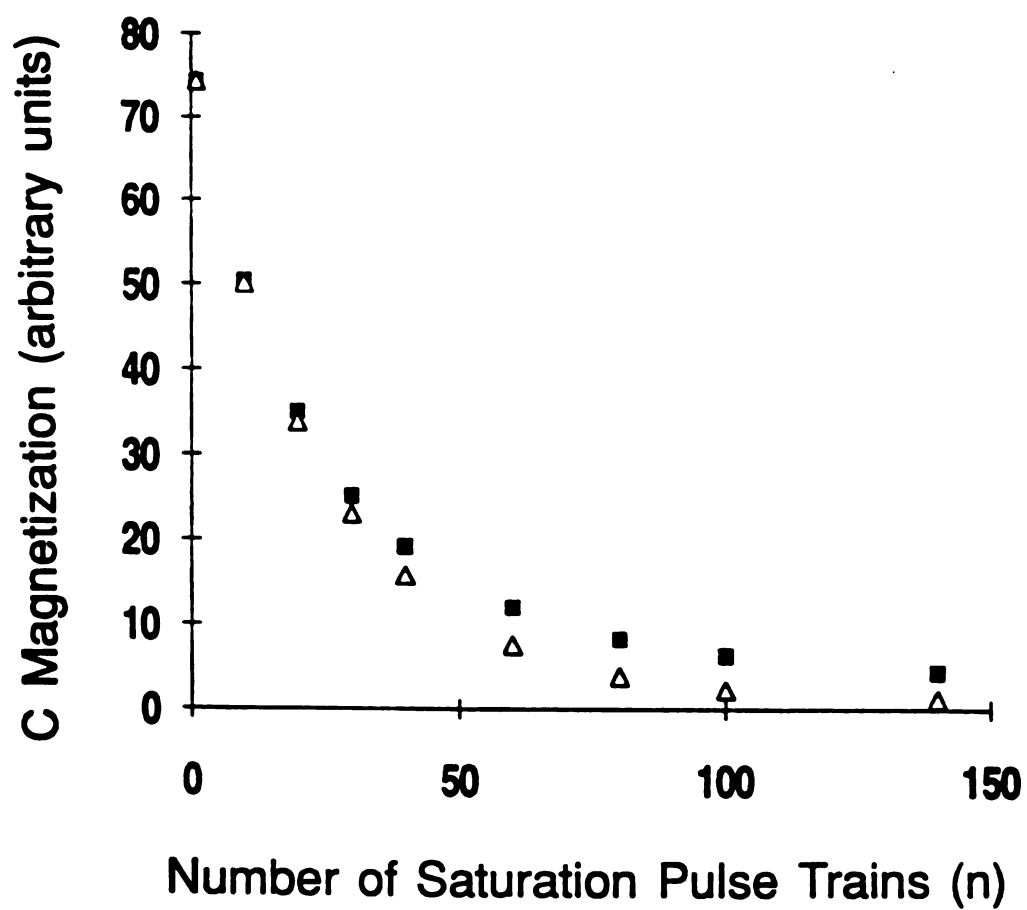
Figure III-4. Calculated (Δ) and measured ($\blacksquare$) peak C intensities (of spectra from Figure III-3) vs. the number of saturation pulse trains (n) applied to peak A. The calculated points were obtained using Eqns. III-2 as described in the text, with a τ_{SD} of 2.4 s.

physical isolation, either due to fluorine vacancies or sample inhomogeneity. A second possible explanation is an orientational dependence of the spin diffusion rate.[9] We have attributed the existence of spin diffusion between peaks A and C to level crossing,[7] the momentary equality at some point in the rotor cycle of the chemical shifts of two adjacent spins with different chemical shielding tensors.[5] For those crystallite orientations that do not lead to level crossing, spin diffusion will be greatly slowed.

3.Conclusions

The SINK pulse sequence has several advantages over the spin diffusion measurement technique (SPARTAN) previously used[7,9] and other spin diffusion experiments.[4,8,10] The SINK experiment provides more accurate spin diffusion time constants (τ_{SD}), particularly for spin diffusion from minor spectral features to major components. The SINK pulse sequence can also be used to clarify crowded regions of the spectrum and reveal "hidden peaks" by saturation of an overlapping peak through saturation transfer. Finally, the SINK pulse sequence is well suited for detecting long range spin diffusion in spatially separated phases such as polymer blends or epitaxially-related crystal phases, since a spectrally resolved resonance of one phase may be saturated for lengthy periods while magnetization from the spins of the other phase slowly disappears. We believe that detecting spectral spin diffusion via the SINK sequence will be useful for making MAS-NMR assignments of such widely abundant spins as ^{19}F, ^{1}H, and ^{31}P and for studying impurity sites in disordered or glassy solids. For surface studies, this approach should also provide useful information about clustering, spatial proximity, and epitaxial relationships.

REFERENCES

1. D. Suter and R. R. Ernst, *Physical Review B,* **32** (1985) 5068.

2. P. Caravatti, G. Bodenhausen and R. R. Ernst, *Journal of Magnetic Resonance,* **55** (1983) 88.

3. P. Caravatti, M. H. Levitt and R. R. Ernst, *Journal of Magnetic Resonance,* **68** (1986) 323.

4. N. J. Clayden, *Journal of Magnetic Resonance,* **68** (1986) 360.

5. A. Kubo and C. A. McDowell, *Journal of the Chemical Society. Faraday Transactions,* **84** (1988) 3713.

6. C. A. Fyfe, H. Gies and Y. Feng, *Journal of the American Chemical Society,* 111 (1989) 7702.

7. L. B. Moran, J. K. Berkowitz and J. P. Yesinowski, *Physical Review B.* **45** (1992) 5347.

8. W. Kolodziejski, H. He and J. Klinowski, *Chemical Physics Letters,* **191** (1992) 117.

9. Z. Zhang, J. H. Kennedy and H. Eckert, *Journal of the American Chemical Society,* **114** (1992) 5775.

10. K. Takegoshi, I. Tanaka, K. Hikichi and S. Higashida, *Macromolecules,* **25** (1992) 3392.

11. G. Bodenhausen, R. Freeman and G. A. Morris, *Journal of Magnetic Resonance,* **23** (1976) 17.

12. W. S. Warren, *Journal of Chemical Physics,* **81** (1984) 5437.

13. S. Forsen and R. A. Hoffman, *Journal of Chemical Physics,* **39** (1963) 1963.

14. K. C. Mishra, R. J. Patton, E. A. Dale and T. P. Das, *Physical Review B,* **35** (1987) 1512.

15. T. S. Davis, E. R. Kreidler, J. A. Parodi and T. F. Soules, *Journal of Luminescence,* **4** (1971) 48.

16. R. W. Warren, F. M. Ryan, R. H. Hopkins and J. Van Broekhoven, *Journal of the Electrochemical Society,* **122** (1975) 752.

17. B. G. Deboer, A. Sakthivel, J. R. Cagle and R. A. Young, *Acta. Crystallographica, Section B,* **47** (1991) 683.

18. J. G. Rabatin, G. R. Gillooly and J. W. Hunter, *Journal of the Electrochemical Society,* **114** (1967) 956.

19. S. Naray-Szabo, *Zeitschrift feur Kristallographie,* **75** (1930) 387.

Section IV.

Chemical-Shift Selective Multiple Quantum NMR as a Probe of

Dopants in Calcium Fluorapatite

1. Introduction

Multiple-quantum NMR has been used previously to count the number of spins in clusters of spins in tightly dipolar-coulped systems.[1-4] Spin counting is done by creating multiple-quantum coherences among sets of spins in a sample and observing the relative magnitudes of the coherences. The coherence order profile can be related to the number of coupled spins in a cluster by the statistical model developed Pines and coworkers.[5] This technique has been used to count clusters of spin in several systems including the number of protons on a single molecule[6] and the number of protons in the silica lattice.[5] Gleason and Scruggs[7] have extended this technique to study the relative fraction of fluorine spins that are randomly dispersed in polymers mixes versus the amount in agglomerated salts. Furthermore, Cho and Yesinowski have fit the coherence orders of the MQ-NMR spectra of distributions of spin cluster sizes in apatitic mineral phases to probe the nonrandomness of dopants and vacancies in the lattice.[8]

In this section (IV) we will examine distributions of clusters of ^{19}F spins in families of crystal orientations in doped, polycrystalline fluorapatite using chemical-shift-selective MQ-NMR. Chemical shift selective MQ-NMR is a technique designed to obtain the MQ spectrum of the spins giving rise to a single peak in a chemical shielding powder pattern. The reason chemical shift selection must be used on fluorapatite is because the total width of the powder pattern is to large for the PI-MQ sequence to effectively create coherences in the entire powder pattern. Chemical-shift-selection is achieved by burning away all but a single peak in the chemical shielding powder pattern with a series of weak stepped-frequency rf pulses. The PI-MQ portion of the sequence is then performed with the rf frequency on resonance

with the single remaining peak. We have employed this technique on two doped calcium fluorapatite samples to look for evidence of clustering of spins.

The first system is a calcium flourapatite sample with one in every ten calcium ions replaced by a strontium ion. The strontium ions have the effect of changing the chemical shielding tensors of approximately one third of the ^{19}F spins in the apatite lattice.[9] Anisotropic shielding tensors can be represented geometrically by ellipsoids; the distance between the origin and a point on the surface is related to the chemical shift.[10] The ^{19}F spins in the strontium doped system can be represented by the schematic diagram in Figure IV-1. Figure IV-1a shows a single column of four unperturbed fluorapatite spins bounded by strontium perturbed spins and Figure IV-1b shows a collection of columns of unperturbed spins punctuated by perturbed spins. When the PI-MQ sequence is used to record the MQ spectrum of unperturbed spins pictured in Figure IV-1, coherence growth is stopped at the perturbed spins because they are to far off resonance (see discussion section below). Therefore, magnitude of the coherence orders in the multiple quantum spectrum will reflect coherences that were created among linear cluster of like spins. In this study we have analyzed the coherence orders in terms of a linear cluster model [9] to compute the mean distance over which the tensors of like spins remain the same. We have deemed this distance the "correlation length" of the tensor.

Two criteria were used to determine which peak in the powder pattern was observed using chemical-shift-selective MQ-NMR experiments. First, a peak was chosen that corresponded to a family of orientations of crystallites where the chemical shifts of the unperturbed spins were most different from those perturbed by strontium ions. The large chemical shift difference ensures that the perturbed spins have resonance offsets large enough so that they cannot enter MQ coherences with the unperturbed spins.
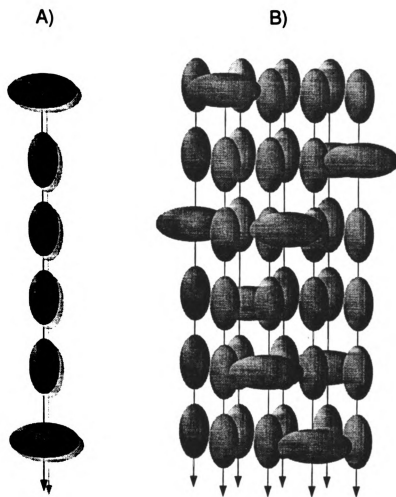
Figure IV-1. Schematic diagram of the fluorine spin tensors in strontium doped

fluorapatite; a) a one-dimensional arrangement , b) three dimensional array.

The second criteria is that the peak should be of great enough intensity to allow for detection. A detailed analysis [9] of the MAS-NMR spectra of this compound yielded the principle components of the shielding tensor of the strontium perturbed fluoride spin of 136.1, 57.3, and 43.7 ppm, compared to the values of 120, 36, and 36 ppm for the unperturbed sample. Chemical shielding powder pattern simulations corresponding to these two sets of tensor components are given in Figure IV-2.

To identify the peak in the pattern where the pertubred and unperturbed spins have the largest chemical shift differences, the chemical shift difference between the two types of spins can be calculated for all crystal orientation. The difference in the chemical shift $\Delta\sigma$ as a function of the crystallite orientation is given by the formula

$$\Delta\sigma = \sigma_{unpert}(\theta,\phi) - \sigma_{pert}(\theta,\phi)$$
$$= -\{\overline{\sigma} + \sigma_0[(3\cos^2\theta - 1) + \eta\sin^2\theta\cos2\phi]\}_{unpert} \qquad \text{IV-1)}$$
$$+ \{\overline{\sigma} + \sigma_0[(3\cos^2\theta - 1) + \eta\sin^2\theta\cos2\phi]\}_{pert}$$

where θ and ϕ are the usual spherical coordinates and $\overline{\sigma}$ and σ_0 are the isotropic chemical shift and the characteristic chemical shift anisotropy respectively. Values for $\Delta\sigma$ are plotted as a function θ and ϕ in Figure IV-3. Figure IV-3 also contains a schematic drawing of the chemical shielding powder pattern of the unperturbed fluorapatite spins to show which peaks in the pattern have the highest intensity as a function of θ. Although $\Delta\sigma$ averaged over ϕ has the largest value at $\theta = 0°$ ($\Delta\sigma = 16.1$ ppm) this is the least intense portion of the powder pattern. Since the intensity of the powder pattern at $\theta = 90°$ is the greatest the chemical shift selective MQ-NMR experiment was performed on the spins in the crystallites at this orientation.

The second system on which the chemical-shift-selective MQ-NMR pulse sequence was used to gain clustering information was a fluorapatite sample doped with antimony. This compound is a phosphor and ,like several other metal-doped
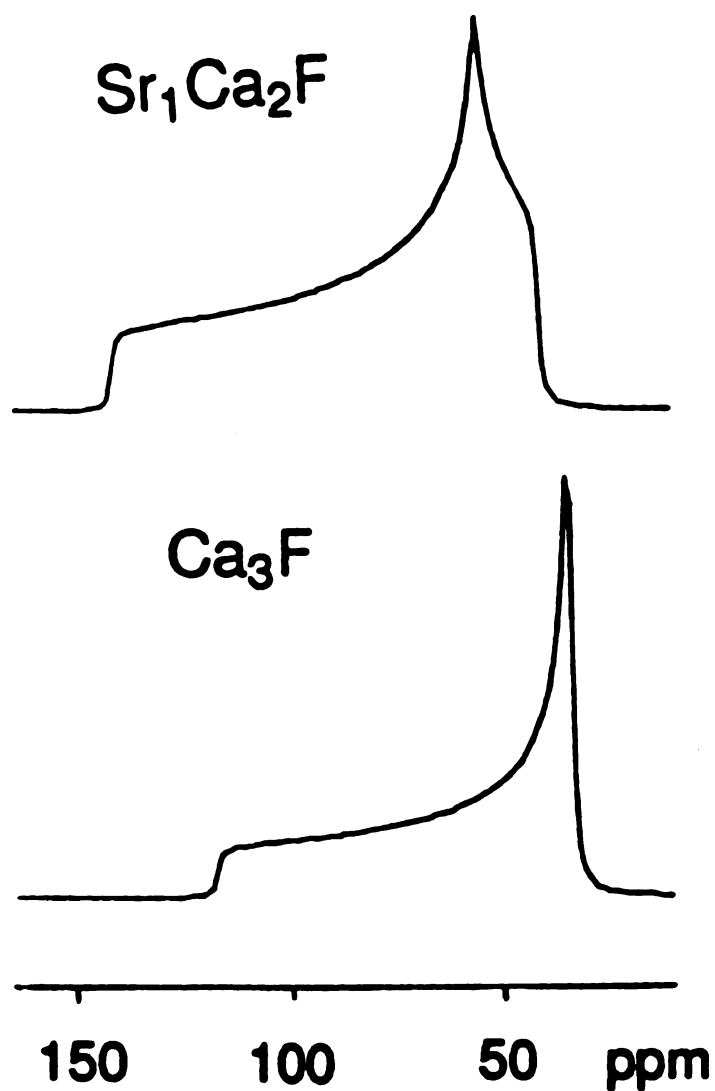
Figure IV-2. Calculated chemical shielding powder patterns for the two main types of fluorine environments found in strontium doped calcium fluorapatite. An exponential function corresponding to a line broadening of 500 Hz was applied to the calculated FID before transformation.

Figure IV-3. Plot of the difference in chemical shift Δσ of the two main types of

fluorine environments (shown in Figure IV-2.) as a function of the spherical

coordinates angles φ and θ .

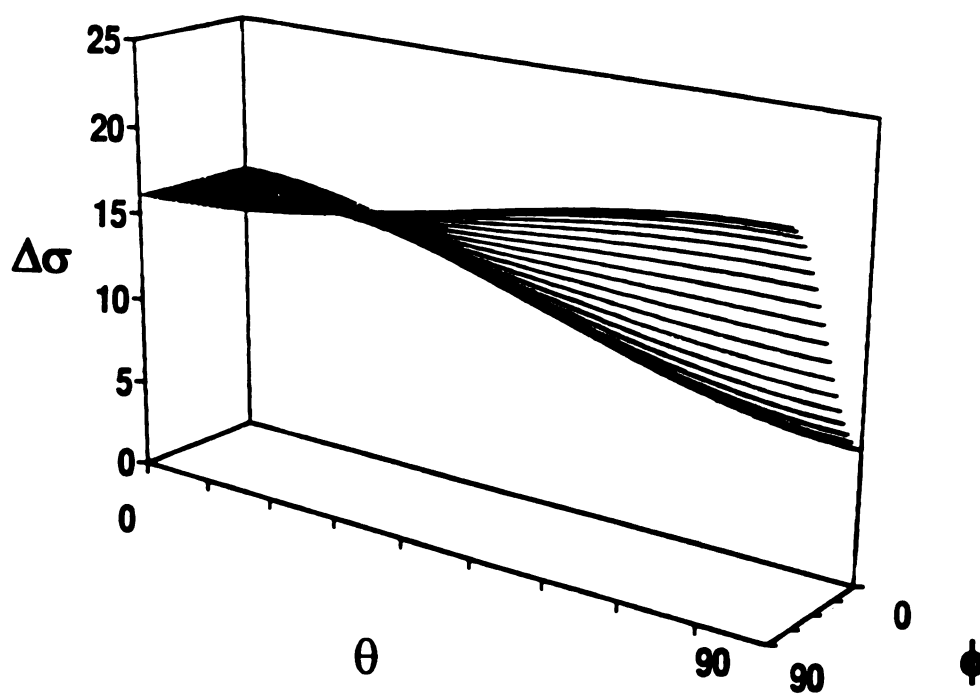fluorapatite compounds, is used in commercial fluorescent lamps. Antimony is believed to be responsible for giving this material its phosphor qualities, that is, the ability to adsorb uv photons and emit in the visible region of the spectrum. It has also been proposed that the phosphor properties in this materials arise from a series of photo centers which are simply fluoride vacancies present in the apatite lattice which compensate for the -2 charge missing when antimonate group (SbO_4^{3-}) replaces a phosphate group (PO_4^{-3}) in the lattice.[11] It has also been proposed that the charge compensation is achieved by simply removing an oxygen atom from the antimonate group as the means of charge compensation instead of two fluorides.[11] Chemical shift selective multiple quantum NMR is well suited answer the question as to whether fluoride vacancies are present in the lattice on a level similar to the antimony(III). If such vacancies were present, they would slow the MQ growth dynamics. The multiple-quantum NMR result we present does not indicate that defects are present strengthening our original conclusion that an SbO_3^{-3} group replace a phosphate group, with the lack of the oxide ligand responsible for charge compensation.

2. Experimental

The ^{19}F NMR experiments were carried out on a Varian VXR-400S spectrometer equipped with a 100 watt fluorine amplifier (376 MHz) and a high-power probe with a 5 mm o. d. solenoid coil. The $\pi/2$ pulse length for the high power portion of the experiment was measured before each experiment, and was typically 3.7 μs. The phase incremented multiple-quantum portion of the sequence has been used previously[12] with the t_1 value fixed at 2 μs and the cycle time at 70.8 μs. Twenty-four saturation pulses with $\gamma B_1 = 330$ Hz and separated by 0.5 ms were applied to the powder pattern so as to saturate the magnetization of all but the upfield edge in the following manner: the frequency offsets of these saturation pulses from the upfield edge were, in order of application 25, 24, 23,22, ..., 6 KHz ,

with five saturation pulses repeated at only the last offset. The spin-lattice relaxation time T_1 of the calcium fluorapatite sample was measured to be 91 s, and that of the calcium/strontium fluorapatite is 85s; such long, nearly-equal, values argue against the presence of motions of the type mentioned above, which would have to occur on the time scale of hundreds of microseconds. Because of these long spin-lattice relaxation times, it was useful to employ short relaxation delays 0.6 T_1 and four sets of "dummy scans" (i.e. repetitions of the sequence without data acquisition), a strategy widely used in 2-D solution NMR experiments. The full 2-D version of the experiment, used to obtain a frequency slice in the f_2 dimension for comparison with the chemical-shift selective experiment, involved 256 complex points in the phase-incremented domain, and sampling 256 complex points in the t_2 domain (a 2 ms delay after the mixing sequence was followed by a $(\pi/2)_x$ pulse, 100 μs spin lock (y) pulse, a Hahn echo sequence with a $(\pi)_x$ pulse between two 35 μs delays, and then detection). The psuedo 1-D chemical-shift-selective experiment involved collecting 64 complex points in the phase-incremented domain, with each complex point in the t_2 domain (obtained as immediately above, but without the Hahn echo sequence) resulting from integrating the FID (summing the first 50 points using a 10 μs dwell time). In order to characterize the width of the MQ excitation profile, and to enable comparison with other reported MQ studies, we obtain the effective size N by least-squares fitting of the equally-weighted orders of coherence (up to n=12 at longer preparation times) to a Gausssian function.

STEPPED- FREQUENCY
SATURATION PULSES

PI-MQ SEQUENCE
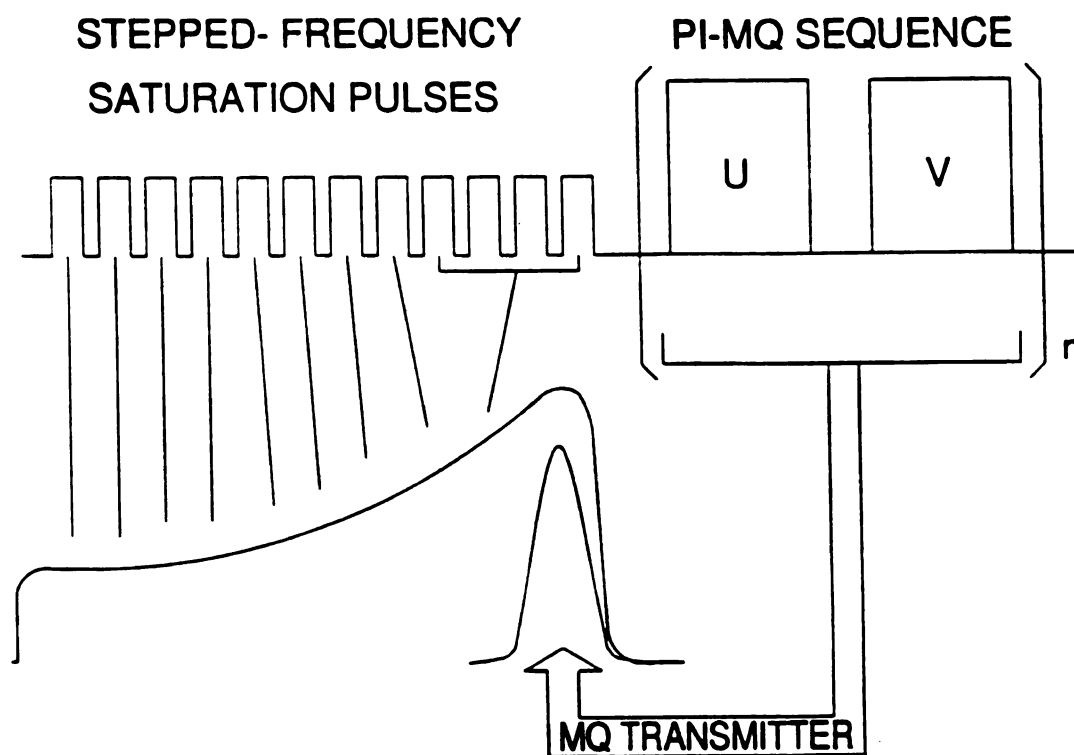
U   V

n

MQ TRANSMITTER

Figure IV-4. Pulse sequence for chemical-shift-selective phase-incremented multiple-quantum NMR (see text for details). The periods labeled "U" and "V" refer to the phase-incremented eight-pulse double-quantum selective MQ preparation period and the "time-reversal" portion of the MQ sequence, respectively. The γB_1 of the frequency-stepped saturation pulses is weak compared to the "hard 90 " pulse in the PI-MQ portion of the sequence, and is in the present case less than the local fields.

3. Results and Discussion

3.1. Chemical Shift Selection

The basic concept behind the chemical shift selective MQ- NMR experiment is to saturate all of the magnetization in a powder pattern with the exception of a specific homogeneously broadened peak and perform the MQ experiment on the remaining peak. When the homogeneous broadenings of the peak within a powder pattern are small compared to the total width of the pattern, strategies such as DANTE[13] and SELDOM[14] have proven useful for selection a specific peak in the powder pattern. The relatively broad homogeneous linewidths of fluorapatite severely limit these schemes as an effective means of suppressing off resonance magnetization. For this reason we have chosen soft pulses applied to the powder pattern to selectively eliminate all but the desired peak followed by a standard multiple quantum detection scheme as shown in Figure IV-4.

To determine the most efficient way of placing the saturation pulses to minimize magnetization from of resonance peaks, we computed the time development of magnetization under the influence of saturation pulses using saturation theory of solids.[15] Furthermore, we have obtained experimental data on saturation of a single crystal of fluorapatite using weak rf pulses. Provotorov[15] has derived an expression for the time development of magnetization under the influence of prolonged, weak rf fields applied to tightly coupled solids. This expression takes the form:

$$M_z = \frac{M_0}{h_0^2 + H_L^2}\left[h_0^2 + H_L^2 \exp\left(-\pi\gamma^2 H_1^2 \frac{h_0^2 + H_L^2}{H_L^2} g(\omega)t\right)\right]. \qquad \text{IV-1)}$$

The terms in this Eqn IV-1 include H_L the local field which is equal to $\sqrt{1/3}$ the root second moment; H_1 the amplitude of the applied high frequency field; h_0, the

difference in frequency between the frequency of an applied rf filed and the resonant frequency γH_0 ; γ, the magnetogyric ratio, and $g(\omega)$; the normalized lineshape function. Equation IV-1 is valid under the condition that the rf fields are "week" or applied $H_1{}^2 << H_L{}^2$. Furthermore, saturation must be achieved rapidly compare to the longitudinal relaxation time T_1 of the system. This condition can be describe by the following inequality:

$$\pi\gamma^2 H_1^2 \frac{h_0^2 + H_L^2}{H_L^2} g(\omega)T_1 >> 1 .$$

IV-2)

Although the lineshape function of in fluorapatite is triplet[16], we have used the normalize Gaussian to approximate the lineshape of fluorapatite which is given by the formula:

$$g(\omega) = \frac{1}{H_L\sqrt{2\pi}} \exp\left(\frac{-h_0^2}{2H_L^2}\right).$$

IV-3)

The terms in Eqn. IV-3 are the same as those in Eqn. IV-1.

Eqn IV-1 has been used to compute the selectivity attainable using soft pulse on the fluorapatite powder pattern when a saturation pulse is applied 6.0 kHz down field (at 20.4 ppm) of the left edge of the pattern. The results of this computation are shown in Figure IV-5 which is a plot of the remaining z-magnetization after 4 millisecond saturation pulses. The highest trace is the magnetization remaining after a single pulse and each lower trace corresponds to increasing numbers of saturation pulses. After a single saturation pulse the remaining magnetization profile is about 4 kHz which is approximately equal to 9 degrees of variance in azimuthal angle θ of the crystallites orientation. After six saturation pulses, the half-height linewidth of the magnetization profile is 1500 hz corresponding to a the variance in θ of 3 degrees.

The time development of the z-magnetation for the same upfield portion of the fluorapatite powder pattern shown in Figure IV-5 is given in Figure IV-6;

however, the length of the saturation pulses is varied from 4 to 80 ms instead of the number of pulses (as in Figure IV-5). The highest trace in Figure IV-6 corresponds to the magnetization profile after a 4 ms saturation pulse and the lower traces correspond to longer saturation pulses. One notable feature of this plot is the selectivity of the magnetization profile increase with increasing pulse width, but the desirable magnetization (at 36 ppm) is decreased concomitantly. The experimental parameters for removing unwanted magnetization from the powder pattern such as the number of saturation pulses, pulse widths, and offsets must be chosen to minimize off-resonant magnetization and preserve enough magnetization in the peak on which the multiple quantum experiment will be performed.

To test the accuracy of the theory of saturation of solids (Eqn. IV-1) at predicting the saturation behavior of fluorapatite, two saturation experiments were performed on a single crystal of fluorapatite oriented at $\theta = 90°$. The first experiment involved applying saturation pulses on resonance to the single crystal of fluorapatite with pulse width ranging from 4 to 80 ms. Figure IV-7 contains the results of this experiment and the computed values predicted by the saturation theory (Eqn IV-1). The experimental points in Figure IV-7 are less then the computed values for short pulse width, but begin to converge for longer saturation pulses.

The second saturation experiment was performed to test the ability of Eqn. IV-1 to predict saturation behavior when rf irraditation is applied off resonance. Figure IV-8 is a plot of the normalized values of z-magnetization obtained experimentally and the values calculated using Eqn. IV-1. The experimental points are lower than the calculated points for all regions of this plot with the greatest difference occurring when the pulses are on resonance. Although the values for z-magnetization predicted by Eqn. IV-1 were qualitatively similar to the experimental values show in Figures IV-7 and IV-8, the quantitative agreement is poor. Since
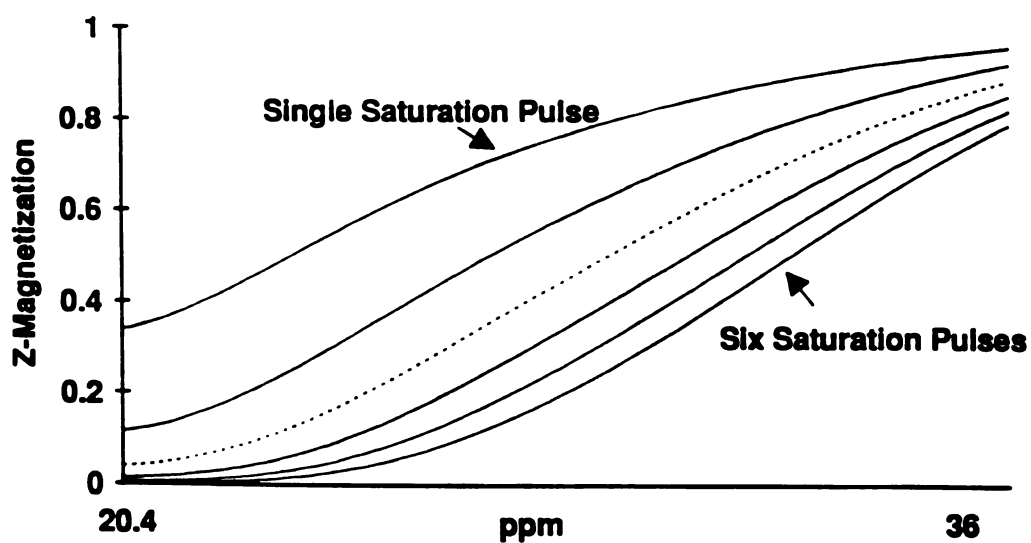
Figure IV-5. Plot of the longitudinal magnetization M_z as a function of resonance

offset for crystallites in the upfield portion of the fluorapatite powder pattern

calculated using the Provotorov [1] theory of saturation of solids by weak pulses.

The plot represents that remaining z-magnetization left in the fluorapatite powder

pattern between $\sigma_\perp$ (36 ppm) and 6 kHz down field (20.4 ppm) after the application

of various numbers of saturation pulses (γH_1 = 300 Hz) at 20.4 ppm.
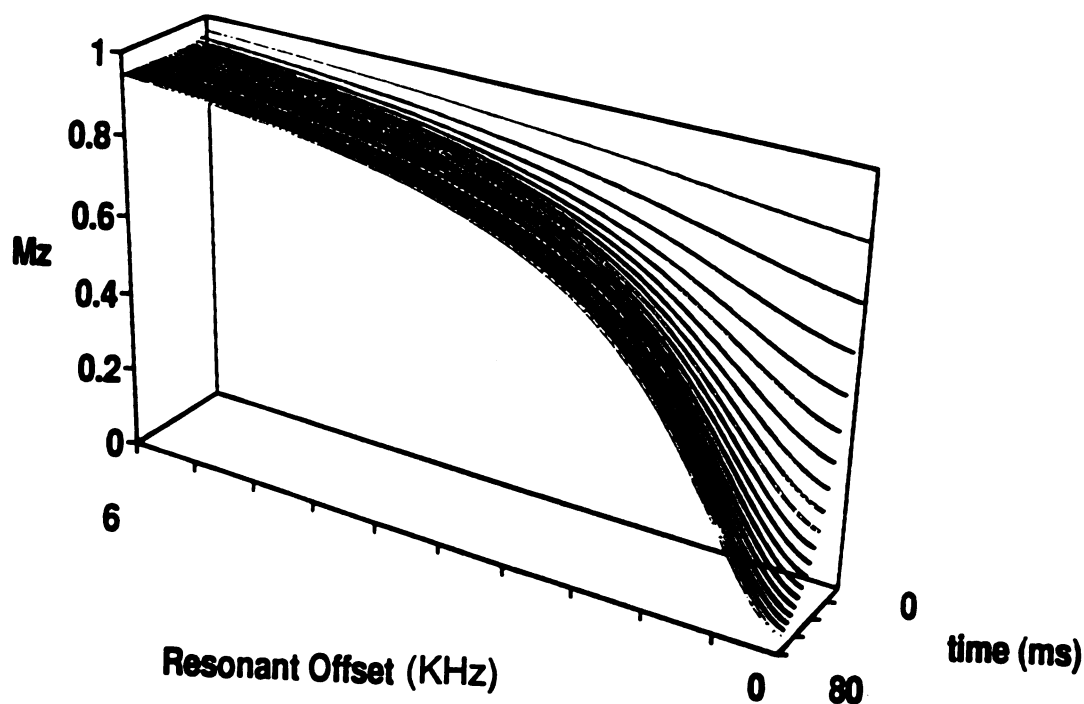
Figure IV-6. Plot of the longitudinal magnetization M_z as a function of resonance offset for crystallites in the upfield portion of the fluorapatite powder pattern calculated using the Provotorov [15] theory of saturation of solids by weak pulses. The plot represents that remaining z-magnetization in the same portion of the fluorapatite powder pattern; however, the traces correspond to different pulse width of a single saturation pulse (γH_1 = 300 Hz).
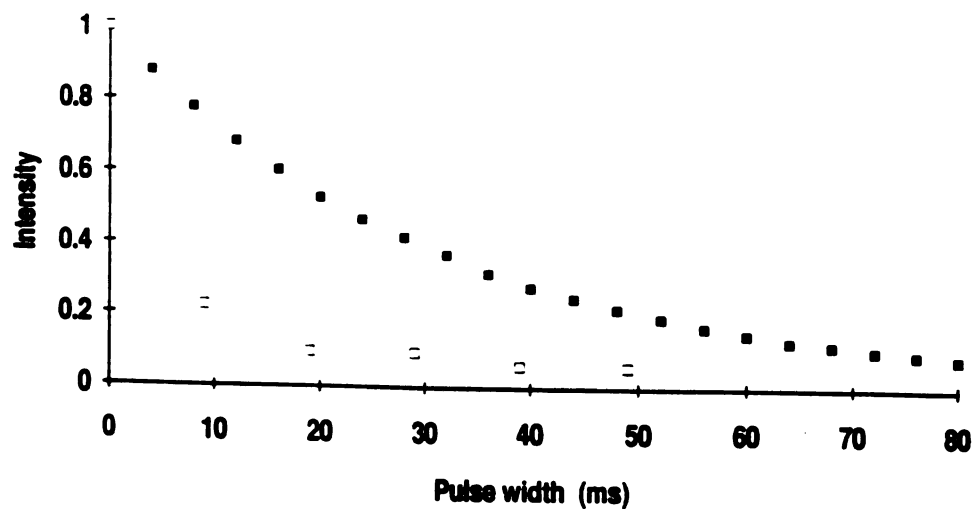
Figure IV-7. Plot of calculated (■) and experimental (□) z-magnetization as a function of time that a single saturation pulse (γH_1 = 330 Hz) is applied to a crystal of fluorapatite oriented at (θ = 90°).
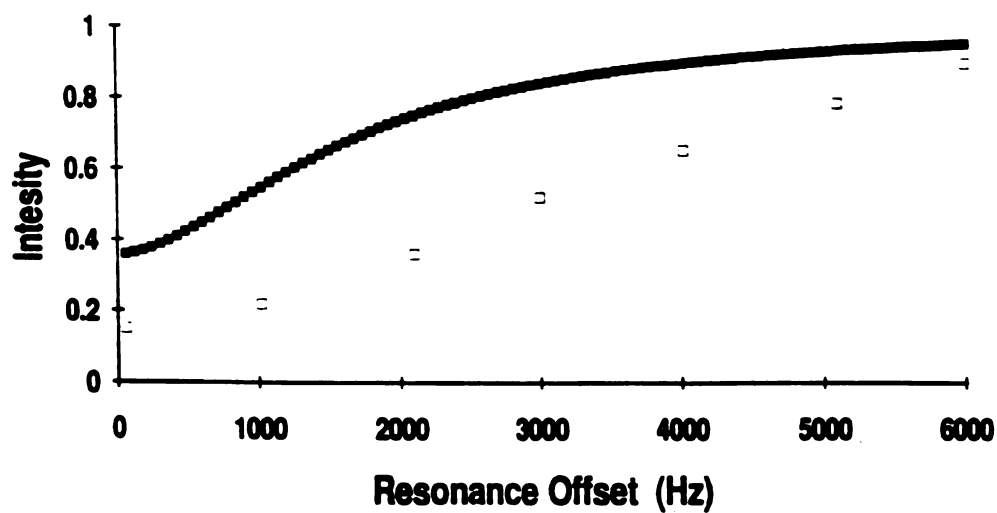
Figure IV-8. Plot of calculated (■) and experimental (□) z-magnetization as a function of resonance offset when a single saturation pulse (30 ms, γH_1 = 330 Hz) is applied to a crystal of fluorapatite oriented at $\theta = 90°$.

these plots show a lack of quantitative agreement between theory and experiment the conditions for the saturation scheme such as pulse widths, offsets, and repetitions were based solely on experimental observations.

The lack of agreement between the experimental and computed z-magnetization values shown in Figures IV-7 and IV-8 may arise in part from the from inappropriate lineshape functions ($g(\omega)$) in Eqn. IV-1. As previously mentioned, the a Gaussian function was used to approximate the line shape function of fluorapatite, whereas the actual lineshape function a fluorapatite crystal oriented at $\theta = 90°$ is a triplet structure.[16] If the true lineshape function is used the difference between experimental and computed points furthest from resonance shown in Figure IV-7 becomes less.

3.2. Discussion of the Sr/Ca Fluorapatite MQ NMR results

The results of the chemical shift selective PI-MQ NMR experiment with the transmitter place at the up field edge of the powder pattern (36 ppm) are given in Figure IV-9. Figure IV-9 is a bar graph showing the magnitude of each coherence orders normalized to the double quantum coherence as a function of preparation time for the pure and strontium doped fluorapatite samples. The magnitudes of higher coherences orders are larger for the pure fluorapatite as compared to those for the strontium doped fluorapatite. This clearly demonstrates that the growth of multiple quantum coherences are slowed by the presence of the strontium-perturbed fluorine spins.

The coherence orders in Figure IV-9 can be fit to a Gaussian function to obtain the effective size n at each preparation time. A plot of the effective size values versus preparation time is given in Figure IV-10. There is a monotonic increase in the effective size in the data for each sample with the exception of one of the points in the strontium doped sample which deviates from the upward rise by

an amount within experimental error. At all preparation times the effective size of the doped sample is less than those for stoichiometric fluorapatite and the difference between the two data sets increases with preparation time. This indicates that the coherence growth is being limited, presumably by the presence fluorine spins perturbed by strontium atoms.

Our interpretation of the relatively slow growth dynamics observed in the strontium doped sample involves viewing the spin system as clusters of like spins bounded by perturbed spins which cannot enter multiple-quantum coherence. Although the PI-MQ-NMR scheme employed is designed to create a double-quantum selective Hamiltonian to first order[12], even for spin systems involving spins with different chemical shifts, it fails when these shifts become to large. At the orientation which was selected (θ = 90 degrees) the chemical shift difference $\Delta\sigma$ (depending on ϕ) between unperturbed fluorine spins and strontium perturbed spins varied from 8 ppm to 21 ppm (see Figure IV-3). To demonstrate how shift differences of ca. 20 ppm block coherences, we have computed the time development of the triple-quantum coherence for linear arrays of four spins separated by 3.44 Angstroms (as in fluorapatite) with chemically shifted spins. The results of this computation are given in Figure IV-11. Figure IV-11a is a plot of the triple quantum coherence as a function preparation time for a system of four like spins and a system with one of the middle spins shifted by 10 ppm. Each of the two traces show a rise to approximately the same level and have deep oscillations; however, there is a substantial difference in the values after approximately 200 μs. Figure IV-11b contains the calculated triple quantum-coherence for a linear array of four spins with one of the middle spins shift by 50 ppm in addition to the triple quantum coherence for a set of spins with equivalent shifts. On the time scale shown the trace corresponding to the cluster of like spins rises quickly and oscillates about a values of approximately 6×10^{-4}. The trace corresponding to a
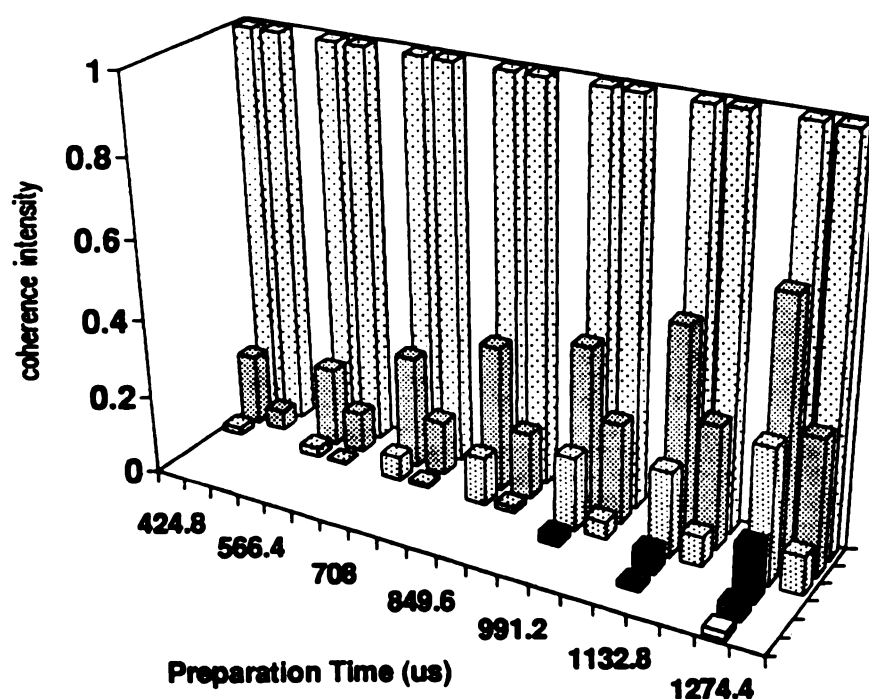
Figure IV-9. Plot of the multiple-quantum coherence orders as a function of preparation time for stoichiometric fluorapatite and strontium doped fluorapatite. The upfield edge of the pattern 36 ppm was "selected" corresponding to crystallites θ = 90°. All coherence orders are normalized to the 2-quantum intensities.
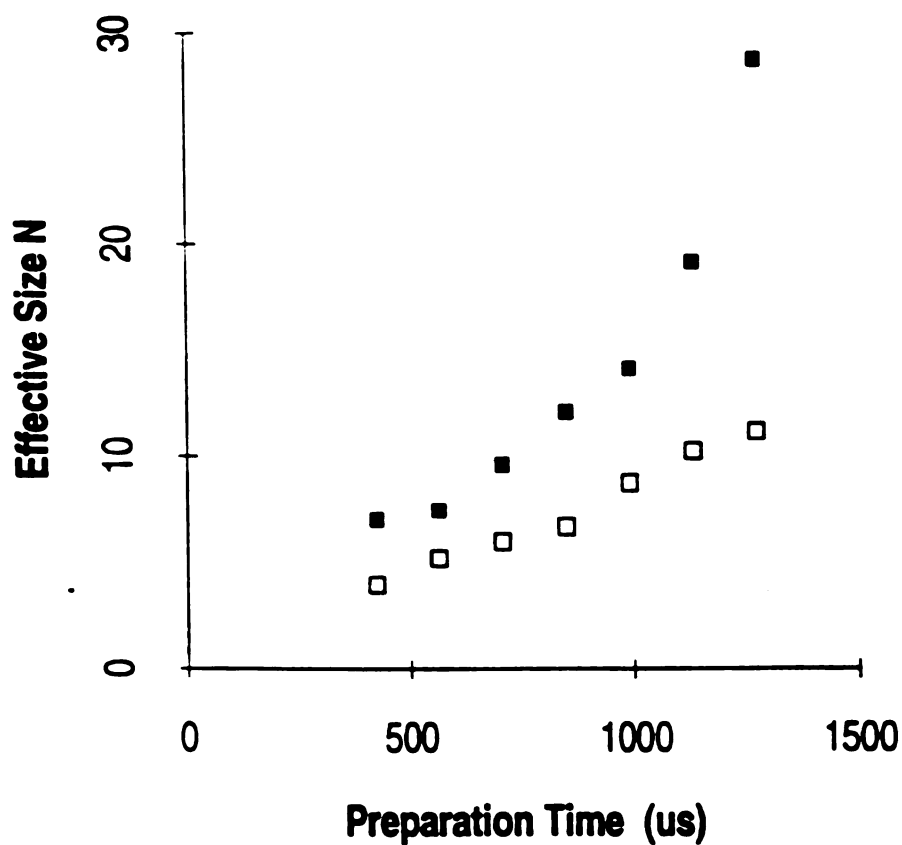
Figure IV-10. Plot of effective size n (obtained from the coherence order in Figure IV-9.) vs. multiple-quantum preparation time. Results from the two samples are shown, calcium fluorapatite (■) and 9/1 calcium/strontium solids solution (□). Experimental errors, including both reproducibility as well as fitting errors, are less than 1.5X the width of the squares.
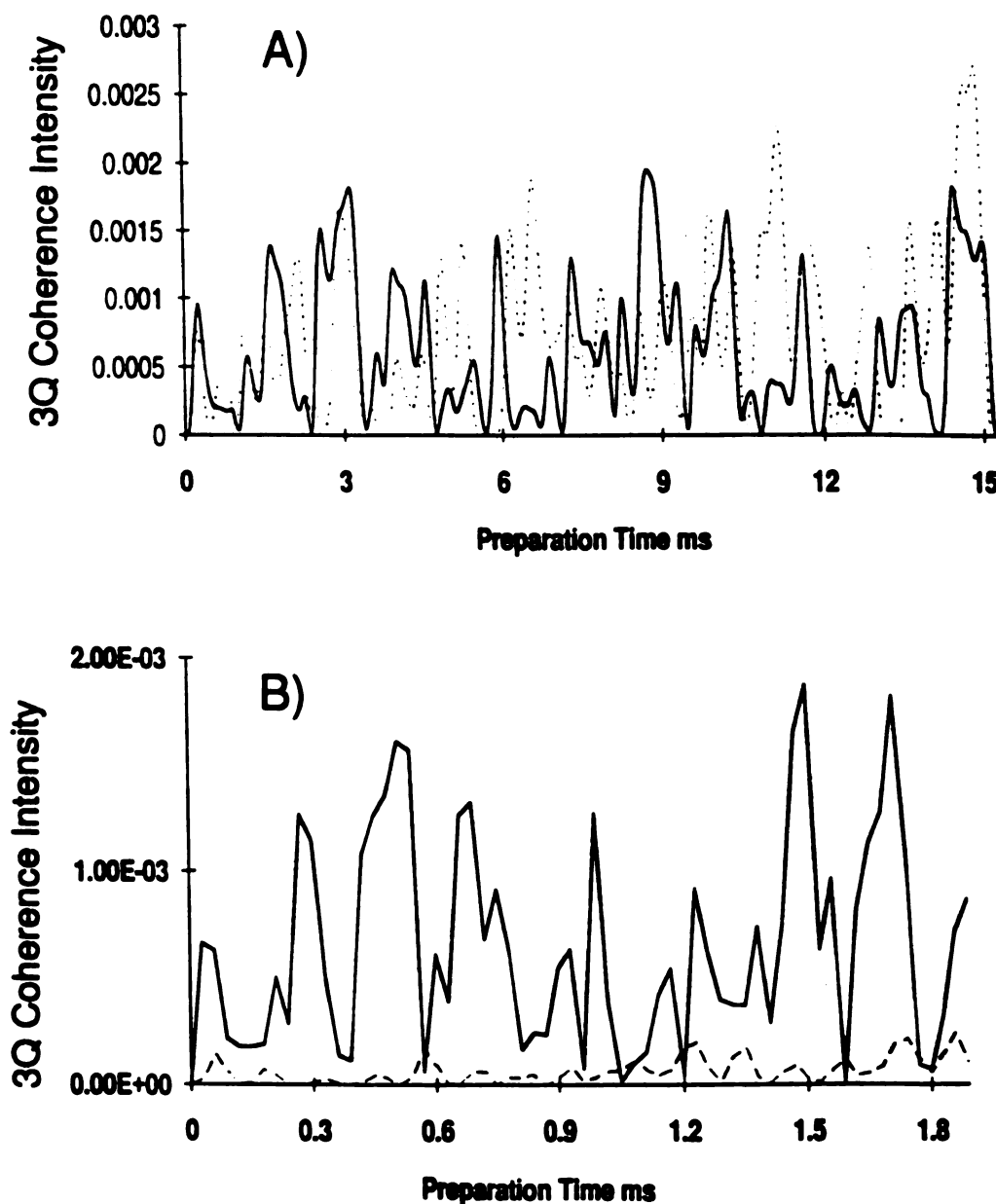
Figure IV-11. ANTIOPE simulation of the triple-quantum intensity as a function of multiple quantum preparation time for the double quantum selective PI -MQ NMR pulse sequence. The spin system is a linear cluster of 4 fluorine spins separated by 3.44 angstroms initially in the I_x state. 11a) trace corresponding to four spins with equivalent shifts (solid line) and trace corresponding to four spins with a single middle spins shifted by 10 ppm. 11b) trace corresponding to four spins with equivalent shifts (solid line) and trace corresponding to four spins with a single middle spins shifted by 50 ppm.

cluster with a chemically shifted spin only rises to oscillate about a level of approximately 1×10^{-4} and does so near the end of the preparation time shown. Figure IV-11 demonstrates that higher coherence orders do not develop in the same manner in spin clusters with equivalent shifts as compared to those containing shifted spins. Furthermore, higher coherence are severely limited when the chemical shift perurbations are only several times greater than the homonuclear couplings. This ability of shifted spins to block growth of higher coherence is what we attribute the slow growth dynamics shown in Figure IV-9 and IV-10. That is, fluorines spins perturbed by strontium ions in the strontium-doped sample create boundaries that block coherence growth and the observed coherences (in Figure IV-9) simply reflect the growth dynamics among clusters of like spins.

We have tested the assumption that the growth dynamics for the strontium doped sample can be modeled as a distribution of clusters of like spins created by the random placement of perturbed spins. The basic scheme to extract information about the size of linear clusters from MQ coherence orders was first proposed by Cho and Yesinowski.[8] This model predicts that the observed coherence orders are the sum of the contributions of the coherence order magnitudes expected for each cluster weighted by the mole fraction of spins in cluster of a specific size. A comparison of the values of the ratio of the 4-quantum intensity to 2-quantum intensity predicted by the linear cluster model and the experimental values of this ratio is given in Figure IV-12. The agreement between the cluster model and the observed values for the strontium doped sample implies that the MQ-NMR dynamics of the strontium doped spins system can be simply viewed as clusters bounded by perturbed spins.

Since this technique has allowed us to gain information about the distance over which the tensors of unperturbed spins remain the same, it should be capable of yielding similar information on other spin systems. We have previously defined a

correlation length for spins with like tensors as the distance between the outermost spins in a cluster of like spins. The average (mean) run length of the cluster of unpertubed spins in this sample was 3.5 giving a correlation length of 12 angstroms.

3.3. Antimony Doped Fluorapatite

In this section the chemical shift selective MQ-NMR technique is used on a practical problem; the search for fluoride vacancies in antimony-doped fluorapatite which are thought to give this material its phosphor qualities. As in the strontium doped system the chemical-shift-selective PI MQ-NMR experiment was set up to record the MQ spectrum of the upfield edge of the pattern (crystals with the orientation at $\theta = 90°$). The profile of the coherence orders (not shown) matched that of the stoichiemtric fluorapatite within experimental error. Specifically, the 4-quantum peaks were 0.32(Sb doped apatite)and 0.330 (pure fluorapatite) the height of the 2-quantum peaks at a preparation time of 991 μs. The experimental error on the 4Q:2Q intensity rations is about 0.03. Furthermore, the linear cluster model predicts that if fluoride vacancies were present at the level of antimony in the lattice (13.6 mole %) the 4-quantum peaks would be only 0.22 as large as the 2-quantum peaks. Since the normalized 4-quantum intensity in the antimony doped sample is within experimental error of the value for stoichiometric fluorapatite we conclude that there are no fluoride vacancies in the lattice. This strengthens the previously proposed scheme of charge compensation for the antimonate ion whereby SbO_3^{-3} replaces a PO_4^{-3} proposed in section II.
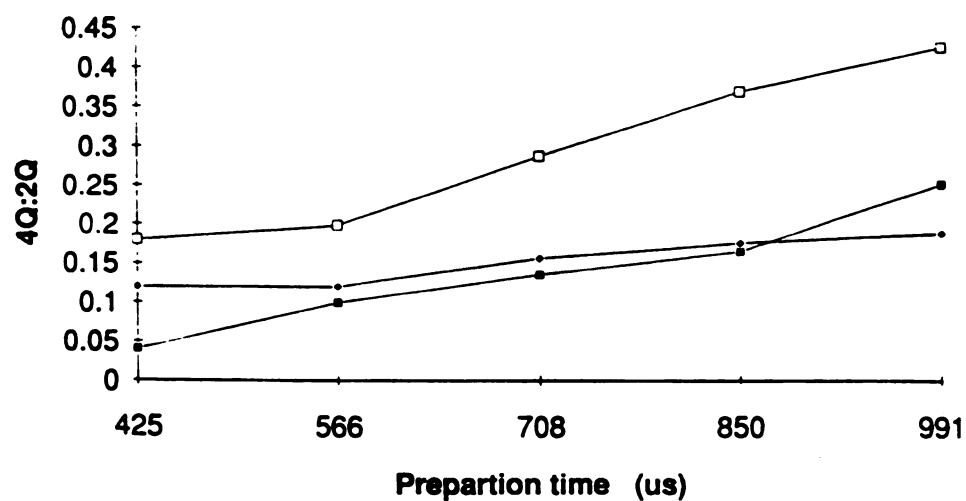
Figure IV-12. Plot of the 4-quantum:2-quantum vs. preparation time for stiochiometric fluorapatite (□) and strontium-doped fluorapatite (◆). The solids squares (■) represent the values calculated using the linear cluster model (see text).

4. Conclusion.

The result of doing chemical shift selective MQ-NMR experiment on fluorapatite systems succeeded in gaining orientation specific MQ-NMR data of a specific class of crystallite orientations. In the strontium doped sample we were able to show that spins with large enough shift perturbations could effective block coherence growth much the same way a vacancy would. The multiple quantum dynamics in this sample reflect coherence growth among clusters of spins with the same chemical shift bounded by strontium-perturbed spins with different shielding tensors. Using this technique to obtain correlation lengths in other types of systems could yield useful information such as the curvature or tacticity of polymers. Finally, this technique was able to clearly show that fluoride vacancies are not responsible for charge compensation in antimony doped fluorapatite. The implication of this finding is that antimony alone is responsible for giving this material its phosphor qualities.

Section V.

Chemical-Shift Selective Multiple Quantum NMR of Fluorapatite: Study of the Effect of Dimensionality on MQ Dynamics

1. Introduction

In section IV the chemical shift selective multiple-quantum NMR technique was use to obtain clustering information about clusters that were present in fluorapatite samples. To expedite data collection, the peak in the powder pattern at the upfield edge was observed since it is the most intense portion of the powder pattern. In this section (V) we will look at other orientations of crystallites by examining different peaks in the powder pattern with the goal learning how the spatial arrangements of spins and the dipolar coupling strength between spins effects growth dynamics. The rate of coherence growth is proportional to the strength of dipolar couplings [1-4]; however, this is difficult to demonstrate experimentally since the couplings between neighboring spins in even simple systems have different dependence upon the crystal orientation. In fluorapatite the dipolar coupling between fluorine spins found in columns have a uniform dependence on the angle between the c axis of the crystal and the applied field. Using the chemical-shift-selective MQ technique to record the MQ spectra of various peaks in the fluorapatite powder pattern we will show that coherence growth among columns of spin is proportional to the dipolar couplings.

The second aspect of growth dynamics examined in this section is the effect of dimensionality of spin arrangements on MQ growth rates. Levy and Gleason have developed a model for the growth dynamics of spin coherences that incorporates spatial information about the arrangements of spins. The Levy-Gleason[18] model predicts that the growth of coherences as a function of preparation time is linear, quadratic and cubic for one, two and three dimensional

arrangements of spins with the absolute rate of growth scale by the diplolar couplings between spins. This prediction has been experimentally verified for coherence growth in two and three dimensional spin arrangements of the protons on the surface of CVD diamond and in calcium hydride.[4] Cho and Yesinowski have shown that effective size growth in the quasi-one-dimensional arrangement of spins in apatites is linear with preparation time; however, the rate three time that predicted by the Levy-Gleason model.[8]

In this section ideas about how to use the chemical-shift-selective MQ NMR technique to study the growth dynamics among planes and columns of spins in fluorapatite are given. The basic idea is to record the MQ growth dynamics of peaks in the fluorapatite powder pattern that correspond to crystallite orientations that would either favor growth among columns of spins or planes of spins in fluorapatite. To illustrate these columns and planes of spins, a schematic arrangement of the fluoride spins in fluorapatite is given in Figure V-1. Each of the spins in the middle columns are surrounded by six nearest neighbors in a plane perpendicular to the columns. We have computed the intra-planar and intra-column dipolar couplings as a function of crystallite orientations (see below) to determine peaks in the powder pattern that would optimally favor one-dimensional or two-dimensional growth coherence growth.
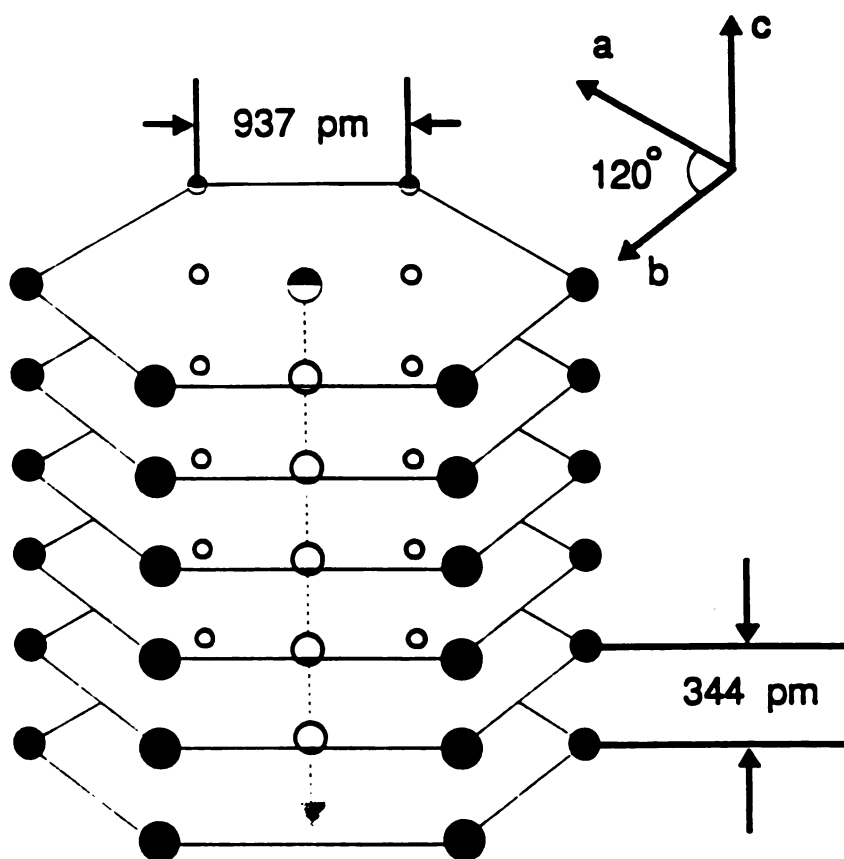
Figure V-1 Schematic arrangements of ^{19}F spins (black solids circles) in calcium fluorapatite.

2 . Experimental

The details of the chemical-shift-selective PI-MQ-NMR experiment are given in section IV-2. The frequencies of the twenty-four saturation pulses were adjusted to remove different portions of powder pattern. One experiment involved removing all of the magnetization except for the peak at 57.4 ppm which corresponds to crystals oriented $\theta=67°$. The offsets of the saturation pulses from the upfield edge were, in order of application 25, 24, 23,.....12, 0, 12, 0, 12 ,0 ,12, 0, 12, and 12 KHz. In a different experiment all of the magnetization except for the peak at the downfield edge of the pattern at 120 ppm which corresponds to crystals oriented $\theta=0°$ was removed. The offsets of the saturation pulses from the downfield edge were, in order of application, 25, 24, 23,22, ..., 6 KHz , with five saturation pulses repeated at only the last offset.

3. Results and Discussion

3.1 Computation of intra-planar and intra-column couplings

In order to determine the crystal orientations that will favor coherence growth in either the planes of spins or the columns of spins in fluorapatite, the dipolar couplings among the spins in both of these types of arrangement must be computed for all crystal orientations. The Levy-Gleason[18] model for the effect of dimensionality upon MQ coherence growth dynamics predicts that the growth rate of coherences is proportional the dipolar couplings between the spins and the number of spins immediately outside a coherent cluster of spins that can enter that coherence. The fact that the number of spins on the periphery of a coherent cluster of spins increases from; chains of spins, to planes of spins, to solid blocks of spins is responsible for the linear, quadratic, and cubic growth of coherences for each of

these arrangements respectively. In the case of fluorapatite each spin in the column has two nearest neighbors and each spin in a plane has six nearest neighbors. These planes and columns of spins are shown clearly in Figure V-2. The relative growth rate of coherences among spins in the planes vs. spins in the columns will be proportional to the dipolar couplings between the spins in these arrangements and the number of nearest neighboring spins.

Expressions for the relative MQ coherence growth rates in the planes and columns of spins can be created by summing the dipolar couplings between each spin pair in these arrangements. These summed dipolar coupling expressions can be written as functions of crystallite orientation by explicitly considering how each of the internuclear vectors transform as a function of crystallite orientation. Furthermore, these expression should only be a function of angle between the c axis of the fluorapatite crystal and the applied field, since this is the orientation that can be "selected" from the powder pattern using the chemical-shift-selective MQ-NMR technique. For clarity in this discussion we will refer the angle between the c axis of the crystal and the applied field as θ_{FAP}. The dipolar coupling between a pair of spins has the form:

$$D(r, \theta) = C\frac{1}{r^3}(1 - 3\cos^2 \theta) \qquad\qquad \text{V-1}$$

where r is the distance between spins, θ is the angle between the internuclear vector and the applied field, and C represents product of several factors (see section I-3.2 for details). Since the value of C is the same for all of the ^{19}F-^{19}F spins pairs we are considering, we only need to consider r and θ in the development of an expression for the dipolar couplings between chains and planes of spins. In order to relate the θ of each spin pair pictured in Figure V-2 to the angle θ_{FAP} we must examine how each of the inter nuclear vectors transforms in the axis
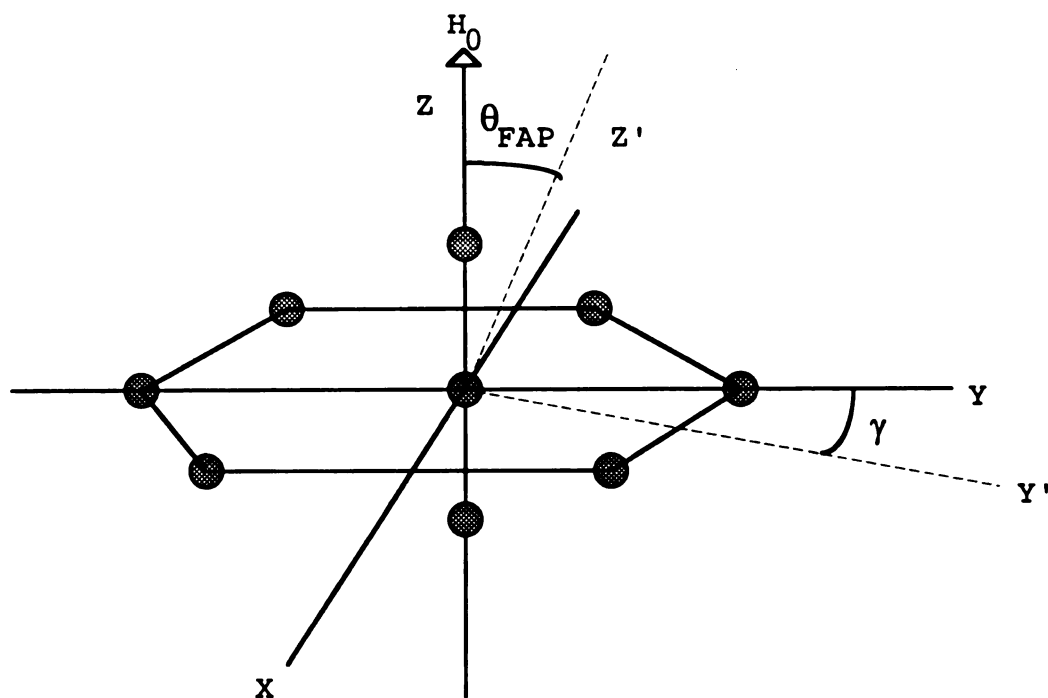
Figure V-2 Schematic diagram of linear and planar arrangements of spins in fluorapatite. The coordinate system relates the molecular frame to the applied field.

system of Figure V-2. This can be done by employing a pair of rotation matrices. The first matrix describes the new coordinates of a vector after the axis system has been rotated about the z axis so that the angle between the original y axis and the new y' is γ as shown in Figure V-2. The second matrix describes the vector after rotation about the y' axis so that the angle between the original z axis and the new z' is θ_{FAP} as shown in Figure V-2. These two matrices R_z and R_y acting on vector $(V_x, V_y, V_z)^T$ and transforming it to a vector V' take the following form:

$$R_Z R_Y \underline{V} = \begin{pmatrix} \cos\gamma & \sin\gamma & 0 \\ -\sin\gamma & \cos\gamma & 0 \\ 0 & 0 & 1 \end{pmatrix} \begin{pmatrix} \cos\theta_{FAP} & 0 & -\sin\theta_{FAP} \\ 0 & 1 & 0 \\ \sin\theta_{FAP} & 0 & \cos\theta_{FAP} \end{pmatrix} \begin{pmatrix} V_X \\ V_Y \\ V_Z \end{pmatrix}$$

$$= \begin{pmatrix} V_X \\ V_Y \\ V_Z \end{pmatrix}'$$

V-3

When the two rotation matrices are multiplied together their product is

$$R_Z R_Y = \begin{pmatrix} \cos\theta_{FAP}\cos\gamma & \cos\theta_{FAP}\sin\gamma & -\sin\theta_{FAP} \\ -\sin\gamma & \cos\gamma & 0 \\ \sin\theta_{FAP}\cos\gamma & \sin\theta_{FAP}\sin\gamma & \cos\theta_{FAP} \end{pmatrix}.$$

V-4

We see from Eqn. V-4 that when a general vector $(V_x, V_y, V_z)^T$ is subjected this double rotation transformation the z component of the new transformed vector is

$$V_Z' = V_x \sin\theta_{FAP}\cos\gamma + V_y \sin\theta_{FAP}\sin\gamma + \cos\theta_{FAP}.$$

V-5

This can be shown by multiplying $(V_x, V_y, V_z)^T$ by $R_z R_y$. By knowing the z component of the rotated vector one can then know the angle between the rotated vector and the applied field since the coordinate system is defined with the applied field vector H_0 coincident with the z axis. The z component of a vector of unit length coincident to the rotated vector V' is equal to the $\cos\theta$ where θ is the angle between the rotated vector and the applied field.

The development of an expression for the dipolar couplings between the linear and planar arrangements of spins picture in Figure V-2 can be completed by installing the vectors that described each of the spins in the axis system into equation V-5. The position of the planar hexagon of spins can be described by the following vectors of unit length: $(0,1,0)^T$, $(0.866, 0.5, 0)^T$, $(0.866, -0.5, 0)^T$, $(0,-1,0)^T$, $(-0.866, 0.5, 0)^T$ $(-0.866, -0.5, 0)^T$. The position of the two spins in the chain of spins above and below the x-y plane can be described by the following vectors of unit length: $(0,1,0)^T$, $(0.866, 0.5, 0)^T$. Since the Vz' component given in Eqn. V-5 is equal to $\cos\theta$, we can simply install the right side of Eqn. V-5 into equation Eqn. V-1 to get an expression for the dipolar coupling as a function of crystallite orientation. For the planar array of spins this expression takes the form:

$$D(2d) = \frac{3}{4} \frac{\gamma^2 h}{r_{\text{inter}}^3} \begin{bmatrix} \left[1 - 3\left(\sin\theta_{FAP}\sin\gamma\right)^2\right] + \\ \left[1 - 3\left(0.866\sin\theta_{FAP}\cos\{\gamma\} + .5\sin\theta_{FAP}\sin\gamma\right)^2\right] + \\ \left[1 - 3\left(0.866\sin\theta_{FAP}\cos\{\gamma\} - 0.5\sin\theta_{FAP}\sin\gamma\right)^2\right] + \\ \left[1 - 3\left(-\sin\theta_{FAP}\sin\gamma\right)^2\right] + \\ \left[1 - 3\left(-0.866\sin\theta_{FAP}\cos\{\gamma\} + 0.5\sin\theta_{FAp}\sin\gamma\right)^2\right] + \\ \left[1 - 3\left(-0.866\sin\theta_{FAP}\cos\{\gamma\} + -0.5\sin\theta_{FAP}\sin\gamma\right)^2\right] \end{bmatrix}$$

V-6

where r_{inter} is the distance between the spin at the origin in Figure V-2 and the spins on the vertices of the hexagon. A similar expression can be derived for the dipolar couplings between the column of spins:

$$D(1d) = \frac{3}{4} \frac{\gamma^2 h}{r_{\text{intra}}^3} \left[2\left[1 - 3\cos^2\theta\right]\right].$$

V-7

With the expressions for the summed dipolar couplings for the linear and planar arrangements of spins in fluorapatite given in Eqn. V-6 and V-7 we can compare the MQ coherence growth rates in either of these two arrangements as a function of crystal orientation. Since only θ_{FAP} can be experimentally controlled (by selecting different peaks in the powder pattern), the expression for the dipolar couplings among spin pairs in the plane (Eqn V-6) is averaged over values of γ at each value of θ_{FAP}. This results in an expression for the intra-planar summed dipolar couplings which is soley a function of θ_{FAP}. Figure V-3 is a plot of the ratio of the summed dipolar couplings between spin pairs in the column to the summed couplings in the plane as a function θ_{FAP}. Regions of the plot where the ratio of the "linear" to the "planar" couplings is large corresponds to orientations that would favor coherence growth among the columns of spins in fluorapatite. When θ_{FAP} is equal to the magic angle (54.7°) the intra-chain couplings are the smallest and planar growth would dominate. The most favorable orientation for linear coherence growth is at $\theta = 0°$.
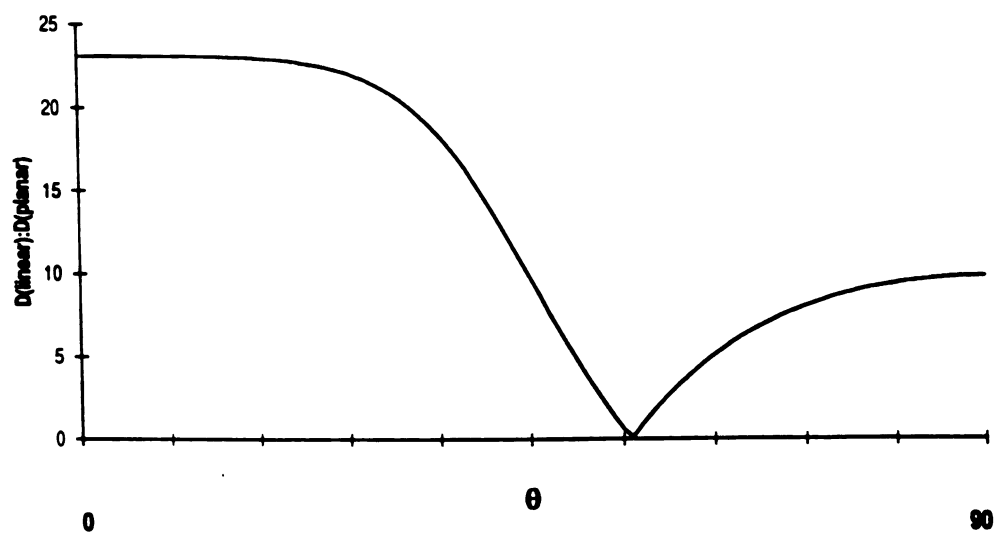
Figure V-3 Plot of the ratio of the summed dipolar couplings of linear spins D(linear) to the summed dipoar couplings of planar spins D(planar) as a funcion of θ.

3.2 Multiple quantum NMR of various orientations

To demonstrate that the growth of MQ coherence does scale as the dipolar coupling between spins the chemical-shift-selective MQ-NMR was used to obtain the MQ growth dynamics of crystals at different orientations. In the first orientation, $\theta = 67.5°$, the strength of the dipolar coupling between the spins in the columns is half of the dipolar coupling at $\theta = 90°$. Figure V-4 is a plot of the effective size as a function of preparation time for crystals oriented at $\theta = 67.5°$ and $\theta = 90°$. The slope of the lower trace over the first 5 points in Figure V-4 corresponding $\theta = 67.5°$ is approximately half that of the upper trace. The points beyond the fifth data point cannot be compared since the MQ growth deviates from linear (toward quadratic) and this region of the plot represents the onset of growth among planes of spins. Figure V-4 supports the prediction that coherence growth is proportional to the coupling between spins.

An attempt was made to record the MQ growth dynamics of crystallites oriented at $\theta = 0°$. At this orientation the dipolar couplings between spins in the chains is strongest relative to the spins in the planar arrangements. The relatively stronger "linear couplings" should have the effect of increasing the linear portion of a plot of the effective size vs. preparation time since growth among the one-dimensional arrays would be favored. Unfortunately the MQ spectra were not able to be recorded. This presumably resulted from the relatively low intensity of the portion of the powder pattern corresponding to orientations at $\theta = 0°$; however the real cause has yet to be determined.
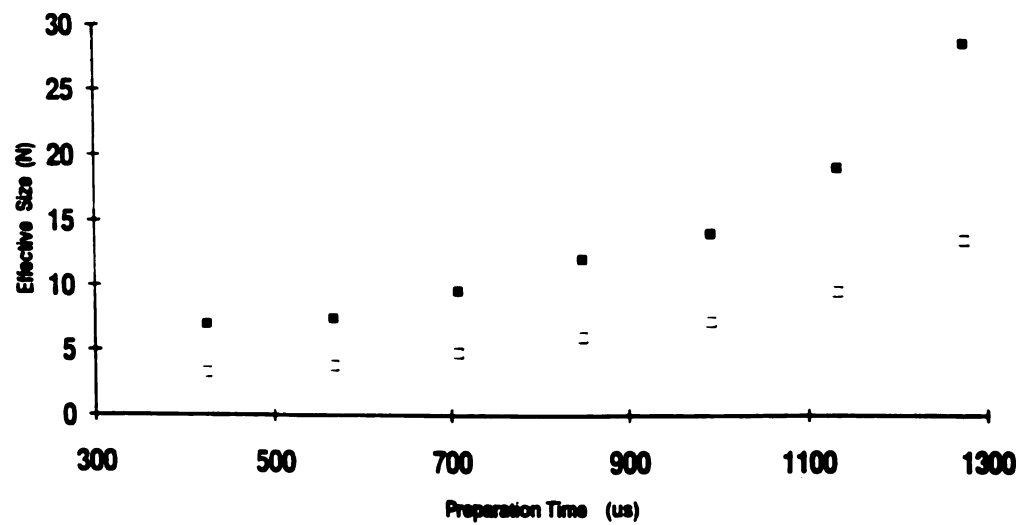
Figure V-4 Effective size vs preparation time in fluorapatite. Results from two orientations are shown; $\theta = 90°$ (■) and $\theta = 90°$ (□).

References for Sections IV and V

1. D. P. Weitekamp, in Advances in Magnetic Resonance, Vol. 11, ed. J. S. Waugh (Academic Press, New York, 1983) p. 111.

2. S. Lacelle, in Advances in Magnetic Resonance, Vol. 16, ed. J. S. Waugh (Academic Press, New York, 1991) p. 173.

3. M. Munowitz and A. Pines, Advan. Chem. Phys. 66 (1987) 1.

4. K. K. Gleason, Conc. Magn. Reson. 5 (1993) 199.

5. J. Baum, M. Munowitz, A. N. Garroway and A. Pines, J. Chem. Phys. 83 (1985) 2015.

6. J. Baum and A. Pines, J. Am. Chem. Soc. 108 (1986) 7447.

7. B. E. Scruggs and K. K. Gleason, Chem. Phys. 166 (1992) 367.

8. G. Cho and J. P. Yesinowski, Chem. Phys. Letters, 205 (1993) 1.

9. G. Cho. Thesis, Michigan State University, 1993.

10. M. Mehring, in: NMR: Basics Principles and Progress, Vol. 11, eds. P. Diehl, E. Fluck and R. Kosfeld (Springer, Berlin, 1976) p. 14.

11. R. W. Warren, F. M. Ryan, R. H. Hopkins, and J. Van Broekhoven. J. Electrochem. Soc. 122, 752 (1975).

12. D. N. Shykind, J. Baum, S.-B. Liu, A. Pines and A. N. Garroway, J. Magn. Reson. 76 (1988) 149.

13. P. Caravatti, M. H. Levitt and R.R. Ernst, J. Magn. Reson. 68 (1986) 323.

14. F. S. DeBouregas and J. S. Waugh, J. Magn. Reson. 96 (1992) 280.

15. B. N. Provotorov, Soviet Phys. JETP 14 (1962) 1126.

16. W. Van der Lught and W. J. Caspers, Physica 30 (1964)1658.

17. H. Eisendrath, W. Stone and J. Jeener, Phys. Rev. B 17 (1978) 47.

18. D. H. Levy and K. K. Gleason, J. Chem. Phys. 96 (1992) 8125.